Band Engineering of Perovskite Ferrite Epitaxial Thin Films for OER Catalysis

By

Rajendra Paudel

A dissertation submitted to the Graduate Faculty of
Auburn University
in partial fulfillment of the
requirements for the Degree of
Doctor of Philosophy

Auburn, Alabama
August 6, 2022

Keywords: MBE, RHEED, XPS, XRD, AFM, $SrTiO_3$, $LFeO_3$, $LaNiO_3$, Heterostructure, Interface

Approved by

Ryan Bradley Comes, Chair, Assistant Professor, Department of Physics
Sarit Dhar, Associate Professor, Department of Physics
Jianjun Dong, Professor, Department of Physics
Yu Lin, Professor, Department of Physics
Byron H. Farnum, Assistant Professor, Department of Chemistry and Biochemistry

Abstract

Reliable energy from renewable sources via oxidation of water requires an efficient electrocatalyst. The high cost, low abundance, and poor stability of the current noble metal based electrocatalyst are a primary obstacle to their commercial use. Perovskite-structured transition metal oxides have demonstrated enormous potential as catalysts in oxygen evolution reaction (OER) and oxygen reduction reaction (ORR). Particularly, $LaFeO_3$ and $LaNiO_3$ have shown great potential as catalysts in the oxygen evolution reaction (OER). However, their catalytic performance needs to be improved significantly for commercial applications to compete with precious metal catalysts. One primary method of optimizing electrocatalytic property is by tuning their electronic properties. In this work I show different ways to perturb the electronic structure of $LaFeO_3$ and $LaNiO_3$ and how that will lead to improvement in their catalytic performance.

Thickness is one important parameter to tweak the electronic properties in thin films. Changing film thickness in $LaFeO_3$ thin films grown on *n*-type Nb-doped $SrTiO_3$ changes its bulk intrinsic behavior from *n*-type in thinner films (1-2 nm) to an intrinsic semiconductor in relatively thicker films, leading to a volcano-like trend in OER performance with thin film thickness. Cation substitution is another key parameter to tune the electronic properties. Sr substitution in $LaFeO_3$ thin films leads to the creation of delocalized oxygen holes, facilitating electron transfer between the catalyst and electrolyte solution. As a result, a sharp increase in OER performance was observed with Sr substitution compared to $LaFeO_3$ thin films. Similarly, creating a $LaNiO_3/LaFeO_3$ heterostructure shows a dramatic increase in OER performance of the $LaFeO_3$ due to the interfacial charge transfer and tuning of the band alignment to produce *p*-type $LaFeO_3$. Our findings in this

work show that perovskite TMOs are promising materials for OER catalysis when perturbed out of their equilibrium electronic structure. They have tremendous potential to be a good substitute to the noble-metal catalyst for oxygen evolution reaction (OER) in energy storage devices.

Acknowledgments

I've received help and support from numerous people to complete my PhD dissertation. I'd like to express my gratitude in the following.

First of all, I'd like to express my deepest gratitude to my advisor Prof. Dr. Ryan Comes for his guidance and incessant support all along. I feel incredibly fortunate to have had the chance to work with Professor Ryan Comes on my Ph.D. research at. The work environment and his support provided me with invaluable opportunities to attend several international conferences and further my scientific and personal development. I'm grateful for his help during one of the most difficult times of my life. Above all, he has shown me how to be a good human being. Thank you for everything you've done for me.

I'm grateful to my dissertation committee members Prof. Dr. Yu Lin, Prof. Dr. Jianjun Dong, Prof. Dr. Sarit Dhar and Prof. Dr. Byron Farnum for their comments feedback and their valuable time. I'm grateful to Prof. Dr. Marcelo Kuroda for his guidance in theoretical and computational aspect of my research work.

I'd like to thank Dr. Byron Farnum and his graduate student Andricus Burton for collaborative work on electrochemical characterization. These data constitute a substantial portion of my dissertation.

I’d like to thank Dr. Steven Spurgeon, Dr. Michael Sassi at pacific northwest national laboratory (PNNL) for providing us with STEM data. I’d also like to thank Dr. Tiffany Kasper at PNNL for her valuable suggestion in our research publication.

I’d like to thank my colleagues at auburn physics department, Dr. Suresh Thapa, Dr. Miles Blanchet, Mr. Patrick Gemperline, and Mr. Jibril Ahammad, who helped me in lab and help make an office environment creative.
Many thanks to faculty, research scientists and students at auburn physics department who helped me in any effort.

My deepest gratitude goes to my parents Krishna Prasad Paudel and Chet Kumari Paudel. I feel extremely lucky to have such wonderful parents. I can’t thank enough for their love and support. My uncle Mahendra Prasad Paudel and my grandparents Bhumi Datta Paudel and Dambar Kumari Paudel, an epitome of hard work and persistence, who has always been a great source of inspiration for me. I’d like to thank them for teaching me love, care, kindness, hard work and persistence. My siblings, Sagar and Sreejana Paudel, who have always encouraged me to succeed. I’m thankful to them.

A special thanks to my wife Season Baral, who has always been my driving force, for her motivation, support, and unconditional love. My two lovely kids Reeti and Reyan, who taught me love and purpose of life. I’m thankful for their presence in my life.

I’d like to acknowledge the National Science Foundation Division of Materials Research for supporting me through grant NSF-DMR-1809847. HRXRD was performed with a Rigaku SmartLab instrument purchased with support from the National Science Foundation Major Research Instrumentation program through grant NSF-DMR-2018794.

Finally, I’d like to thank Physics Department at Auburn University, for providing me with all the resources and the foundation necessary for the completion of my PhD.

Table of Contents

List of Figures

List of Abbreviations

MBE	Molecular Beam Epitaxy
XPS	X-ray Photoelectron Spectroscopy
AFM	Atomic Force Microscopy
XRD	X-ray Diffraction
CV	Cyclic Voltammetry
EIS	Electrochemical Impedance Spectroscopy
TEM	Transmission Electron Microscopy
XAS	X-ray Absorption Spectroscopy
QCM	Quartz Crystal Microbalance
RHEED	Reflection High Energy Electron Diffraction
2DEG	2-Dimensional Electron Gas
STO	Strontium Titanate
SNO	Strontium Niobate
LFO	Lanthanum Ferrite
LNO	Lanthanum Nickelate
LAO	Lanthanum Aluminate
LSFO	Sr doped Lanthanum Ferrite
OER	Oxygen Evolution Reaction
ORR	Oxygen Reduction Reaction
Nb:STO	Niobium Doped Strontium Titanate

CBM	Conduction Band Minimum
VBM	Valence Band Maximum
TMO	Transition Metal Oxide
TM	Transition Metal
STEM	Scanning Transmission Electron Microscopy

Chapter 1

Introduction

Global energy demand is steadily rising, and this trend is expected to accelerate in the future [1]. Majority of current energy supply is derived from fossil fuels. Our fossil fuel reserve is limited, and they are polluting our environment [2]. A clean and sustainable energy supply is essential for addressing this issue. Significant progress has been made in this direction, such as solar or wind energy, but efficient energy conversion and storage technology is required for dependable energy supply. Electrochemical water splitting is one of the most promising technologies that can convert electrical energy into chemical energy and vice versa [3]. Oxygen evolution reaction (OER) and its reverse chemical reaction (oxygen reduction reaction (ORR)) are the key chemical reactions in the electrochemical energy conversion process. However, the slow reaction kinetics and low energy efficiency are the major obstacles in its practical application [4,5]. Use of electrocatalysts such as Ir and Pt has been helpful in improving the rate of reaction and lowering the overpotentials, but the lack of efficient, stable and economic electrocatalyst has posed a significant barrier to their widespread use.

Transition metal oxides have emerged as new class of electrocatalyst material [6–9]. The conventional electrocatalysts, Ir and Pt have low overpotential and are a good catalyst, but they are very expensive, and are rare. On the other hand, TMOs are highly abundant and low-cost materials. Transition metal oxides such as $LaNiO_3$, $LaCoO_3$, and LaFeO3 exhibit good catalytic performance in their intrinsic form [8,10]. Further, their catalytic properties can be optimized by appropriate

tuning of their electronic structure [11–13]. Their catalytic performance has been significantly improved by tuning thickness, strain, doping, or by creating heterostructures, and they have been found to outperform even Pt in a strained LNO thin film [11–13]. Therefore, TMOs have enormous potential as an alternative to conventional electrocatalysts.

1.1 Perovskite Structured Transition Metal oxides

Transition metal oxides (TMOs) have long been at the forefront of material science research due to their vast spectrum of electrical, optical, and magnetic properties, making them ideal for a wide range of applications. Electronic properties in transition metal oxides are dictated by partially filled d-orbital electrons. In 3d-transition metals (TM), the hybridization between O 2p and TM 3d orbitals changes the bonding environment thereby affecting the ability of electrons to move in a lattice [12]. TMOs have narrow 3d bands compared to other metals which produces strong coulomb interactions known as strong correlation [14]. Partially filled d-orbitals provide additional spin and orbital degrees of freedom, and TMs can have various valences and exist in mixed valence states. All these complexities make TMOs unique and interesting for various device application. High-temperature superconductivity [15–19], metal-insulator phase transitions [20–22], colossal magnetoresistance [23–25], ferroelectric and multiferroic properties [26–30] are just a few emergent properties that makes them ideal for their device application.

Lately, perovskite structured TMOs have received growing attention for their catalytic applications. TMOs have several characteristics such as multiple valences, abundance of active sites, and tunable electronic structure to make them the ideal candidate for a electrocatalyst [31,32]. Among the family of perovskite TMOs $LaFeO_3$ and $LaNiO_3$ are some of the preferred materials for OER catalysts. Lower overpotential, e_g occupancy, hybridization

between TM 3d and O 2p orbitals, position of d-band center and O 2p band center, make LFO and LNO superior candidate for the OER catalyst. [8,11,33–35]. Perovskites have the general structural formula ABX_3. A and B-sites are occupied by metal cations and X-sites generally oxygen, but the structure is stable with other anions as well. A-site is 12-fold coordinated with oxygen and B-site is 6-fold coordinated with oxygen atoms. The cubic perovskite structure is shown in Figure 1.1.

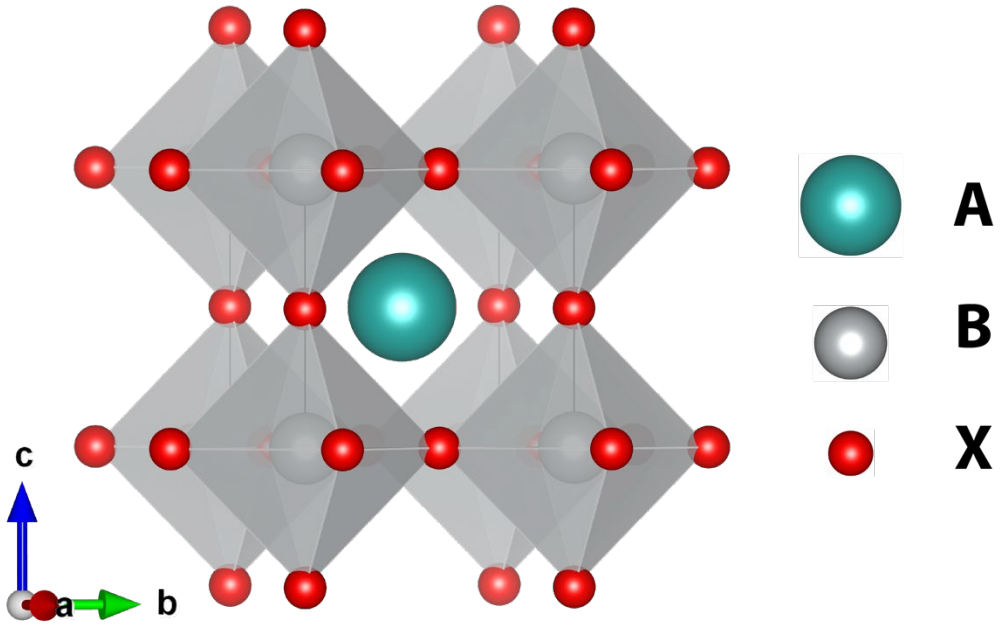

Figure 1.1: Cubic perovskite structure [36]. Where A site is occupied by larger cation which is 12-fold coordinated with oxygen (in oxides) and B-site cations are octahedrally coordinated with oxygen. In an ideal cubic perovskite, there is no octahedral tilting but the change in size of A and B-site cation can cause octahedra to tilt certain direction leading to a lower symmetry structure.

Most of the TM have one or more stable perovskite structures. Rare earth ions such as La may occupy the A-site with Fe or Ni in B-site in the perovskite structure. The structure and stability of

perovskites can be explained in terms of two parameters Goldschmidt's Tolerance Factor (TF) $TF = \frac{(R_A + R_X)}{\sqrt{2}(R_B + R_X)}$ and Octahedral Factor, $\mu = \frac{R_B}{R_X}$.

Where R_A, R_B and R_x are the ionic radii of A, B and X-site ions. Perovskites are stable for tolerance factor is roughly in the range $0.81 < TF < 1.10$ and octahedral factor should be in the range $0.414 < \mu < 0.732$ [37]. The ideal cubic perovskite has a tolerance factor close to 1. As the tolerance factor moves away from 1, the cubic structure is distorted, and the perovskite adopts tetragonal, orthorhombic or other lower symmetry structures. Considering tolerance factor and octahedral factor, perovskite TMOs can accommodate almost entire row of the periodic table in A or B-site. Also, perovskites can accommodate defects and multiple A-site or B-site cations [7,38]. This allows greater flexibility in material development with enhanced efficiency [39]. Therefore, the stability and tunability of perovskite TMOs makes them ideal for many types of energy applications.

In order to optimize these materials for practical applications, it is critical to understand the electronic properties of the bulk, thin films and heterostructures. Modern deposition techniques have made it easier to synthesize these materials as well as new materials with precise control of thickness, stoichiometry and doping into A or B-sites. Progress made in first-principles calculations within the framework of density functional theory (DFT) have significantly lowered the time and cost of modelling the properties materials at the fundamental level [40,41]. Development of exchange-correlation term, Hubbard correction, and well-developed plane-wave pseudopotential method has given DFT a very powerful predictive power of the material properties with higher accuracy [42–45]. Combination of experimental techniques and DFT is highly

effective in understanding the material properties and tailoring these materials for optimal device performance [43,46].

1.2 Thin Films and Their Heterostructures

A thin film is a material layer with a thickness ranging from few angstroms to several micrometers. Depending on the purpose and growth technique it can be amorphous, polycrystalline or single crystal. In this work thin film refers to epitaxial single crystal thin films. Thin films in general are interesting because of new phases emerge as a result of reduced dimensionality accompanied by spin or charge-ordering phenomena [47]. Transition metal oxide thin films are well known for various new phases and new properties that are not present in their bulk [48–50]. The unsaturated dangling bonds at the surface might result into the surface states that are not present in the bulk. The size effect may be dominant in deciding the mobility of electrons as various scattering mechanisms comes into play in thin films, which affects electronic and physical properties. Compared to bulk, thin films are generally free of defects and can be doped independent of the substrate. Therefore, Thin films have always been a preferred platform for researchers because of emergence of novel properties and tunability of thin film properties.

Perovskite ferrite thin films are good catalysts partly because of partially filled d-orbital and their ability to exist in mixed valence state. The mixed valence is usually caused by non-stoichiometry, which can be controlled either by doping or the oxygen pressure. Thin film thicknesses another crucial parameter that can be exploited to tune the properties of TMOs. May et al. have reported the thickness dependance of $LaFeO_3$ in photocatalysis [35]. In our recent work we've been able to establish the correlation between film thickness and OER catalytic activity in $LaFeO_3$ thin films [51]. Certain properties of the TMO thin films depend on orientation of the atomic planes.

$MnFe_2O_4$ thin films oriented along (100) is more active than the film oriented along (111) direction under ORR catalysis [52]. Therefore, thin film structures are important, as these unique properties exist in the thin films which may not be present in their bulk counterpart.

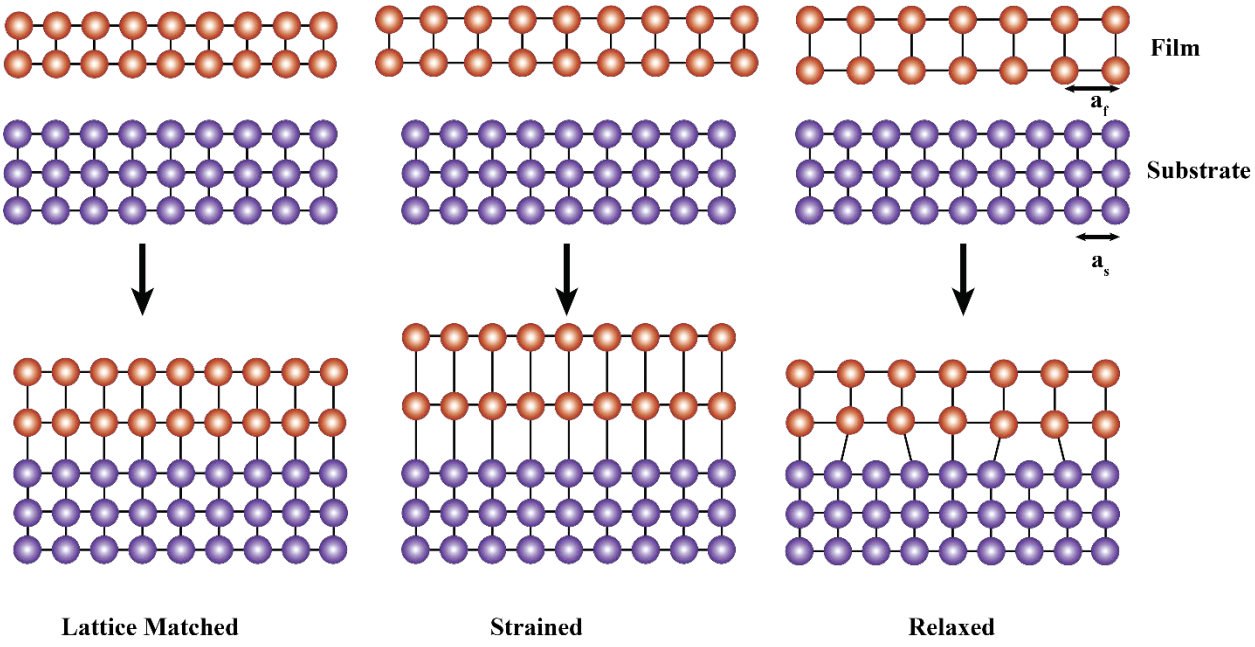

Figure 1.2: Schematic of lattice matched, fully strained and relaxed thin film heterostructures. In a lattice matched growth substrate and thin film are the same material. In the case of different material depending on the degree of lattice mismatch thin film is either strained or relaxed. For smaller strain, thin film is strained elastically to match the interatomic spacing in substrate producing coherent interface. Whereas for larger strain, thin film can't sustain the strain and eventually relax introducing misfit dislocations as shown in the rightmost figure.

Heterostructures are epitaxially grown thin film layers of two different materials. Lattice misfit between two different crystalline materials is the defining parameter in a heterostructure. Lattice misfit is defined as, $f = (a_s - a_f)/a_f$. Where a_s and a_f are the lattice parameter of the substrate and film. Epitaxial films with lattice misfit of less than 9% are coherently strained [53]. Schematic of different types of heterostructures is shown in Figure 1.2. All the heterostructure in this work are coherently strained multilayer structure.

From downscaling the size to designing a new material with novel functional properties, epitaxial heterostructures are at the core of modern-day electronics and many other technologies. In the word of Nobel laureate Herbert Kroemer "The interface is the device" [54]. In strongly correlated systems like TMOs and their heterostructures the interplay between charge, spin, orbital and structural degrees of freedom often results in complex novel properties [20,55–59]. The possibility of symmetry breaking which is the origin of different emergent properties makes heterostructure even more interesting. For example, breaking of inversion symmetry might result in ferroelectric properties, while broken time-reversal symmetry is associated with new magnetic phases [60]. Depending on the nature of the materials used in the heterostructure wide range of modifications to the intrinsic properties can be realized. Withs modern deposition techniques such as molecular beam epitaxy (MBE) and pulsed laser deposition (PLD), we can grow heterostructures with the sharp interface. However, cation intermixing over several unit cells at the interface is possible and must be accounted for in interpreting material properties. Cation intermixing affects the carrier density and introduces structural distortion [61].

One approach to engineering novel functionalities is through interfacial engineering of polarity or charge transfer. A polar discontinuity at the interface leads to high mobility 2DEGs [62–67]. The most notable example is discovery of 2DEGs at the interface of band insulators $LaAlO_3$ and $SrTiO_3$ [57]. After a 2DEG was discovered in polar/non-polar LAO/STO interface heterostructures and multilayer structures drew significant attention from the scientific community. Efforts to control and tune the 2DEGs have produced some impactful results, such as superconductive 2DEGs [65]. The interaction between metal cations across the interface leads to the double-

exchange interaction. Ferromagnetic phase has been observed at the $LaNiO_3/CaMnO_3$ interface. Double exchange interaction between Mn^{4+} -Mn^{3+} and super exchange interaction in Ni^{2+}-O-Mn^{4+} bonds which gives rise to a ferromagnetic phase at the paramagnetic/antiferromagnetic interface [59]. Rotations of the BO_6 octahedra due to oxygen octahedral coupling at the interface can be used to control magnetic properties, for example $La_{0.67}Sr_{0.33}MnO_3/NdNiO_3$ interface [68]. Band bending and charge transfer across the interface is another intriguing phenomenon in heterostructures. One of the earlier discoveries of charge transfer is $CaMnO_3/CaRuO_3$ interface. Ferromagnetic phases have been discovered at the interface as a result of charge transfer across the interface [69]. Therefore, heterostructures serve as the primary platform for scientists to invent materials with novel properties.

1.3 Effect of Cation Substitution and Epitaxial Strain

Cation substitution (doping) is a very effective way of tuning the intrinsic properties in bulk materials, thin films and heterostructures. In TMOs the dopant will occupy A-site or B-site depending on the nature of the impurity ion. One direct consequence of the doping is increased carrier concentration. Wide band gap insulator $SrTiO_3$ (E_g =3.2eV) can be made conductive by doping Nb [70] or La [71] in the A-site. Partial substitution of A-site and B-site can change the valence state via electron transfer or create holes which then affects material properties by tuning orbital overlap between metal d-orbital and oxygen 2p-orbital, covalency of the metal-oxygen bond, or filling of e_g orbital in metal cations. OER activity in perovskite TMOs is influenced by the number of d electrons [72], e_g filling [8], the covalency of metal-oxygen bond, hybridization between metal 3d and oxygen 2p orbital [12,13], the TM d-band and oxygen p-band centers [11] and the charge transfer energy [73]. By optimizing the interplay between these factors, OER performance can be improved. This can be achieved by proper doping into TMOs. Heavy doping

in perovskite A or B-site will increase the carrier concentration but decreases the mobility due to impurity scattering. Despite doping being the effective parameter to tune the properties, there's a limit depending on the type of application. When $LaNiO_3$ is doped with Fe, Ni obtains a fraction of an electron from Fe atoms as Ni^{2+} valence state is more stable, causing increased hybridization between TM 3d- O 2p orbitals [74]. Therefore doping Fe in $LaNiO_3$ B-site will enhance the OER catalytic activity [13]. They reported the volcano like trend in OER performance with 37.5% doping in B-site being the best OER catalyst. Larger Fe concentration will increase the coulomb repulsion in TM 3d bands and opens the gap making it harder for electrons to move across the fermi level. Similar results were reported for doping Sr in $LaNiO_3$ A-site [75]. The TMOs with highest OER performance are among some double perovskite structures such as $Ba_{0.5}Sr_{0.5}Co_{0.8}Fe_{0.2}O_{3-\delta}$, are also doped materials in a complex way [8,76]. Therefore, doping can be a very efficient way of optimizing the catalytic properties.

Strain primarily originates from the lattice mismatch between film and the substrate. Thinner films can withstand large strain, but thicker films eventually relax to reduce strain by creating misfit dislocations. Therefore, choice of the substrate is important in controlling the strain. Interfacial strain can bring about the significant changes in the materials properties. Distortion in the lattice due to epitaxial strain might break the degeneracy of metal 3d orbital causing 3d band splitting and changing charge transfer energy. $LaTiO_{3-+\delta}/LaNiO_3$ interface shows e_g band splitting and orbital polarization induced by the strain [77]. Epitaxial strain in $NdNiO_3$ causes splitting of e_g bands. Which changes the covalency and charge transfer energy leading to the metal-to-insulator transition to antiferromagnetic and paramagnetic phase for tensile to compressive strain [22,78]. Epitaxial strain can cause BO_6 octahedra tilting, breaking the octahedral symmetry [79]. There is a wealth of evidence that strain influences the catalytic properties. The application of strain might

change the metal -oxygen (M-O) bond length and cause splitting of d_{z^2} and $d_{x^2-y^2}$ orbitals. Tensile strain favors occupation of in-plane ($d_{x^2-y^2}$) orbitals and compressive strain favors occupation of out-of-plane (d_{z^2}) orbitals [80].

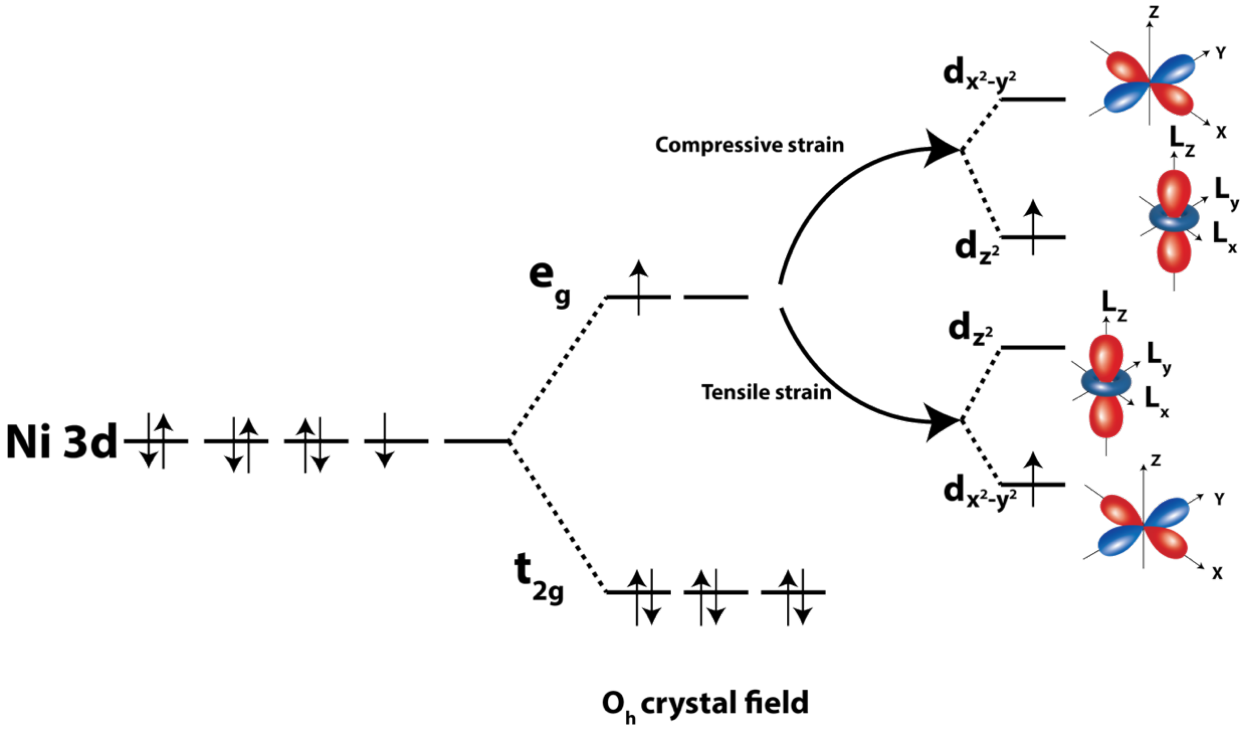

Figure 1.3: Ni 3d band splitting under octahedral crystal field and under strain. The octahedral crystal field splits 3d bands into 2-fold degenerate e_g and 3-fold degenerate t_{2g} bands. Under tensile and compressive strain degeneracy of e_g bands is lifted further making filling of an in-plane and out-of-plane orbitals favorable respectively.

Schematic of 3d orbital splitting of under tensile and compressive strain is shown in figure 1.3. Out of plane orbital filling lowers the d band center, which favors catalysis. $LaNiO_3$ under compressive strain shows higher catalytic activity [11]. Similar results have been observed in

$LaCoO_3$ thin film [81]. Therefore, strain engineering is crucial in designing a catalyst with improved performance.

1.4 Band Alignment and Charge Transfer

Heterojunctions have a discontinuity in electronic bands at the interface. When two different materials are brought together, their Fermi energies align to be constant throughout the material; as a result, the valence band and conduction band realign themselves, which is known as band alignment. The discontinuity in the band edges after alignment of the Fermi level are the band offsets. In the heterostructure there exists a potential gradient across the interface if the charge is transferred across the interface. Band edges at the interface bends due to charge transfer. Band bending can be used to tune electron hole-pair separation or recombination. This is particularly useful to improve photocatalysts [82]. As the band offset represents the energy barrier for charge carriers, understanding band alignment is critical for understanding and manipulating heterostructure properties for various device applications.

Interfacial charge transfer is potentially superior way to achieve doping and can result in different novel phenomena that doesn't exist in their constituent material [83]. Doping adds electrons or holes to the material depending on the nature of dopant. We can achieve the same goal with charge transfer and avoid oftentimes unnecessary consequences such as lattice distortion and reduction in mobility due to the insertion of different atomic species in the lattice. We can control the amount of charge transfer required for specific device applications by selecting a suitable pair of materials. Charge transfer from Ti to Ni in $LaTiO_{3-+\delta}/LaNiO_3$ interface results in insulating ground states which can be used to new electronic and spin states [77]. A thickness dependent metal-insulator phase transformation has been reported in $LaNiO_3/LaMnO_3$ interface [84]. The

$LaTiO_3/LaFeO_3$ interface shows non-magnetic behavior as a result of charge transfer from Ti to Fe 3d orbitals [58]. In TMOs unoccupied e_g bands of the B-site cations are near the Fermi energy, therefore the possible charge transfer leads to an electronic rearrangement of the e_g orbital. Because A-site electronic bands are far from the Fermi level, they are usually indifferent to charge transfer. Even though the effect of interfacial charge transfer in catalysis has not been studied, we can expect it to have an impact on catalysis because B-site is the active site for OER catalysis.

1.5 Overview of the Dissertation

The study of perovskite rare-earth ferrites, specifically $LaFeO_3$, for its application as an OER catalyst is the focus of this dissertation. In a quest to optimize its catalytic properties, we tried to tune it's electronic structure by nanostructuring, doping and creating a heterostructure. This dissertation will present the systematic study of $LaFeO_3$, $LaNiO_3$, $LaFeO_3/LaNiO_3$ and Sr-doped $LaFeO_3$ thin films from synthesis to characterization. The thesis will conclude with a presentation of the results and a discussion of some future directions based on the experience gained during this work.

Chapter 2

Density Functional Theory

2.1 Introduction

Density functional theory is a quantum mechanical approach to compute the electronic structure of the materials. DFT has been very successful in predicting ground state electronic properties, though it is known for underestimating band gaps in semiconductors and insulators. Therefore, it has been widely used to study the electronic properties of numerous material systems, including complex oxides [85–88]. The DFT is based on the Hohenberg and Kohn theorem [40], which states that the total energy of the system can be expressed as the functional of ground state electronic density,

$$\mathrm{E} = E[\rho(r)]$$

The total ground state energy of the multi-particle system can be expressed as,

$$E[\rho] = T_k[\rho] + E_{eN}[\rho] + E_H[\rho] + E_{xc}[\rho]$$

where $T_k[\rho]$ is the single particle kinetic energy, $E_{eN}[\rho]$ is the electron-nucleus interaction energy, $E_H[\rho]$ is the Hartree energy, which accounts for the coulomb interaction between electrons, and $E_{xc}[\rho]$ is the exchange-correlation functional. The challenge in this method is accurately calculating exchange-correlation energy given by

$$E_{xc}[\rho] = \int d^3r\, \rho(r)\epsilon_{xc}(r)$$

Here for calculation of exchange correlation energy, $\epsilon_{xc}(r)$ requires some approximation. Commonly used approximation are the local density approximation (LDA) and generalized gradient approximation (GGA) [89].

Later, Kohn and Sham demonstrated that electron density for multi-particle system as sum as single electron density [41]. They were able to calculate the ground state energy accurately by solving Schrödinger-like equation using density dependent potential called Kohn-Sham equations [41]. Which is written as,

$$[T + V_{eN}(r) + V_H(r) + V_{xc}(r)]\varphi_i(r) = \varepsilon_i(r)\,\varphi_i(r)$$

where $\varphi_i(r)$ are the Kohn-Sham orbitals. The success of this method lies in the self-consistent calculation of the electron density. The electron density is defined as,

$$\rho(r) = \sum_{occ} \varphi_i^*(r)\,\varphi_i(r)$$

Once the electron density is calculated, the ground state energy can be calculated for a multiparticle system.

The DFT modeling software Quantum ESPRESSO was used for first principles calculation in this work [90,91]. Quantum ESPRESSO is open-source software, which has been widely used to compute ground state electronic and structural properties Over the years the code has been improved significantly and has become more robust such that even non-equilibrium (excited state) properties can be calculated [91]. First principles methods using DFT commonly employs plane wave pseudopotential [92] or projector augmented wave methods [93] with LDA or GGA

approximation for exchange correlation functional to calculate the electronic structure of many body electron systems.

2.2 DFT+U Method

The LDA or GGA approximation on exchange-correlation functionals are based on the homogeneous nature of the electron gas [94,95]. Despite the success of this model, it fails to accurately describe the ground state properties of most transition metal oxides. In transition metals with d or f-valence shells, valence electrons experience strong onsite Coulomb interaction producing what are known as strongly correlated electron systems. A common problem is the underestimation of band gap in the insulators and semiconductors [96,97]. In order to address this problem one of the widely used method is introduction of correction potential inspired from Hubbard model [44], which is commonly known as DFT+U method. There are two different approaches to introduction of Hubbard correction. One is Hartree-Fock like Coulomb potential(U) as described by Dudarev *et al.* [98].The other approach is considering the anisotropic Coulomb interaction. In addition to Coulomb interaction(U), the exchange term(J) is also included [99]. But for simplicity both Coulomb and exchange interaction is used as a single parameter as U_{eff}=U-J. Introduction of Hubbard correction has been successful in predicting the band gap and ground state electronic structure in strongly correlated systems [43,100].

The choice of U is not unique and cannot be physically determined from first principles. Instead the value of U is chosen to match physical parameter such as lattice constant or the electronic band gap with experimental results. However there are newly developed approach to self-consistently calculate the U parameter known as ACBN0 [42]. ACBN0 method accounts for both the coulomb

interaction and exchange interaction to calculate U parameter. This method has resulted in improved prediction of electronic band structures in the transition metal oxides [88].

Chapter 3

Thin Film Growth

3.1 Molecular Beam Epitaxy (MBE)

Epitaxy refers to the deposition of a crystalline material on a crystalline substrate, where atoms on the deposited layer arrange in the same structure and orientation as the substrate crystal. Therefore, the whole structure is a single-crystal, and the deposited layer is an extended part of the single crystal substrate. If the deposited layer and the substrate are the same material, the synthesis is called homoepitaxy; if they are different, it is called heteroepitaxy. Homoepitaxial or heteroepitaxial thin films allow us to alter their bulk properties either by doping or by applying strain. Thus, epitaxial films offer unique opportunity for scientists to develop new materials for a wide range of new applications. Different applications where thin films are useful or being explored were discussed in chapter 1.

The modern-day MBE is the result of advances in vacuum science and the deeper understanding of materials in the most fundamental level over several decades. MBE was initially used for the growth of III-IV narrow gap semi-conductor compounds such as GaAs, $Ga_{1-x}Al_xAs$, $Ga_{1-x}In_xAs$, which were thought at the time to be excellent candidate semiconductor to be used in MOSFETs [101,102]. To grow these compound materials atomic fluxes were obtained by heating source materials to high temperature to evaporate or sublimate from the sources. These materials were relatively easy to grow as they would easily react to form a crystal at high temperature [101]. Due to the thermodynamically favorable 'growth window' even if there is excess flux of volatile As, only those As atoms would stick to the substrate which can bond with Ga and excess As desorbs from the surface.

After the discovery of high temperature superconductivity in Ba - La- Cu- O system, the transition metal oxide thin film gained significant attention [103]. Unlike GaAs systems transition metals lack adsorption-controlled growth window and therefore are challenging to grow. Transition metals generally need higher oxygen pressure to adequately oxidize their thin films. In the MBE, metals are brought to gas phase by thermal evaporation and therefore have low kinetic energy(~0.1eV). If the oxygen pressure is too high, such low energy particles suffer scattering and result in poor quality thin films. Supply of atomic oxygen through plasma or ozone were developed as they were highly reactive even at low pressure and temperature. [104,105]. Another challenge was to bring refractory metals such as Hf, Ta, Nb, Ti in gas phase using effusion cell and maintaining the stable flux. These materials have commonly been evaporated using an electron-beam evaporation source, though more recent efforts have focused on the use of metal organic precursors [106,107].Which solved the issue of refractory metals despite some challenges and difficulty in integrating metal organic source to the MBE system. Some other transition metals evaporated easily in the effusion cell, but due to oxidation of the source material in the effusion cell during its exposure to high oxygen pressure during growth, it was difficult to obtain their stable flux or the source material has to be replaced too often [108]. The use of differential pumping and more powerful turbomolecular pumps helped in minimizing this problem [109]. Integration of in-situ RHEED made it possible to monitor the thin film growth in real-time. Which allows us to perfect the growth recipe. With all these advancements it has become possible to grow wide range of materials including binary to quaternary perovskite oxides artificially [106,107,110].

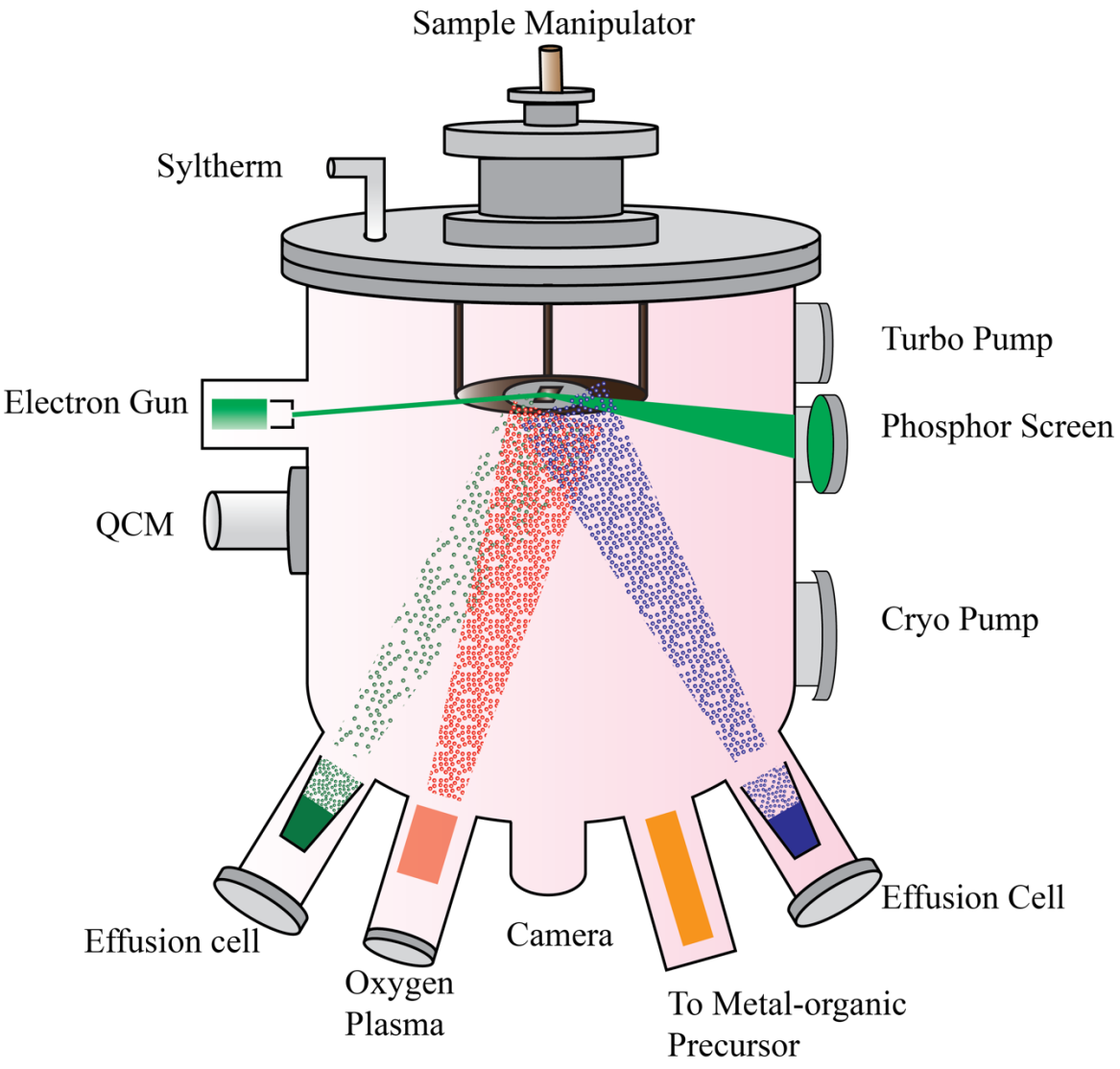

Figure 3.1: Auburn FINO Lab plasma- assisted MBE system. The MBE chamber is kept in ultra-high vacuum environment. Substrates are transferred from loadlock chamber with the help of sample manipulator and magnetic transfer arm in high vacuum condition. The individual metallic fluxes are obtained by heating source materials in effusion cells situated at the bottom of the chamber. Highly reactive radio frequency oxygen plasma is used for oxidation of the thin films. And high energy electron diffraction pattern, as indicated in light green color, is used to monitor the thin film growth.

Modern oxide MBE systems use Knudsen effusion cells, where elemental or molecular sources are heated to get atomic or molecular fluxes. Atomic fluxes are measured using a quartz crystal

microbalance (QCM). The MBE chamber base pressure is ~10^{-9} Torr And operates at oxygen background pressures of 10^{-6} to 10^{-5} Torr. At such a low pressure, evaporated atoms have high mean free path so that they are not scattered via collision with oxygen atoms and molecules and easily reach the hot substrate where they diffuse and crystalize. The schematic of the MBE system is shown in Figure 3.1. Evaporated atoms have low kinetic energy (~0.1 eV) which enables coherent and psuedomorphic growth of the single-crystal film. Oxygen is supplied through an RF plasma source. The oxygen plasma efficiency varies, depending on plasma power and oxygen pressure. High power plasma tends to damage the substrate or thin film itself. But nowadays plasma is pretty standard and helps sputter clean carbon or water molecules from the substrate surface without causing any damage to the substrate or film [111,112]. Ozone, on the other hand, is a highly reactive oxygen source, can be an explosive due to exothermic nature of ozone liquefaction. Therefore ozone should be handled more carefully to prevent any such incident [113] In addition to effusion cells, atomic fluxes also can be obtained through the metal-organic precursor source. Refractory metals such as Ti, Nb, Hf fluxes can be obtained by heating their metal-organic precursor at low temperature [106]. The FINO Lab MBE is designed to accommodate metal-organic precursors, though these were not used for this work.

Perovskite oxides have a layered structure, alternating between AO and BO_2 planes along the <100> directions in the crystal. MBE employs slow growth process and gives better control over each layer deposited and each atomic layers can be doped independently to achieve uniform doping throughout the sample. Shuttered growth alternating between A site and B site cations can help to control stoichiometry to produce more precise films [114]. Therefore, MBE in layer-by-layer growth mode is ideal for synthesis of perovskite oxides.

All the thin film samples discussed here are grown using MBE in layer-by-layer growth mode. By controlling the shutter individually one layer was grown at a time. In the case of LFO, LaO and FeO_2 layers were deposited alternately to achieve layer-by-layer growth. 300-watt radio frequency plasma was used to supply highly reactive atomic oxygen. All the samples were annealed post-growth in oxygen plasma during cooldown to achieve adequate oxidation of the thin film samples. Growth was monitored using RHEED and diffraction spots were sharp, and intensity shows nice oscillation with periods matching the shuttering sequence.

3.2 Growth Modes

Growing a high-quality thin film is optimizing the interplay between temperature, oxygen pressure and molecular fluxes. The growth process is bound by laws of thermodynamics and kinetics. Depending on the temperature and pressure the atomic layers arrange differently on the substrate to form a single crystal.

Schematic of different growth modes in epitaxial growth is shown in figure 3.2. Island growth (Volmer-Weber growth) occurs usually at low temperature. When particles don't have sufficient kinetic energy to move around the substrate surface the atoms form a cluster. They are more strongly bound together than with the substrate surface [115]. The atoms form a columnar structure on the substrate. As the growth proceeds structures rise above the surface with multiple unit cells of roughness and the intensity of the RHEED spots decreases. Two-dimensional array of diffraction spots can be seen in the RHEED patterns in this case due to transmission of electrons through the small islands. This is the key indicator of island growth.

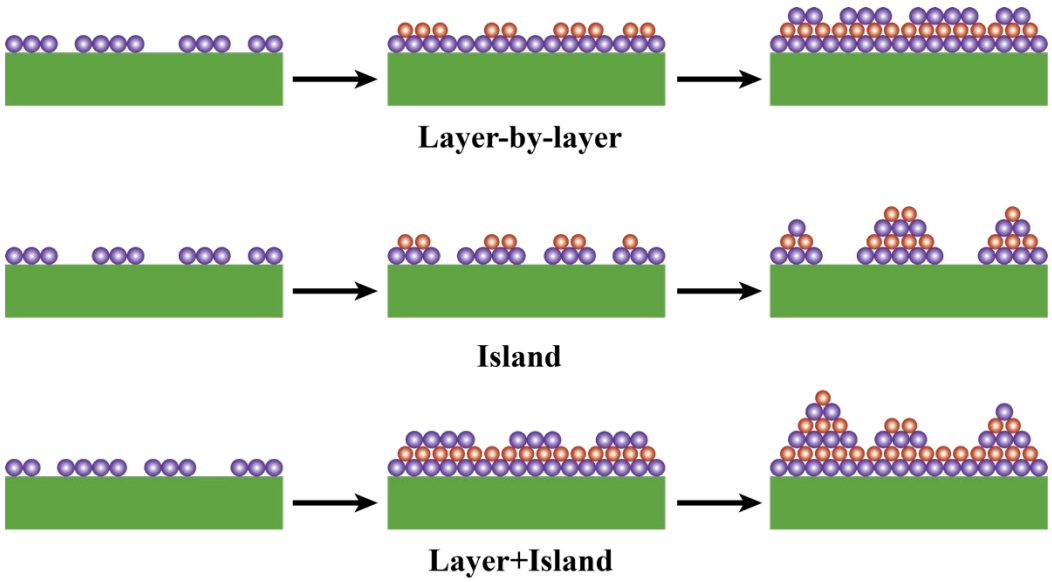

Figure 3.2: Different growth modes common in MBE. In layer-by-layer mode one atomic layer is filled completely before another layer start to fill, producing atomically flat surface, whereas Island formation produces rougher surface.

In a layer-by-layer growth mode (Frank-van der Merwe growth), one atomic layer is deposited at a time and the second layer doesn't start until the first layer is completed [116]. This type of growth usually occurs at temperatures higher than for island growth. The atoms are bound more strongly with the substrate than with each other. The atoms have sufficient energy to diffuse across the surface but not enough energy to cross the step terrace on the substrate surface due to the Ehrlich-Schwoebel barrier [117,118]. This growth mode is particularly important for the synthesis of multilayer materials. We can effectively control the thin film thickness in this mode and produce abrupt interfaces. If the atomic or molecular fluxes are calibrated properly each oscillation corresponds to one monolayer. We can calibrate flux and the shuttering time to match one monolayer per oscillations based on the information from X-ray reflectivity data and RHEED [119]. This will enable us to control thickness with the precision of a monolayer and make precise heterostructures.

When the atoms have sufficient energy to move around the surface, atoms move to thermodynamically favorable steps and starts depositing. When one step is complete atoms move to the next energetically favorable step and growth continues this way. This is called step flow growth [120]. This occurs at higher substrate temperature. During step flow growth RHEED intensity doesn't oscillate but remains bright all the time, as the surface termination is unchanged throughout the process.

The combination of both island and layer-by-layer is also possible and is known as Stranski-Krastanov growth. Film growth starts with layer-by-layer mode and island formation begins to occur as condition becomes energetically unfavorable [115].

3.3 Role of Substrate and Substrate Preparation

The choice of substrate is critical for any type of thin film or heterostructure growth. The surface termination, substrate orientation and lattice mismatch significantly impact the thin film properties. The most important parameter here is the lattice mismatch, which is primarily used to control the strain. Although strain in thin films or heterostructures has led to the novel phenomena [121–125], excessive strain could be detrimental to film quality due to the lattice distortion or formation of defects [126]. The surface orientation of the substrate affects the orientation of thin films as well. For example Depending on the orientation of exposed film surface their certain properties might vary [128].

The thin film properties or interfacial phenomena in heterostructures may also be impacted by the substrate termination. One famous example is the creation of 2DEGs at the TiO_2-terminated LAO/STO interface [57,129]. Specific termination can be obtained by chemical etching. By

immersing STO substrate in hydrofluoric acid solution Sr is etched out and after annealing TiO_2 termination can be obtained [130].

Figure 3.3: 10x10 mm2 Nb:STO Substrate mounted on a sample holder. The samples are mounted with the help of foil, pins and a thin wire made up of Ta to sustain high temperature condition. The front surface of the substrate is polished to produce atomically flat surface and therefore looks shiny.

For the work in this dissertation, we used commercially available cubic (001) STO and 0.7% (001) Nb doped STO. Cubic (100) $LaAl_2O_3$ (LAO) and cubic (100) $(LaAlO_3)_{0.3}(Sr_2AlTaO_6)_{0.7}$ (LSAT) were also used for calibration growths. STO has a small lattice mismatch with both LNO and LFO, which helped to minimize structural defects in these materials thanks to the absence of misfit dislocations.

The substrate and holder used for the growth are shown in Figure 3.3. Dimension of the substrates were either 10x10 mm^2 or 5x5 mm^2. The substrates were sonicated in acetone and then in isopropanol for ten minutes each. The substrate was dried with nitrogen gas to obtain a clean surface. All the substrate we used for the growth were used without any etching or annealing.

Regardless of surface termination or presence of steps or terraces on the substrate all thin films reported here are of excellent quality.

3.3.1 Challenges with Oxide Molecular Beam Epitaxy

The MBE system itself is a complex system. Multiple pumps are working in tandem to maintain the ultra-high vacuum system. Effusion cells, RHEED gun, and a QCM are attached to chamber on ports that are confocal with the substrate stage. Multiple chillers are working continuously to cool down the heated effusion cells and sample stage and maintain a lower temperature shroud at -30°C for improved base pressure. system. The complex nature of the system makes its upkeep challenging. Maintenance of the cryo pump and scroll pump must be performed regularly. Sudden failure of any of these components could be costly. Electrical parts such as motors that are used to control the shutters may need regular replacement or maintenance. As the mass accumulates over time, the QCM becomes less sensitive and requires regular replacement. Due to the heat and extended exposure to the highly reactive oxygen in the chamber, the filaments in the effusion cells, stage, or RHEED gun may oxidize, which reduces their life. The oxidation of the source material in the effusion cells is one typical issue. For the highly reactive source material and RHEED system and a differential pumping system has been installed to prevent oxidation. Another issue we've been having is obstruction of the effusion cell opening due to oxidation. Particularly with nickel and manganese because of the formation of oxide layer, blocks the effusion cell opening, which either makes the particle flux unstable or completely blocks it. We should routinely clean these cells, which is time consuming and tedious process.

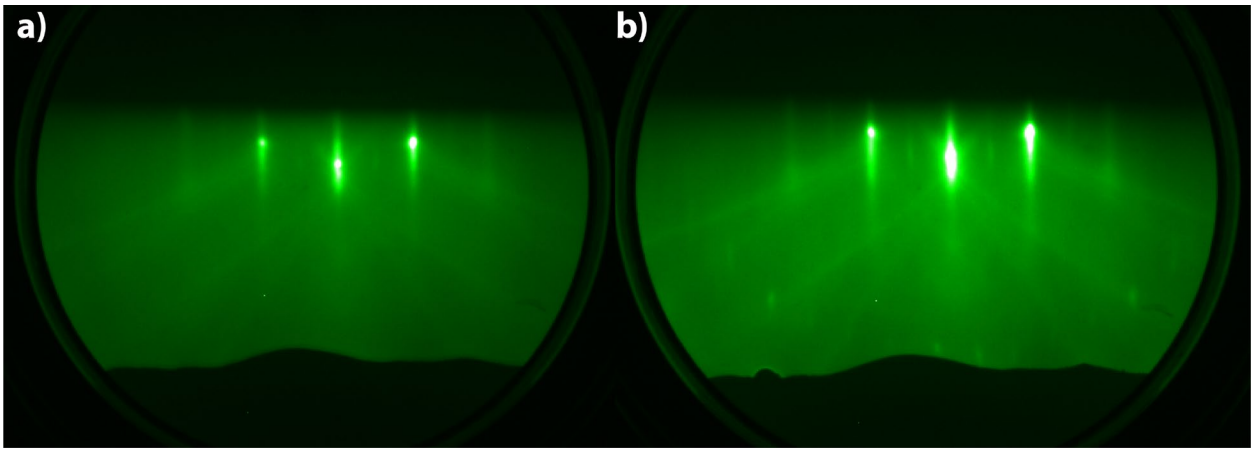

Figure 3.4: a) LaFeO3 thin film right after the growth b) same thin film after 30 minutes of post-growth annealing in oxygen plasma. The RHEED pattern is brighter after annealing in oxygen plasma, which indicates the better oxygen stoichiometry.

Finding the ideal oxidation condition to minimize defects is another challenge. In low oxygen environment the oxygen vacancies are more likely to form. Meanwhile, if the oxygen environment is too high, secondary phases become more stable and cation defects are formed [131]. Post-growth annealing in oxygen is very effective in minimizing oxygen defects [132,133]. Using low oxygen pressure, thin film will suffer oxygen non-stoichiometry or form some defects, but these perovskite thin films can incorporate defects to some degree without forming a secondary phase and post-growth annealing reduces the concentration of oxygen defects. We annealed the LFO and LNO samples in oxygen for ~30 minutes after the growth. The RHEED images of the $LaFeO_3$ thin film right after the growth and after post-growth annealing is shown in Figure 3.4. The RHEED spots after the post-growth annealing is much sharper, indicates that the sample is free of defects.

Synthesis of LNO requires Ni^{3+} valence state. Ni^{2+} being more stable presents another challenge. Finding ideal temperature and pressure is crucial in LNO growth. If the thin film is not sufficiently oxidized results in mixed valence state with secondary phases. If the temperature is too high results

in lower oxidation state or defects. In thicker films formation of lower valence Ruddlesden-Popper phases is more common. And if the temperature is low that affects the crystallinity. Post-growth annealing was helpful in minimizing mixed valence or defects.

Chapter 4

Thin Film Characterization

4.1 Reflection High Energy Electron Diffraction (RHEED)

Modern MBE systems are equipped with an in situ RHEED system to monitor thin film growth in real-time. It uses collimated high energy electron (10-100KeV) beam incident on sample surface at grazing incidence to measure diffraction off of the plane of the film surface. Due to small glancing angle (1°-5°) electrons probe only one or two atomic layers and the diffraction pattern of the forward scattered electrons are observed on the phosphor screen as shown in Figure 4.1. A CCD camera is mounted to the flange holding the phosphor screen and the video is fed to the computer for further analysis.

The diffraction pattern we observe on the screen is due to the constructive interference of the electrons satisfying Laue's condition [134,135]. The separation of the RHEED spots is the reflection of interplanar spacing between adjacent atomic planes in reciprocal space. The shape of the diffraction spots is determined from the intersection of Ewald's sphere and reciprocal lattice planes of the atoms on the film surface. For example, the 1-D array of atoms in reciprocal space forms an equidistant plane separated by the reciprocal of their interplanar spacing in real space. For 2-D array of atoms in the reciprocal space forms an equidistant array of rods. When these rods in reciprocal space intersect with Ewald's sphere, they form a point. Therefore, diffraction patterns of the 2D lattice with atomically flat surface are point spots. However, due to lattice imperfections and lattice vibration reciprocal rods have finite widths, therefore RHEED patterns usually appears

streaky. In the case of surface reconstruction additional secondary streaks appear in between primary spots.

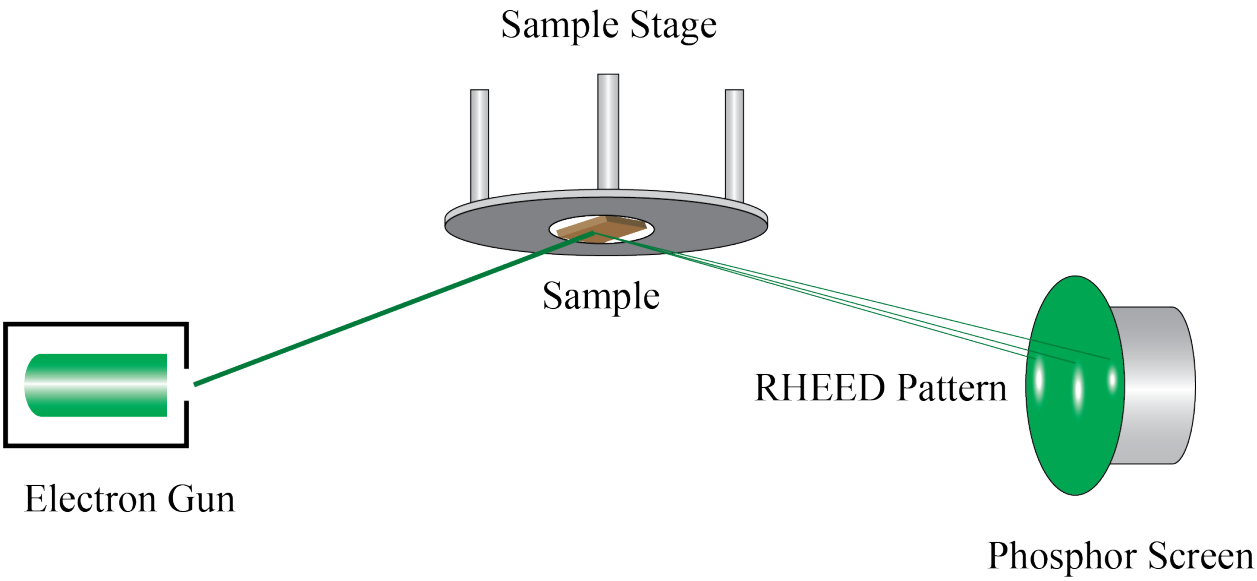

Figure 4.1: RHEED measurement arrangement in MBE system. The substrate is incident with high energy electrons (10KeV) at a small angle of incidence (1°-5°) and diffraction pattern of forward scattered electrons are observed on the phosphor screen.

RHEED pattern can be visualized as a reflection from a mirror. Schematic of RHEED intensity oscillation is shown in Figure 4.2. When the surface is smooth, intensity of reflected beam is maximized. If the surface is rough the intensity of reflected beam decreases. Since electrons are waves, they undergo diffraction and therefore they produce a diffraction pattern along with the specular reflection spot. When atoms are deposited on the substrate, the surface begins to roughen, and the intensity of the diffraction pattern decreases. As additional atoms populate the surface, it gets smoother, and the intensity begins to increase. When the layer is complete, surface is atomically flat which produces the maximum intensity in the diffraction pattern. This process results in oscillation in the intensity of diffraction pattern.

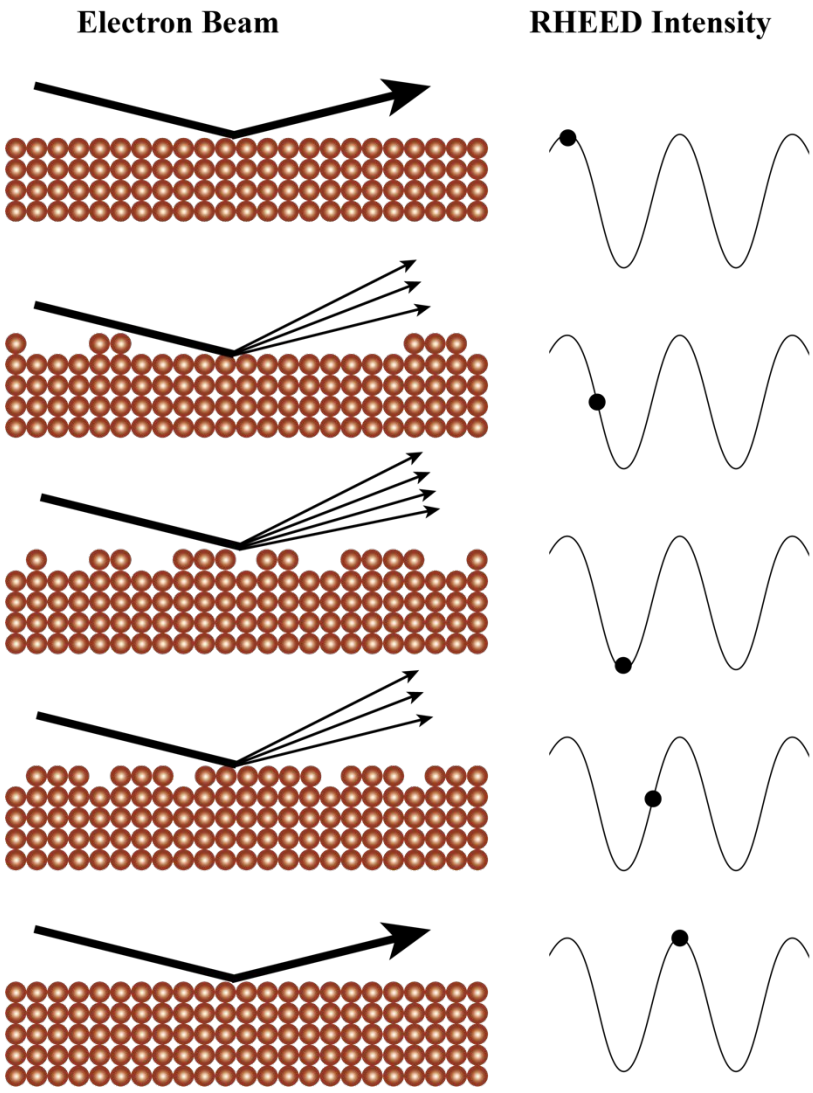

Figure 4.2: Deposition process of single monolayer in MBE and on the right are corresponding RHEED oscillations.

This is the unique feature of layer-by-layer growth mode, which allows us to effectively control the thickness. This is one of the advantages of the RHEED. If the atomic order degrades or thin film becomes non-crystalline, RHEED intensity diminishes quickly. RHEED can provide various information about the thin film in real time. The film thickness, growth modes, thickness of the film, growth rate, surface roughness, secondary phases and surface reconstruction can be easily

extracted from the RHEED pattern, which makes RHEED an essential component of the MBE system.

4.2 X-ray Photoelectron Spectroscopy

XPS is an important tool for characterizing thin films and epitaxial interfaces [136]. XPS can provide variety of information about the thin film such as chemical composition and electronic properties. The photoelectrons emitted carry the information about their bound state and the environment they originated from. Therefore, by careful analysis of the photoelectrons, detailed information about the local electronic structure can be obtained. Surface termination is important in the TMO thin films or heterostructures, particularly in the case of polar/non-polar interface to realize certain properties. Angle resolved XPS can provide such information. The potential gradient in the material influences the electron binding energies, which is associated with the photoelectron energies. Therefore, information of built-in potential or the band offset at the heterostructure interface can also be extracted from XPS.

The physics behind the XPS is the photoelectric effect. When the X-Ray is incident on an atom, it excites an electron from a particular shell and if the energy of photon is sufficiently high will eject the electron out of an atom. When a photon interacts with electrons, different phenomena can occur. For example, photon will excite an electron and subsequent transition will result in emission of photon again or photon can eject multiple electrons known as Auger electrons. XPS analyzes only the photoelectrons.

From the information of photon energy, the binding energy of the electrons can be calculated. XPS uses a monochromator to select specific wavelength. The XPS system generally uses Al K_α

(1487eV) or Mg K_α (1254eV) line. The photon energy and the binding energy (E_B) of photoelectrons are related as,

$$E_{photon} = h\nu = E_B + \Phi_S + E_{k'}$$

Where $E_{k'}$ is the kinetic energy of photoelectron with respect to the vacuum level. And Φ_S is the material work function. When electron enters the analyzer the kinetic energy of electrons as seen by the analyzer,

$$E_k = E_{k'} - (\Phi_A - \Phi_S)$$

Where Φ_A is the work function of the analyzer. Now binding energy of the photoelectron is calculated as,

$$E_B = h\nu - E_k - \Phi_A$$

The binding energy therefore depends on the analyzer work function rather than work function of the material.

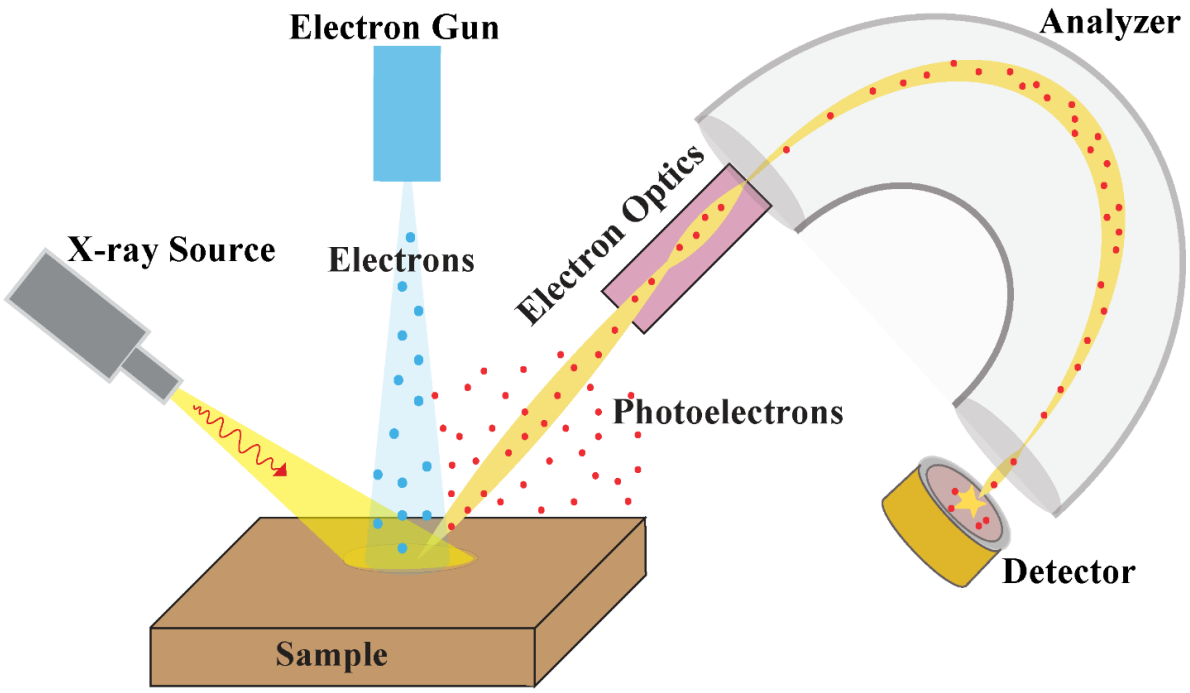

Figure 4.3: Schematic of the XPS system. Monochromatic X-ray ($Al_{k\alpha}$) is used as incident probe and photoelectron energies are analyzed to determine the binding energy of photoelectrons.

The schematic diagram of the XPS system is shown in figure 4.3. The photoelectrons enter the analyzer through the slit and are first decelerated to some constant energy value known as pass energy. The analyzer then counts the number of photoelectrons at given energies that pass through the entrance slit, where energy resolution is highly sensitive to the choice of pass energy and the width of a selected entrance slit. Energy resolution can be improved by narrowing the slit and decreasing the pass energy. And the electrons are at the end are focused to the detector. Due to the ejection of photoelectrons, charge may build of in the samples if it is not conductive, which may cause shifting of the binding energy of electrons. Lowe energy electron flood gun is used for charge compensation and minimize the effect of charging. In this work PHI 5400 XPS system was used. It uses Al Kα line for the measurement. The image of the PHI 5400 XPS system is shown in Figure 4.4.

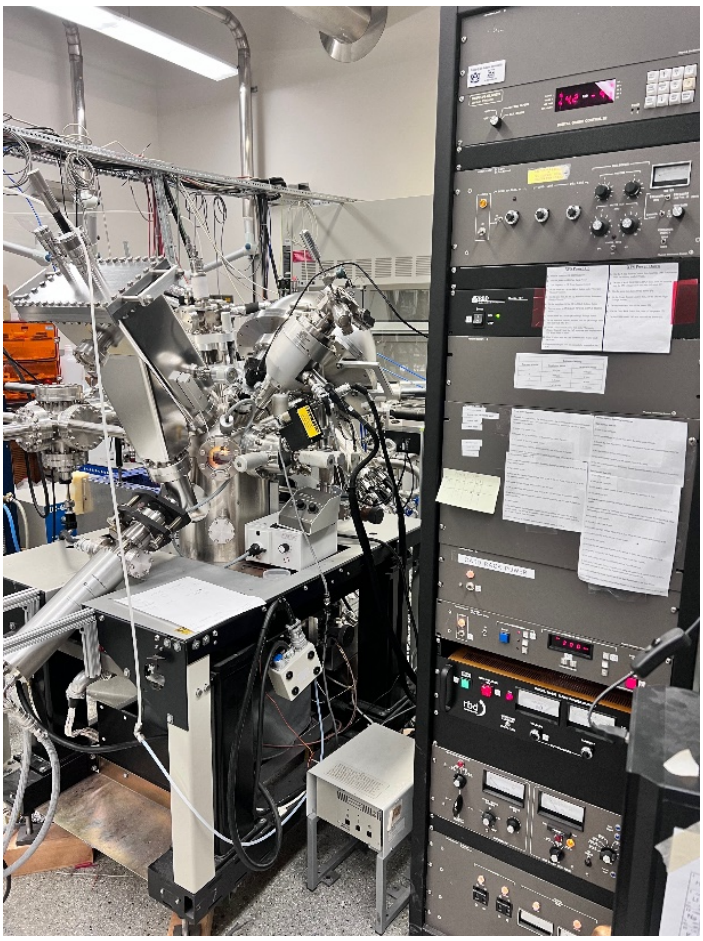

Figure 4.4: PHI 5400 XPS system in the Auburn FINO Lab. Hemispherical part is the photoelectron energy analyzer. Ultra-high vacuum condition is maintained using titanium sublimation pump. The vertical structure on the right side is power control rack for XPS system.

The depths that XPS can probe depends on the photoelectron's attenuation length (λ). The photoelectrons ejected out of an atom deep into the material undergo inelastic scattering and loses its kinetic energy. Inelastic scattering also increases the background level in lower binding energy region. Therefore, with soft X-ray one can obtain information from 5-10nm deeper into the material. XPS contains different peak features such as spin orbit splitting, spin multiplet splitting, shake up satellites and Auger peaks. The atomic orbitals with $l > 0$, spin and angular momentum couple according to L-S or J-J coupling scheme to split final states which leads to the doublet peak

in XPS. The separation of these doublet depends on the strength of the spin-orbit interaction. Another type of peak is spin multiplet splitting. When the valence band is not completely filled and have unpaired spin, that interacts with the core level spin to give rise to peak splitting. Both spin-orbit and spin-multiplet splitting are more common features among transition metal. When a core level electron is ejected out of an atom valence electrons experiences sudden increase in effective charge and respond this change by excitation of valence electrons to higher BE energy levels, which results in new peak feature in a low kinetic energy side known as 'shake up' satellite. Auger peaks are the most common peak feature in the XPS spectra. When the rearrangement of valence electrons to fill the core holes results into an ejection of secondary electrons, results in Auger peaks. These peak features are rich in information about electronic structure and bonding environment in the materials. All these effects should to be taken into account for the accurate analysis of the XPS data.

4.2.1 X-ray Photoelectron Spectroscopy Data Acquisition

For good XPS data collection, the sample must sit flat or should be properly aligned on the stage. The choice of appropriate pass energy is crucial for high resolution data while achieving sufficient signal-to-noise ratios to properly analyze the data. Also, the use of a flood gun to neutralize the sample surface due to photoelectron escape is important in case of wide bandgap or insulating substrates such as $SrTiO_3$. After following the necessary steps, XPS data are collected in two different scan modes.

4.2.1.1 Survey Scan

A survey is a quick scan over the entire binding energy range accessible with the given X-ray wavelength. Al Kα line was used for the measurements, and range of the binding energy was -10

eV-1400eV. Survey scans contain all the peaks resulting from the elemental composition of the material. Therefore, survey scans are important to determine any contaminant present or absence of the element necessary for the desired material. An example of survey scan is shown in Figure 4.5.

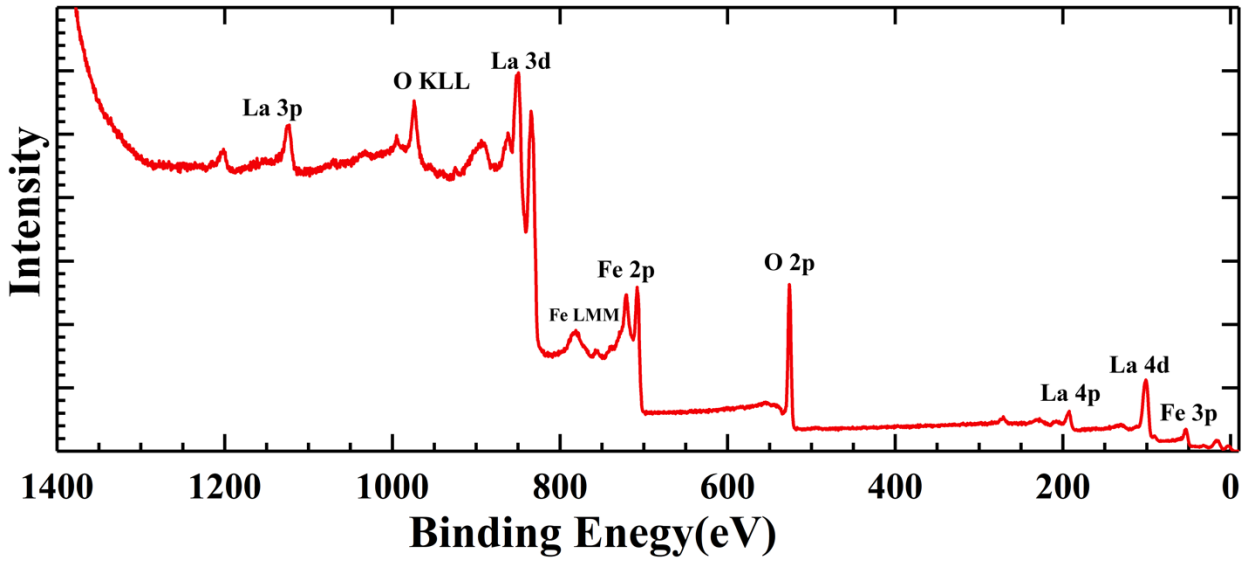

Figure 4.5: XPS survey of $LaFeO_3$ film on $SrTiO_3$ substrate. All possible peaks including Auger peaks that fall in the binding energy range of X-ray line can be observed.

For the thin films with thicknesses within the XPS probing limit, film thickness can be estimated from the relative intensity of the peaks from the substrate before and after the growth. Stoichiometry of the thin film can be estimated from the relative intensity of peaks corresponding to different elements. In particular, XPS survey scans accelerates the analysis of the thin films to improve a growth recipe.

4.2.1.2 Multiplex Scan

Multiplex scans take longer time and can provide more detailed information. To obtain better resolution a lower pass energy and smaller energy step is used compared to survey scans. Depending on the resolution of the multiplex data, spin orbit splitting or multiplet splitting might

be visible or those peaks can be deconvoluted by fitting with components. The area under the peak or components can be used to calculate stoichiometry. From the peak position of the individual components, the valence state can be determined and in the case of mixed valence state, the ratio of different valence state can be calculated.

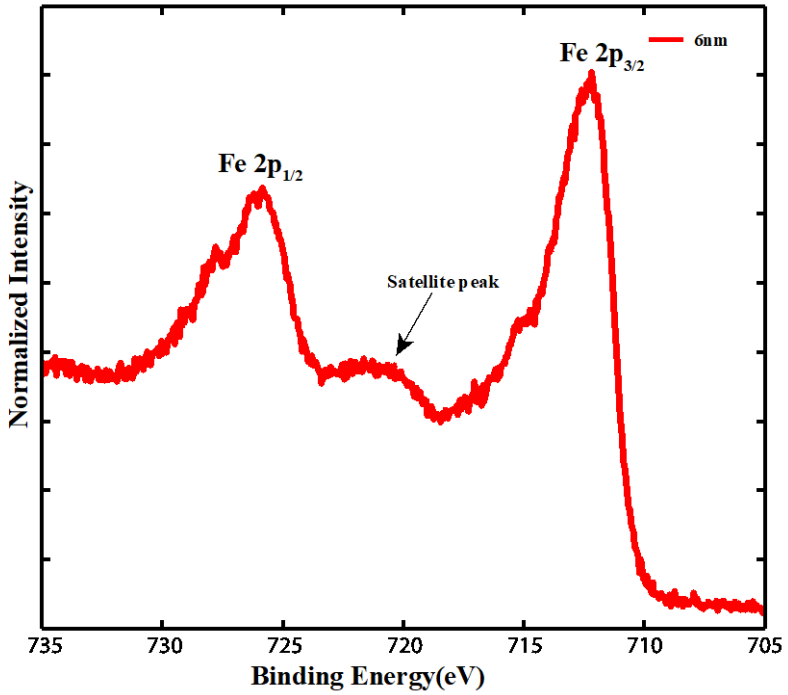

Figure 4.6: Fe 2p core level from $LaFeO_3$ film grown on Nb doped $SrTiO_3$. Fe 2p region shows clear spin-orbit splitting along with the satellite peak, which can be used to extract the information about valence state of Fe.

A multiplex scan of the Fe 2p core level from an LFO thin film is shown in Figure 4.6. The spin-orbit splitting is clearly visible with Fe $2p_{3/2}$ and $2p_{1/2}$ ~14.6 eV apart. These binding energies correspond to the Fe^{3+} valence state [137,138]. In addition to main peak there is a shake-up peak at the right shoulder of the $2p_{1/2}$ peak. This shake up satellite is signature of Fe^{3+} state, whereas Fe^{2+} shake-up satellite is shifted to lower binding energy [139]. Therefore, different peak features are very important to determine local bonding environment and thereby oxidation state.

Another important application of XPS is determination of the band offset at the heterostructure interface. In the heterostructure Fermi level of the two materials must be constant throughout the

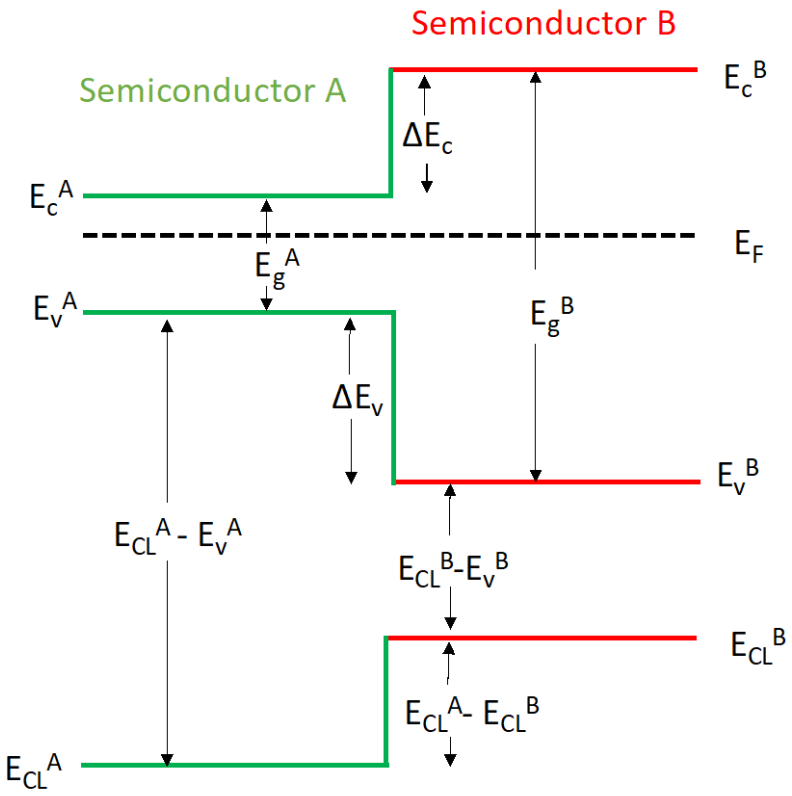

Figure 4.7: Band alignment at the interface of two semiconductor material. The band offsets are measured using flat band approximation.

system. Once the Fermi level between two semiconductors align themselves to be constant, the valence and conduction also realign themselves to produce a particular band alignment. The resulting difference in energy between valence bands and conduction bands are the band offsets. The band offset in heterostructures is crucial to predict the charge transfer between two materials at the interface. The band offset between two semiconductors is shown schematically in Figure 4.7. XPS allows us to precisely determine the core level binding energies and valence band

maximum (VBM) of the material. From this information the band offset can be determined using following equations, often referred as Kraut's method [140].

$$\Delta E_v = (E_{CL}^A - E_v^A) - (E_{CL}^B - E_v^B) - (E_{CL}^A - E_{CL}^B)$$

$$\Delta E_c = E_g^A - E_g^B - \Delta E_v$$

Where ΔE_v and ΔE_c are valence band offset and conduction band offset. E_{CL}^A and E_{CL}^B are the core level BE of two semiconductors. E_v^A and E_v^B are valence band maxima, similarly E_g^A and E_g^B are the band gaps. The valence band maxima are measured with respect to some core level energies in sufficiently thick films. And the difference in core level BE is measured in thin film heterostructure. This method works so well because the VBM measured with respect to core level remains constant regardless of any changes to the material [141]. Main challenge with this method is precise determination of VBM from valence band spectra. Rather simple method of linear extrapolation of valence band edge to the zero-background level have been found to work reasonably well compared to Kraut's original approach of fitting XPS valence band spectra with theoretical valence band density of states [142].

XPS measurement in all the samples was carried out *In-situ*, which enables measurement on pristine samples without any chemical changes due to exposure to atmosphere. *In-situ* XPS is very impactful in examining the surface and interface of as-grown samples and better understanding their properties

4.3 X-ray Diffraction

X-ray penetration depth in the solids is of the order of microns, therefore it is a bulk sensitive technique. X-rays are produced by interaction of energetic electrons with a target material, the X-

ray anode. When the electrons hit the target material there are two types of interaction i) electrons are decelerated by atomic core due to electrostatic interaction which produces continuous spectrum of X-Ray and ii) if the electrons have sufficiently high kinetic energy, they dislodge the core electrons and a subsequent transition to fill the core hole generates the X-ray characteristic spectrum. The characteristic spectrum consists of a mixture of several wavelengths and a monochromator is used to produce monochromatic X-ray filtering out unwanted wavelengths. Monochromatic characteristic spectrum is used for XRD measurements. The monochromatic beam is passed through the collimator to produce highly parallel beam of monochromatic X-rays. Conventional XRD uses the Cu K_α line which consists of K_{α_1} and K_{α_2} lines. High-resolution XRD is equipped with the ability to filter out K_{α_2} and uses only K_{α_1} line. This is achieved through diffraction of the X-rays off of two Ge crystals that are configured to satisfy the Bragg condition for only K_{α_1} wavelength. In this dissertation all the measurements are performed using and Cu K_{α_1} (1.54Å) X-ray.

When X-rays interact with solids, a mixture of photoelectrons, fluorescent X-rays, incoherently scattered X-ray and coherently scattered X-rays are produced. Only coherently scattered X-rays which satisfy Bragg's condition forming a diffraction pattern are analyzed in XRD [143]. In a crystal, atoms are arranged periodically in atomic planes separated by a distance d_{hkl}. Bragg's law states that only those scattered electrons interfere constructively, which satisfy the condition

$$2d_{hkl}sin\theta = n\lambda$$

Where θ is angle of incidence and λ is the wavelength of the X-ray. In a cubic crystal with lattice constant 'a', (*hkl*) atomic planes are separated by a distance

$$d_{hkl} = \frac{a}{\sqrt{h^2 + k^2 + l^2}}$$

Therefore X- rays can provide information about the crystallinity and the crystal structure. XRD measurements can provide variety of other information such as film thickness, surface roughness, and the orientation of the crystal.

4.3.1 High Resolution X-ray Diffraction

High resolution XRD uses only K_{α_1} , which has wavelength very close to K_{α_2} line but is twice in intensity and finer linewidth; therefore, can produce high resolution diffraction pattern than K_α line. We performed mostly out-of-plane HRXRD and X-ray reflectivity measurement for our work in this dissertation.

High resolution X-ray diffraction (HRXRD) is a non-destructive process to study crystalline materials. The Rigaku SmartLab system used in this work uses Cu $K\alpha_1$ source filtered appropriately for thin film samples using a parabolic mirror and double bounce Ge (220) monochromator. Measurements were carried out in 2θ-ω scans on the (001) reflection of the STO samples using a Malvern Panalytical X'Pert3 Diffractometer with a four-circle goniometer and a Cu $K\alpha_1$ radiation line isolated with a double bounce Ge (111) monochromator. Where ω is the angle of incidence and 2θ is the angle between incident and reflected X-ray. Parallel beam optics is used for thin film samples. In 2θ-ω mode X-ray source moves at angle ω and detector moves at an angle 2θ. The schematic of the XRD is shown in figure 4.8.

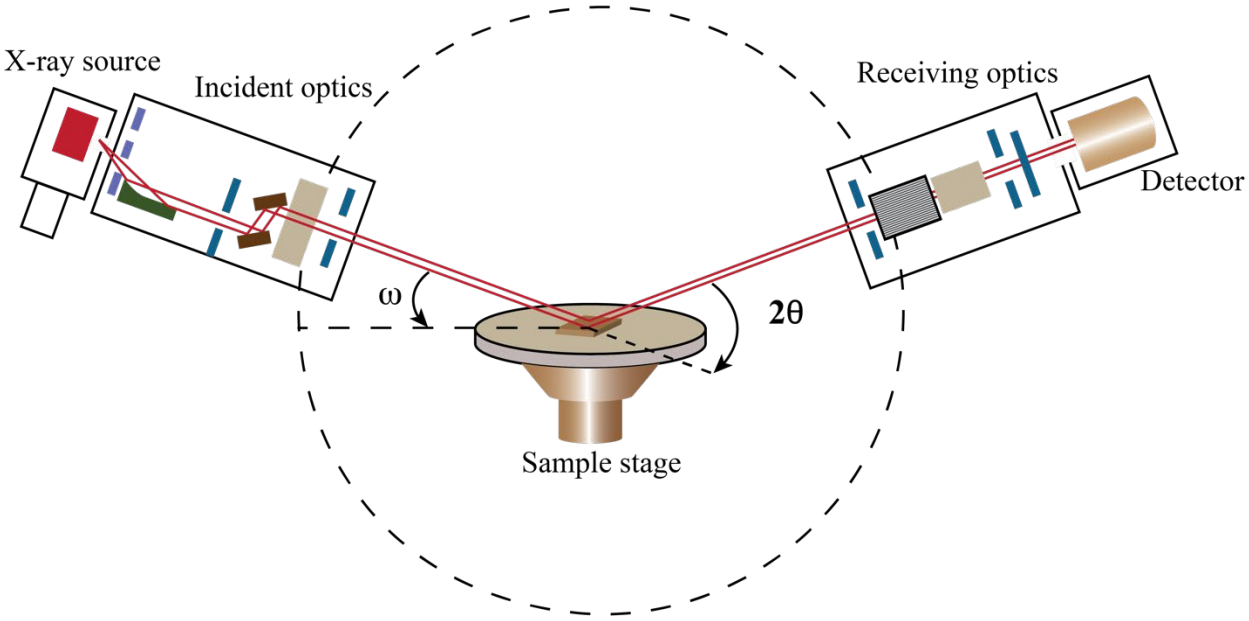

Figure 4.8: Schematic of high resolution XRD. Position of X-ray source is recorded as ω and detector position is 2θ. In 2θ-ω mode both source and detector move in a circle around the sample.

Out-of-plane diffraction is caused by either symmetrical or asymmetrical reflection from the atomic planes. Symmetrical reflection is obtained if the lattice planes are parallel to the sample surface and asymmetrical reflection is obtained if the atomic planes are tilted. The diffraction due to symmetrical reflection is intense and can probe deeper than in the case of asymmetrical reflection. This method is well suited to study thin films with homogeneous crystal orientation, to get the information about crystal structure and crystallographic orientation. The reflection from the (002) plane of LFO thin film on STO (001) substrate is shown in Figure 4.9 (a). As can be seen from the reflection peak of substrate and film, there is a lattice match and LFO crystal planes are parallel to the substrate. Additionally, there are interference fringes along with the main reflection peaks. Usually, the presence of these fringes is indication of highly crystalline film. The out of plane lattice parameter can be calculated by fitting these reflection peaks with suitable parameters.

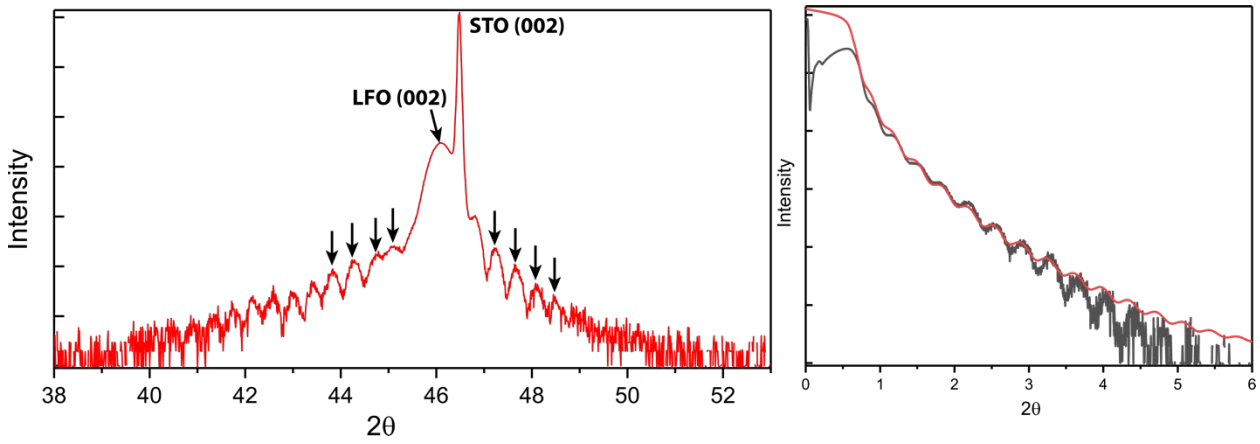

Figure 4.9: High resolution out of plane and X-ray diffraction pattern and reflectivity data for 20 nm $LaFeO_3$ film on Nb:$SrTiO_3$ substrate with thickness fringes labelled with arrows.

X-ray reflectivity is used to calculate thickness of the thin films. When X-ray are incident on the sample surface at a small angle gets reflected and as the angle is increased intensity of the reflected x-ray decreases rapidly. XRR technique analyzes interference pattern between X-ray reflected from surface and the interface. Therefore, XRR scans are over small range (0-6°) that is sensitive primarily to the film thickness. The reflection profile shows oscillation in intensity known a Kiessig fringes due to the interference between the X-rays reflected from the surface and the interface [144]. Period of these oscillations depend on surface roughness, film thickness and density of the material. The period of these oscillations gets longer for rougher films. Thicker films have shorter period of oscillations. The XRR curve of 20nm thick LFO film on STO (100) and it's fitting is shown in the Figure 4.9 (b). The thickness, density and roughness of the samples can be determined accurately by fitting the X-ray reflectivity curve.

4.4 Atomic Force Microscopy(AFM)

Atomic force microscopy (AFM) is powerful surface analysis technique. It can produce a high-resolution nanoscale image of the material surface topography. AFM uses a nanoscale tip mounted

on cantilever spring. A simplified sketch of the AFM system is shown in Figure 4.10. When the tip is brought very close (1-10 nm) to the sample surface the atoms at the tip sense force due to the electrostatic interaction with the atoms on the material surface. As the tip is scanned along the surface, the force experienced by the atoms in the tip changes due to topography variation, this information is used to get the topographic image of the surface.

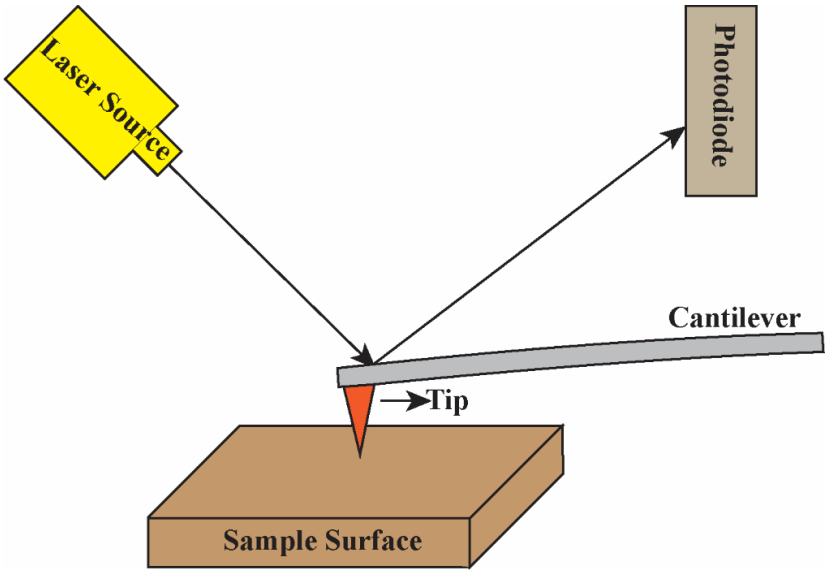

Figure 4.10: Atomic Force Microscopy system.

The AFM works in two different modes contact mode and non-contact mode. In contact mode, the tip contacts the surface and due to electrostatic interaction, the cantilever bends. A laser diode and photodetector is used to detect the bending. An electronic feedback loop is used to keep the force constant (bending constant) between tip and sample surface.

In non-contact or tapping mode, the cantilever vibrates at a mechanical resonance frequency. As the tip moves along the surface, the force between tip and the surface atoms changes due to topographical variation. This change in force changes the amplitude and the phase of the oscillation. The change in amplitude is detected using the laser diode and photodetector. An

electronic feedback loop monitors the force to keep the tip-sample separation constant. In both contact and non-contact mode the deflection of the tip is mapped to get the high-resolution topographic image of the surface.

Contact mode can often produce higher resolution images compared to non-contact mode but can be destructive to the thin film surfaces. Therefore non-contact mode was used to image the surface in this work. The AFM images in this work are obtained using a Park Systems' XE7 AFM, over area as large as 5 x 5 μm^2 to measure the root-mean-square (rms) surface roughness of the LFO and LNO thin films. The AFM images of the two different LFO sample is shown in figure 4.11.

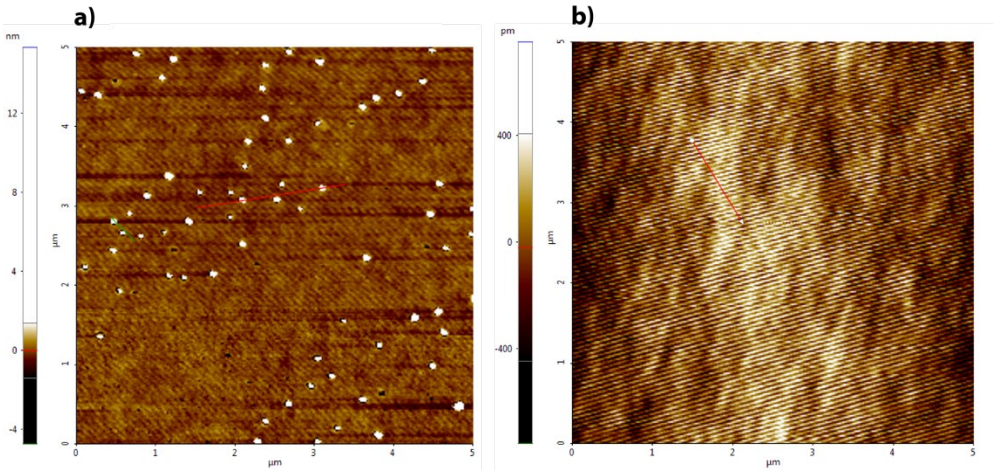

Figure 4.11: AFM images of LFO thin film a) with rough surface b) smooth surface.

One (Figure 4.11(b)) has a smooth surface, and another sample(Figure 4.11(a)) has a rough surface with secondary phases such as binary oxides. AFM is very helpful tool in assessing the film quality in the TMO thin films.

4.5 Scanning Transmission Electron Microscopy (STEM)

STEM can produce a real-space image of materials at atomic scale resolution. A beam of electrons is focused into a point probe of the size of 1Å using electron optics, which is sufficient to resolve interatomic distances in most of the crystal structures. The fine electron beam is scanned across the sample. Since STEM uses information from transmitted electrons to create the image, the sample cross section must be sufficiently thin to allow for the electron transmission through the material. The transmitted electrons are scattered by the atoms in the sample. The scattered electrons are detected using different detectors.

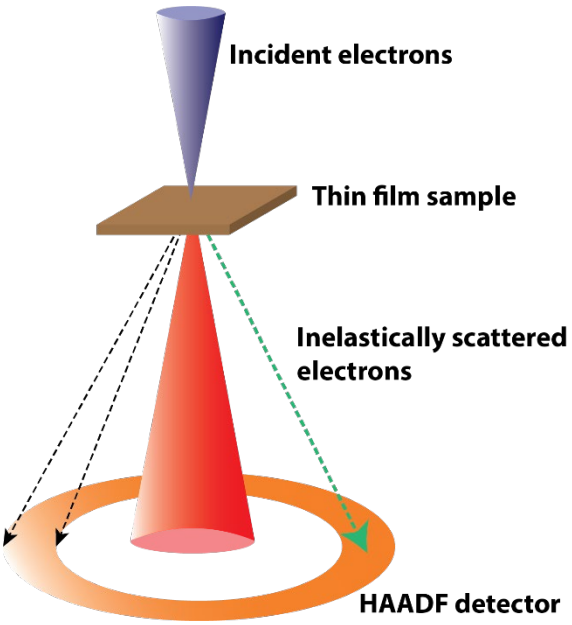

Figure 4.12: STEM imaging in HAADF mode. In this mode only the scattered electrons at high angle as indicated by orange circle are analyzed.

Based on the angular distribution of the scattered electrons used to produce images, it can be dark-field or bright-field as shown in Figure 4.12. In this work STEM images were produced using a high angle annular dark field detector. In HAADF mode only the electrons scattered at high angle are collected by the detector. The scattering of these electrons is like Rutherford scattering where

the intensity of scattered electrons is proportional to the square of atomic number(Z^2). Therefore, the heavier atoms appear brighter in a HAADF-STEM image. Electron energy-loss spectroscopy (EELS) coupled with STEM can produce elemental mapping which provides the information of chemical composition. From STEM images the lattice structure and defects present can easily be visualized. In the case of heterostructures interfacial cation mixing or misfit dislocations are apparent, which makes STEM-EELS an ideal tool to study thin films and heterostructures.

4.6 Cyclic Voltammetry (CV)

Cyclic voltammetry is an electrochemical technique to study redox chemistry in the material. Experimental setup of CV measurement consists of three electrodes as shown in Figure 4.13.

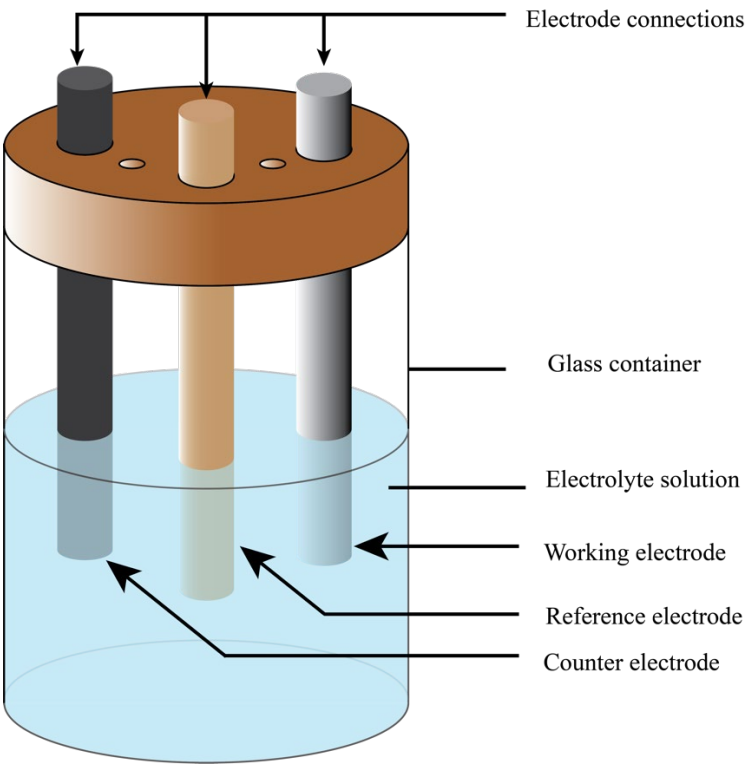

Figure 4.13: Three electrode system for Cyclic voltammetry measurement.

Acidic or basic electrolyte solution is used to provide path for electrons generated during oxidation or reduction process. The working electrode is where oxidation or reduction takes place. A reference electrode is used to measure potentials across other electrodes and standardize potential differences in the analysis. When oxidation or reduction takes place at the working electrode current flows due to electron transfer during the chemical reaction. The counter electrode completes the circuit so that electron can flow and current can be measured.

In this work the electrochemical measurements were performed by our collaborator at Auburn chemistry department. In order to measure the oxidation or reduction activity of the thin film samples they are mounted on the working electrode as shown in Figure 4.14. The working electrode is usually made up of glassy carbon. The thin film sample is attached on the glassy carbon electrode using gallium indium eutectic to get the conductive contact. Additionally, silver paint is applied around the eutectic's edge to hold the substrate in place. Epoxy is then used to seal the entire structure, leaving only the film surface exposed.

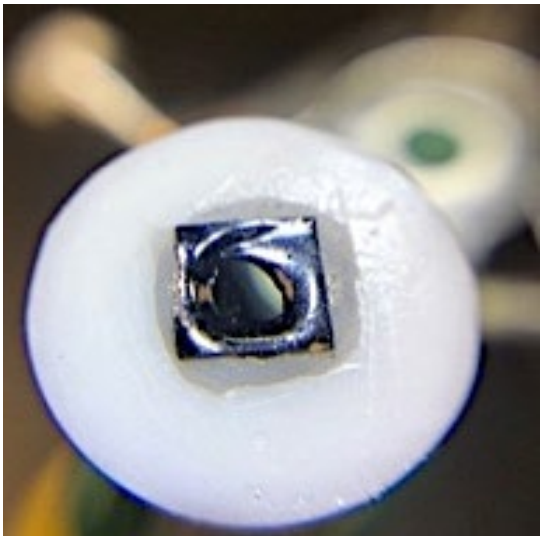

Figure 4.14: LFO thin film sample mounted on a glassy carbon working electrode.

For data acquisition potential is applied externally through a potentiostat and the resulting current is measured. Cyclic voltammetry is an important tool to study the beahvior of oxide thin films as well as interfaces under electrochemical process for their application in renewable energy technology.

4.7 Electrochemical Impedance Spectroscopy (EIS)

EIS helps understand the charge transfer process across the various interfaces under electrochemical process. The experimental set up for EIS measurement is similar to that of CV. The frequency of input ac signal is varied and change in impedance as a response is measured. The analysis is done using Nyquist plot and Bode phase plot. Typical Nyquist plot and Bode phase plot is shown in Figure 4.15.

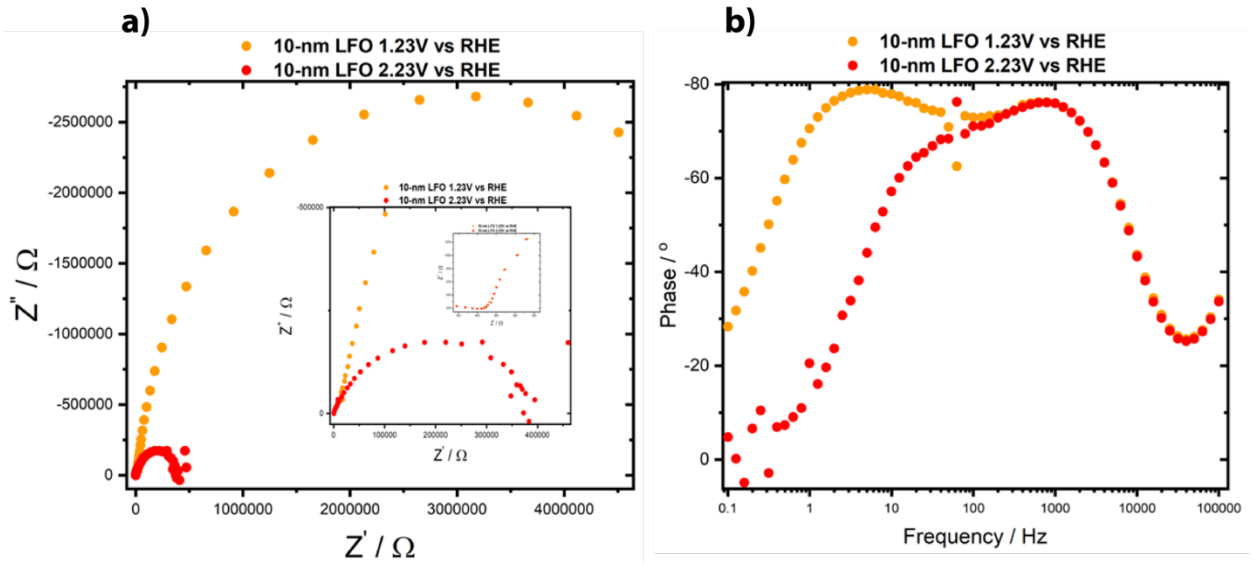

Figure 4.15: a) Nyquist plot and b) Bode phase plot of 10nm thick LFO-Nb:STO thin film.

The Nyquist plot is the is the plot of real and imaginary part of the impedance, which is fitted with Randle's circuit to extract the information about impedances due to different interfaces or

contacts [145]. The bode phase plot is the plot of phase of the output signal vs frequency. Depending on the nature of the interface or charge transfer, it will exhibit different peak features or peak shifts for different potentials. Combination of Nyquist and Bode plot can elucidate the charge transfer mechanisms across the various interfaces.

Chapter 5

Perovskite Oxide Thin Film Properties and Their OER Activity

Portion of this chapter are extracted from *Burton et al.* published in ***Journal of Materials Chemistry A***, 2022, **10**, 1909-1918 DOI: 10.1039/d1ta07142d with permission of the publisher.

5.1 Lanthanum Ferrite ($LaFeO_3$)

5.1.1 Structural and Magnetic Properties

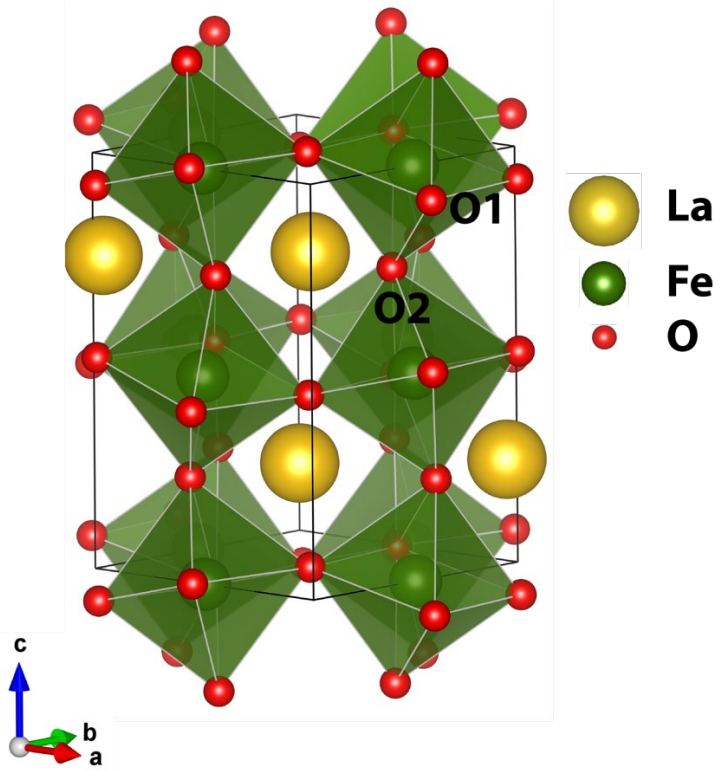

Figure 5.1: Orthorhombic LaFeO3 unit cell. The FeO_6 octahedra tilting distorts from the ideal cubic structure quadrupling the unit cell volume.

$LaFeO_3$ is an orthorhombic wide band gap semiconductor with AFM-G type antiferromagnetic phase at the ambient condition. Its orthorhombic perovskite structure is shown in Figure 5.1. Lanthanum ferrite assumes Orthorhombic structure with Pnma space group and G-type

antiferromagnetic phase in ambient condition [146]. Experimental lattice parameter are a=5.557Å, b=5.565Å and c=7.854Å [147]. First principles calculations using density functional theory predicts the orthorhombic structure with a=5.549Å, b=5.563Å and c=7.873Å, which is in good agreement with the experimental data. The tolerance factor (TF) for LFO is 0.954 [148], and for this value of TF orthorhombic is the stable structure. A site is occupied by La^{3+} cations and B-site is occupied by Fe^{3+} cations. B-site is 6-fold coordinated with oxygen, and due to octahedra tilting there are two inequivalent oxygen sites O1 and O2. Glazer notation for octahedra tilting for orthorhombic structure is $a^+b^-b^-$ [149]. The lattice parameter of orthorhombic structure due to octahedra tilting relates to its pseudo-cubic structure as $a=\sqrt{2}a_{pc}$ $b=\sqrt{2}a_{pc}$ and $c=2a_{pc}$. $LaFeO_3$ structure also evolves in symmetries with temperature. $LaFeO_3$ changes its orthorhombic Pnma symmetry to rhombohedral $R\bar{3}c$ at 1228 K and transforms to $Pm\bar{3}m$ cubic symmetry is predicted at 2140 K [150].

The antiferromagnetic behavior in LFO is due to the spin ordering in Fe^{3+} cations. Five 3d orbital electrons are distributed as $t_{2g}^3e_g^2$ in high spin state [151]. And the super-exchange interaction through Fe-O-Fe bonds results in antiferromagnetic alignment [152]. Magnetic behavior is also temperature dependent. The antiferromagnetic phase changes to paramagnetic at 735 K [150]. Spin polarized DFT calculations of the orthorhombic LFO structure also shows the antiferromagnetic phase.

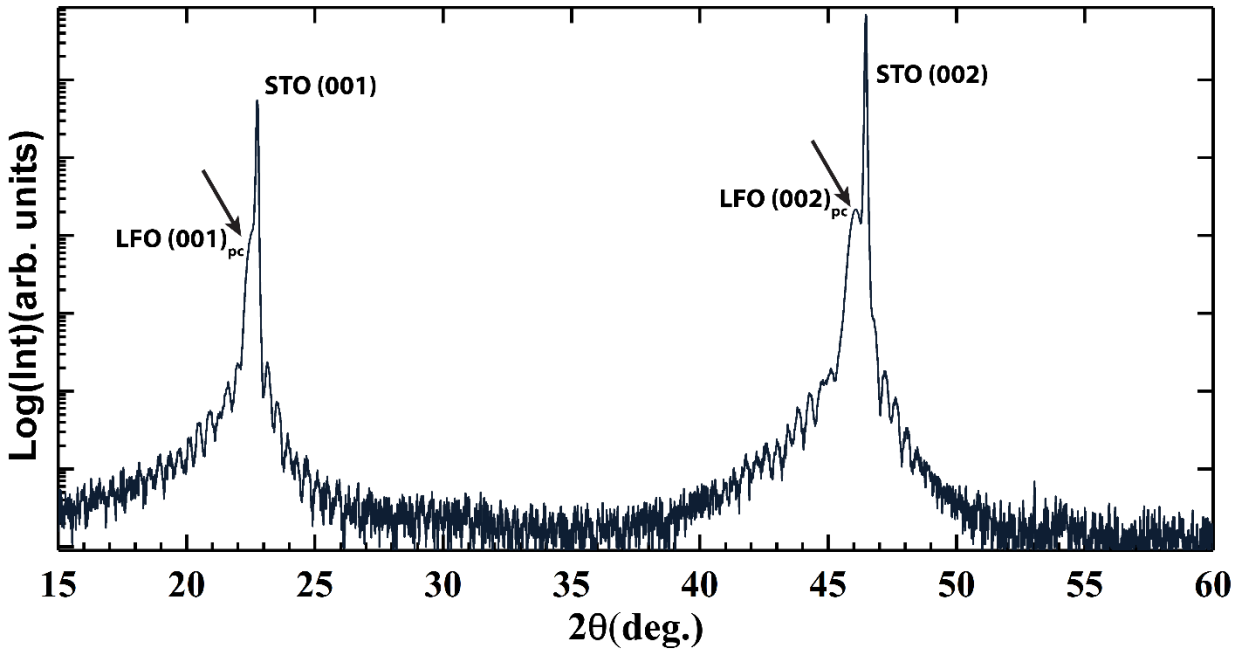

Figure 5.2: Out of plane high resolution XRD data for LFO thin film grown on (001) Nb:STO substrate.

LFO thin films are grown on $SrTiO_3$ substrate, which is a cubic perovskite. The lattice mismatch between LFO (a_{pc} =3.93Å) and STO (a_{pc}=3.905Å) is ~0.6% therefore, epitaxial LFO thin films are coherently strained. The out-of-plane X-ray diffraction data shown in Figure 5.2 confirms the lattice match between LFO thin film and STO substrate. The well-defined thickness fringes implies that the LFO samples have high crystallinity. We can see two peaks from cubic Nb:STO substrate (001) and (002). The (001) and (002) peaks from pseudo-cubic LFO thin films overlaps with STO diffraction peaks. Therefore, LFO sample grown on STO substrate have pseudo-cubic structure.

5.1.2 Bulk and Surface Electronic Properties

$LaFeO_3$ is a wide band gap semiconductor with experimental band gap 2.3 eV [153]. It is an intrinsic semiconductor as Fermi energy resides in the mid-gap [154]. Crystal field leads to splitting of 5-fold degenerate Fe 3d band into 3-fold degenerate t_{2g} and 2-fold degenerate e_g states. The ground state electronic configuration is $t_{2g}^3 e_g^2$. The electronic band structure and density of states using the first principles calculations are shown in Figure 5.3.

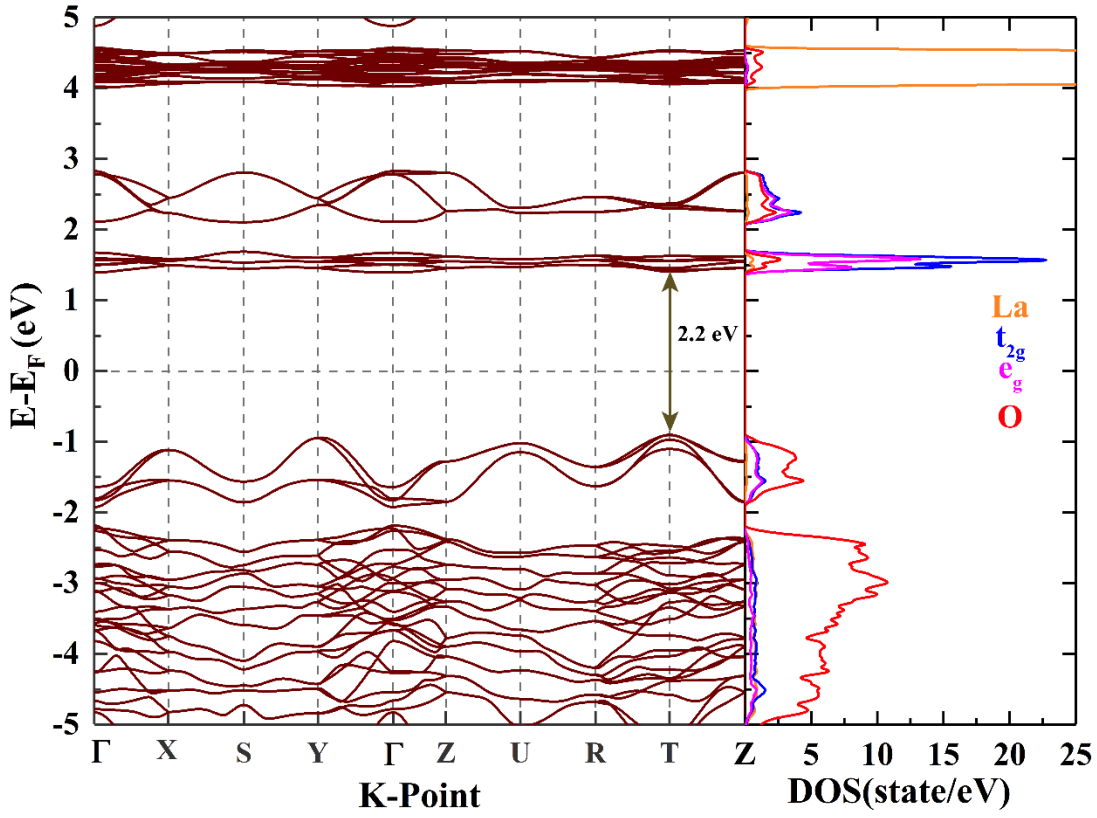

Figure 5.3: Ground state electronic structure and density of states projected onto different atoms and orbitals of $LaFeO_3$.

The valence band edge is formed by mostly oxygen 2p states hybridized with unoccupied t_{2g} and the deep oxygen 2p bands are separate from bands near the Fermi energy. The conduction band near the Fermi energy is mostly formed of occupied t_{2g} states. The valence band maximum and

conduction band minimum lie at T point resulting in direct band gap of 2.2 eV. Some groups have reported that conduction band minimum lies at Γ point which is below 0.01eV than the CBM at T point, but our calculations reveal otherwise [153].

5.1.3 Thin Film Synthesis

There are several approaches to grow thin films. Depending on the technique employed films could be amorphous, polycrystalline to single crystals. We focus our discussion on epitaxial single crystal thin films. MBE and pulsed laser deposition are the most advanced techniques that allows control the thin film in atomic level. For layered structure such transition metal perovskites it is easy to control the film termination and dope uniformly throughout the sample with these techniques.

LaFeO3 thin film samples were synthesized using molecular beam epitaxy (MBE) in layer by layer growth mode. LFO thin films of varying thicknesses were grown on commercially available 0.7% Niobium doped $SrTiO_3$ substrates. Individual metallic fluxes were obtained by heating metallic source in high temperature effusion cell. The RHEED image along of the $LaFeO_3$ thin film along [110] is shown in Figure 5.4.

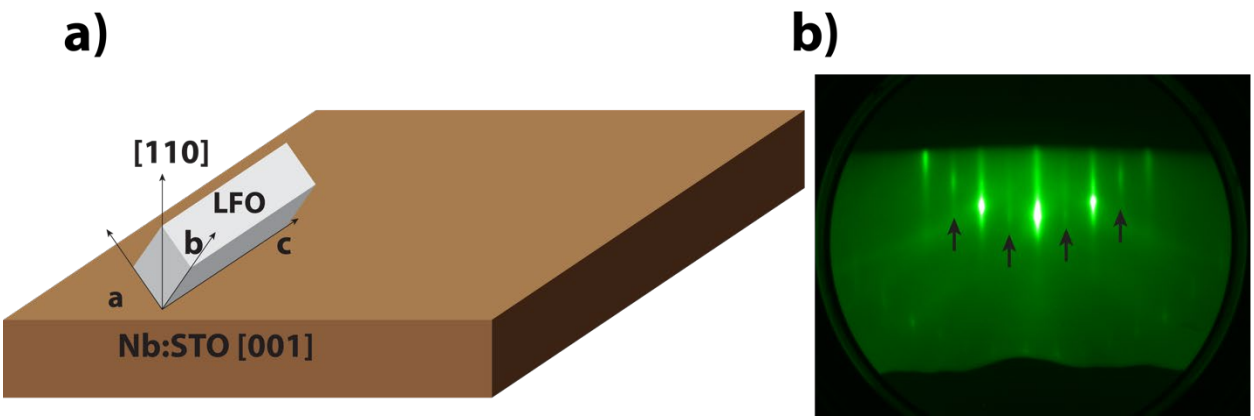

Figure 5.4: a) Schematic of the LFO unit cell orientation on (001) Nb:STO substrate. b) RHEED image of the LFO samples, arrows indication the c(2×1) reconstruction.

The RHEED images of the thin film sample is very sharp indicating stoichiometric film with high crystallinity. There are additional streaks in between major diffraction spots as indicated by the arrows in Figure 5.4 (b), which is due to c(2×1) reconstruction. This reconstruction suggests that the c axis of the orthorhombic LFO is parallel to the substrate surface and $(001)_{STO} \parallel (110)_{LFO}$ as shown in the Figure 5.4 (a). Clear intensity oscillation was observed in RHEED confirming layer by layer growth.

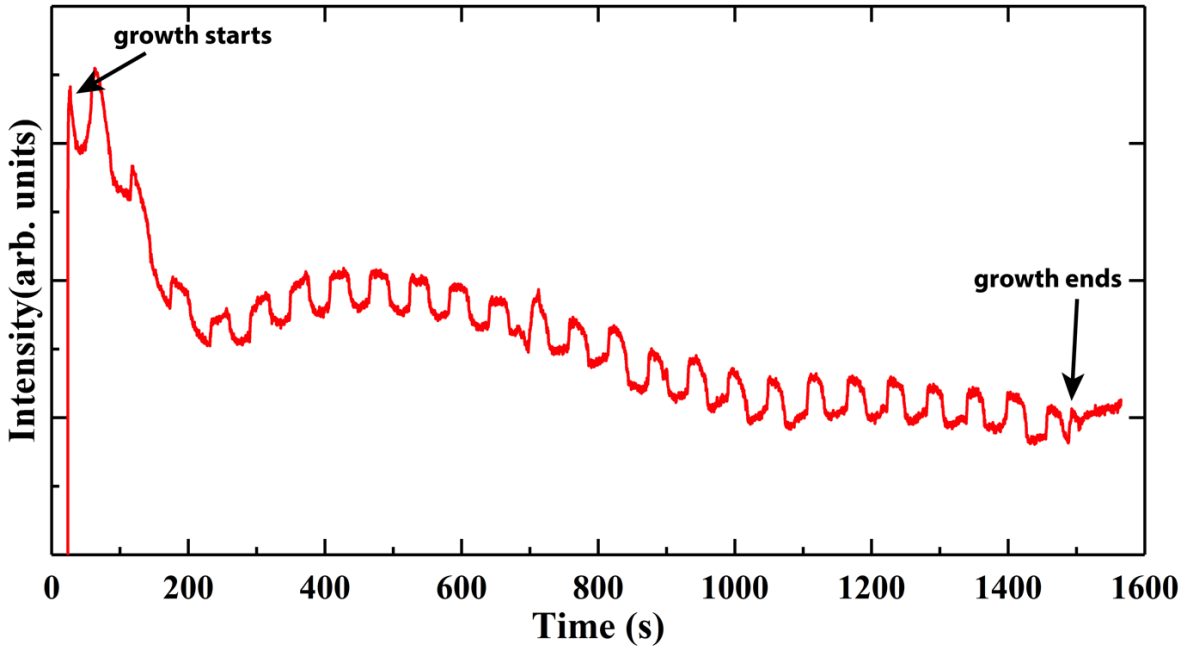

Figure 5.5: RHEED intensity oscillation for 10nm LFO-NbSTO film. Where each oscillation corresponds to one unit cell of the material

RHEED intensity oscillation of 10nm thin film is shown in Figure 5.5. Each period of oscillation corresponds to one unit cell. This is how we controlled the thickness of the film. We used XRD reflectivity data to confirm the thickness predicted by RHEED, and they agree within the error margin of one unit cell.

5.1.4 Application as a OER Catalyst

Perovskite ferrites with bandgap falling in visible light spectrum range have been investigated for their potential applications in photovoltaics and optoelectronic devices [155–157]. $LaFeO_3$ is one of the newest and least investigated candidates among perovskite ferrites. Based on the intrinsic properties of LFO and available descriptors LFO is potentially a good candidate for OER catalyst [8,33]. There are some literatures that report photocatalytic OER activity of $LaFeO_3$ and results are promising [35,158,159]. LFO intrinsic electronic structure can be tuned easily by

doping or by making heterostructure. Moreover, the high abundance and low cost of these elements makes it more relevant from the commercialization perspective.

5.1.5 Thickness dependent OER electrocatalysis of $LaFeO_3$ thin films

5.1.5.1 MBE Synthesis and Thin Film Characterization

MBE synthesis was performed in an ultra-high vacuum system (Mantis Deposition, base pressure = $5x10^{-9}$ Torr) to achieve high purity in the resulting samples. *In situ* RHEED analysis was used to monitor the growth process. Commercially available (001)-oriented 0.7% Nb-doped $SrTiO_3$ (n-STO, MTI Crystal) 10 mm x 10 mm substrates were used. The small lattice mismatch (-0.6%) and conductive nature of n-STO makes it ideal as a conductive substrate suitable for catalysis measurements. Before loading into the growth chamber, n-STO substrates were sonicated for 10 minutes in acetone (ACS grade, VWR) and isopropanol (ACS grade, VWR) and dried with N_2 gas (Airgas, 99.999%) to produce a clean surface. La (ESPI, 99.9%) and Fe (Sigma Aldrich, 99.98%) flux were supplied through individual high temperature effusion cells. The cell temperatures for La and Fe were approximately 1550 °C and 1350 °C respectively. The oxygen flow was set to 0.2 sccm (Airgas, 99.999%) during the entire growth and an RF plasma source operated at 300 W was used to supply atomic oxygen. Pressure in the chamber during growth was $3x10^{-6}$ Torr. The *n*-STO substrate was heated to 700 °C in oxygen plasma before growth to remove hydrocarbons and recover a well-defined surface as observed by RHEED. A shuttered growth process was employed to synthesize the samples at 700 °C. [160,161] By programming individually controlled shutters, La and Fe fluxes were deposited alternately with a growth rate of ~80 seconds per unit cell. Samples were cooled in the presence of oxygen plasma until ~200 °C to promote full oxidation of the LFO film.

Epitaxially grown samples were then transferred to an appended X-ray photoelectron spectroscopy chamber (PHI 5400, refurbished by RBD Instruments). The XPS system is attached to the MBE system by a vacuum transfer line to preserve pristine surfaces for post-growth characterization. A monochromatic Al K-alpha X-ray source was used for measurement. A low energy electron flood gun (neutralizer) was used for charge compensation. All the XPS peaks were adjusted by shifting the O 1*s* peak to 530 eV. [136] Following XPS, 10 mm x 10 mm n-STO/LFO samples were diced into (4) 5 mm x 5 mm samples for electrocatalysis and microscopy measurements. Post-growth high resolution X-ray diffraction (HRXRD) was performed using a Rigaku SmartLab system with a Ge (220)x2 incident beam monochromator and hybrid pixel area detector in 0D mode to obtain out-of-plane diffraction and X-ray reflectometry scans.

5.1.5.2 Scanning Transmission Electron Microscopy

Cross-sectional scanning transmission electron microscopy (STEM) samples were prepared using a FEI Helios NanoLab DualBeam Ga^+ Focused Ion Beam (FIB) microscope with a standard lift out procedure. STEM high-angle annular dark field (STEM-HAADF) images were collected on a probe-corrected JEOL GrandARM-300F microscope operating at 300 kV, with a convergence semi-angle of 29.7 mrad and a collection angle range of 75–515 mrad. STEM electron energy loss spectroscopy (STEM-EELS) mapping was performed using a 0.25 eV ch^{-1} dispersion for fine structure measurements, yielding an effective ~0.75 eV energy resolution, and using a 1 eV ch^{-1} dispersion with a 4× energy binning in the dispersive direction for composition maps. Data was collected in the DualEELS mode to correct for energy drift and no denoising was applied.

5.1.5.3 OER Electrocatalysis

n-STO/LFO (5 mm x 5 mm diced) samples were fabricated into electrodes using a rotating disk glassy carbon electrode (GC, Pine Instruments). Indium gallium eutectic (InGa, Ted Pella #**495425**) was used to form an electrical contact between the backside of the n-STO substrate and the GC electrode. A ring of silver paint (Sigma Aldrich) was placed around the InGa eutectic to serve as a binding agent between the n-STO substrate and the GC surface. Chemically inert epoxy (Loctite D609) was then used to cover the edges of the n-STO substrate and GC electrode, leaving only the LFO surface exposed to solution.

Cyclic voltammetry (CV) experiments were performed with a Pine WaveDriver 20 bipotentiostat using a three-electrode setup. The working, reference, and counter electrodes for the electrochemical setup were n-STO/LFO, Hg/HgO (0.1 M NaOH, Pine Instruments), and platinum wire respectively. All measurements were performed under saturated O_2 conditions in water (18 MΩ, Millipore) with 0.1 M KOH electrolyte while rotating the working electrode at 2000 rpm to remove bubbles from the surface. CV experiments were performed by sweeping the potential at 20 mV s^{-1} from 0.80 to 2.23 V vs RHE for 25 cycles to equilibrate the electrode surface. The anodic scan of the 25th cycle was used for analysis of electrocatalytic performance. All potentials were iR compensated by measuring the solution resistance before each measurement.

Electrochemical impedance spectroscopy (EIS) was performed at designated applied potentials using a Gamry 1010E potentiostat with a 5 mV modulation voltage. The modulation frequency was scanned from 0.1 Hz to 100 kHz.

5.1.5.4 Results and Discussion

The RHEED pattern for the 6 nm LFO sample after cooling to ambient temperature is shown in Figure 5.6 (a). The sharp RHEED image taken along the [110] direction suggests the film is a

single crystal with the perovskite structure. The absence of any modulation in the streaks in the RHEED image indicates a smooth surface with roughness comparable to the original substrate. Films show a c(2x1) surface reconstruction consistent with stoichiometric La-based perovskite films [162]. *In situ* XPS analysis was performed to determine the valence state of Fe and the film compositon. The Fe 2p XPS peak is shown in Figure 5.6 (b). The Fe 2p XPS region has two separate peaks corresponding to $2p_{1/2}$ and $2p_{3/2}$ due to spin multiplet splitting. An additional satellite peak close to the right shoulder of the $2p_{1/2}$ peak is an indication of the Fe^{3+} valence state [163], while for Fe^{2+} valence the satellite moves towards lower binding energies. Chemical composition analysis was done by comparing the area ratio under La 4d and Fe 2p peaks and were consistent with stoichiometric LFO. The LFO samples were also studied for film thickness and crystallinity using HRXRD. Out-of-plane HRXRD data is shown in Figure 5.6 (c). and shows single phase films with peaks consistent with epitaxial films oriented along the [001] pseudocubic direction. All films exhibit a primary diffraction peak consistent with an out-of-plane lattice constant of ~3.93 Å, though precise determination is challenging for the thinnest samples. Presence of thickness fringes alongside the main peak is indication of high crystallinity.

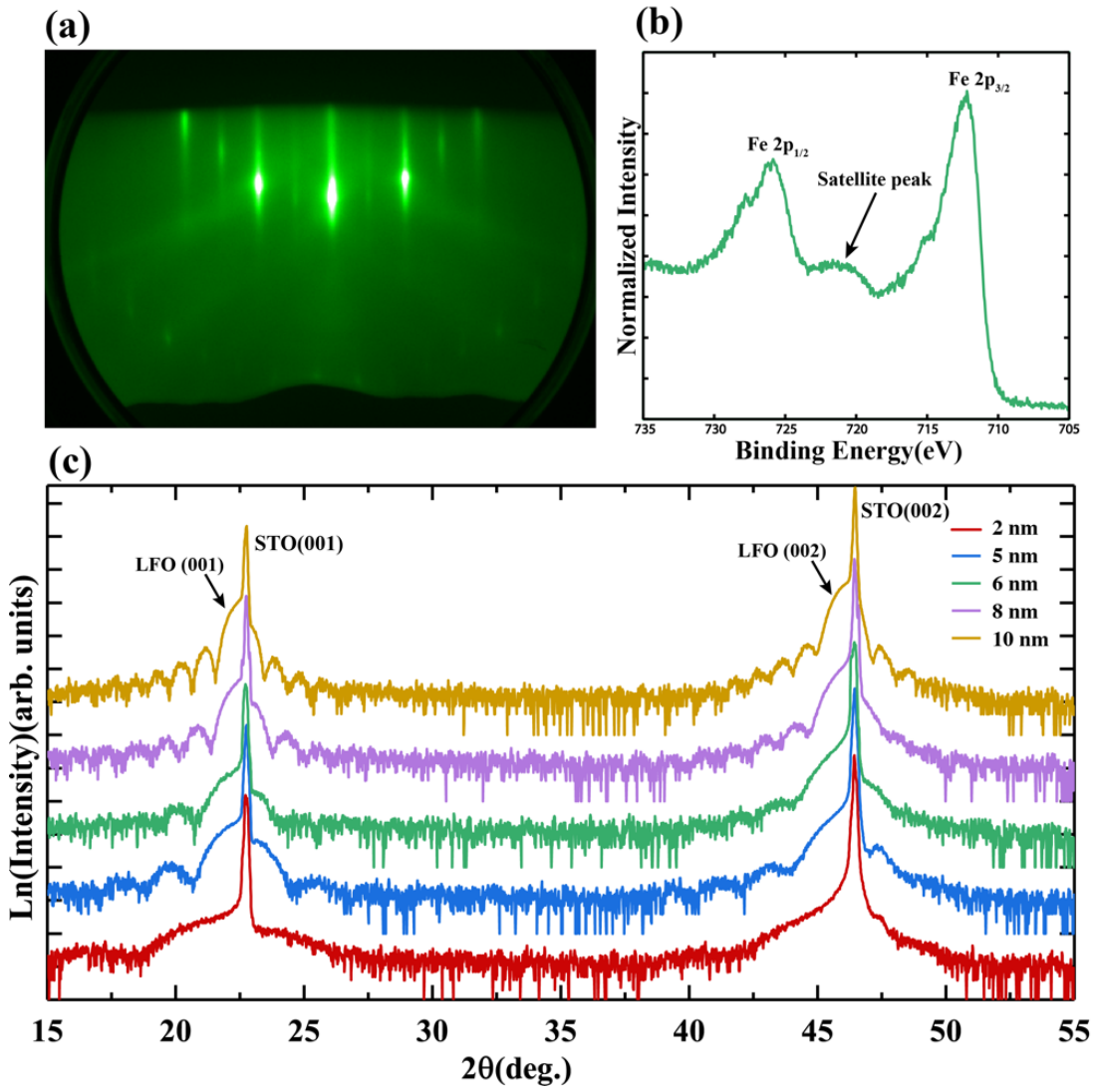

Figure 5.6: a) RHEED pattern of a 6 nm LFO thin film sample along the [110] of the *n*-STO substrate. (b) Fe 2p XPS region for 6 nm LFO. The satellite on the right side of the of Fe $2p_{1/2}$ is a signature of the Fe^{3+} valence state. (c) Out of plane HRXRD for n-STO/LFO samples of different thicknesses.

Figure 5.7 shows CV data collected for LFO films of different thickness. These data were obtained following 25 cycles of the potential range (0.80 - 2.23 V vs RHE). The catalytic current density

observed at 1.6 V vs RHE (η_{OER} = 0.37 V) increased from 0.8 μA cm^{-2} for 2 nm LFO to a maximum of 55.6 μA cm^{-2} for 6 nm and then decreased to 2.7 μA cm^{-2} for 10 nm (Figure in inset).

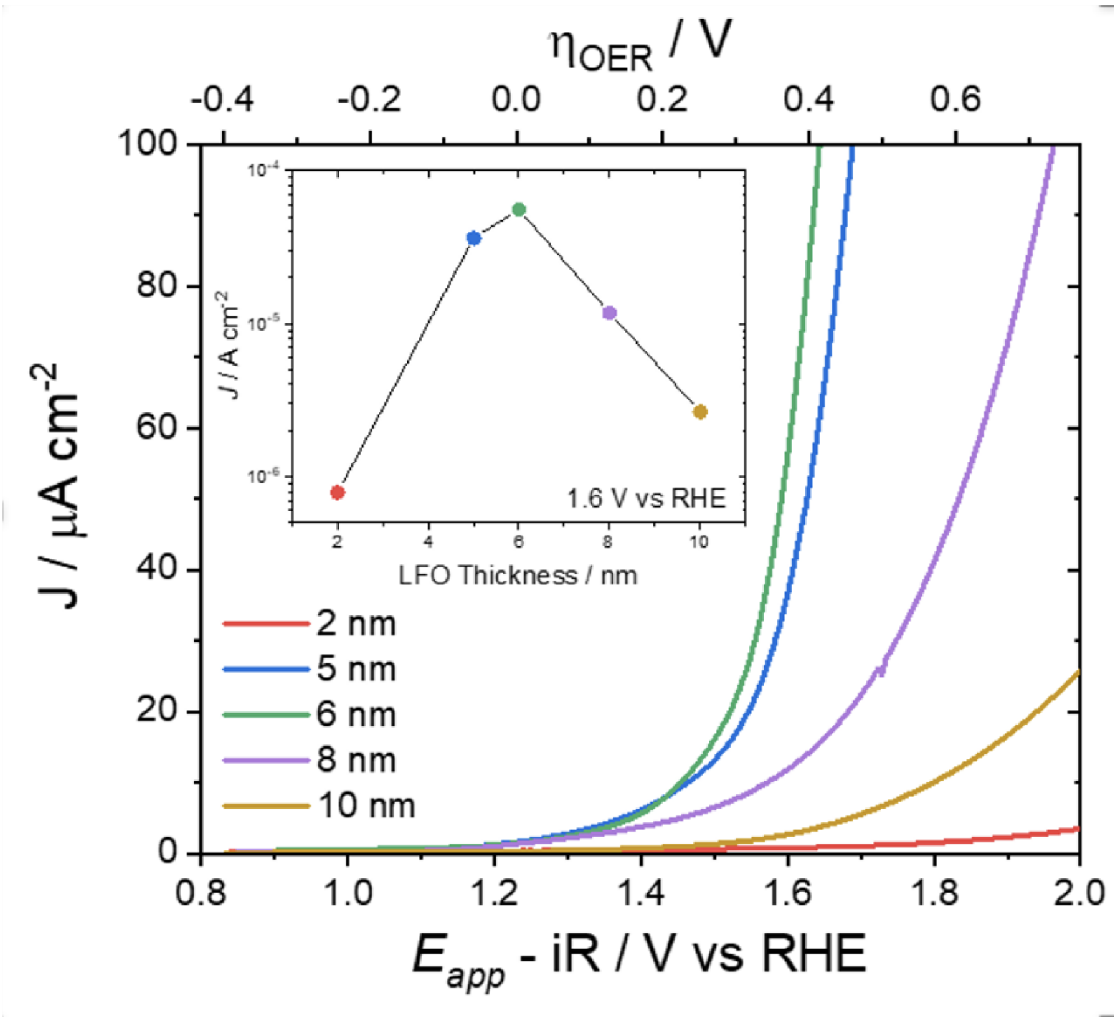

Figure 5.7: Anodic scans obtained from CV for n-STO/LFO films of different thickness. Data collected in O2 saturated 0.1 M KOH aqueous electrolyte at 20 mV s-1 scan rate and 2000 rpm rotation. (Inset) Current density measured at 1.6 V vs RHE as a function of LFO thickness.

In order to gain further understanding of the LFO thickness dependence, EIS was performed for each electrode for a selection of applied potentials. Figure 5.8 (a)-(d) shows Nyquist and Bode-

phase plots comparing 1.23, 1.63, and 2.23 V for 6 nm LFO where multiple features can be observed.

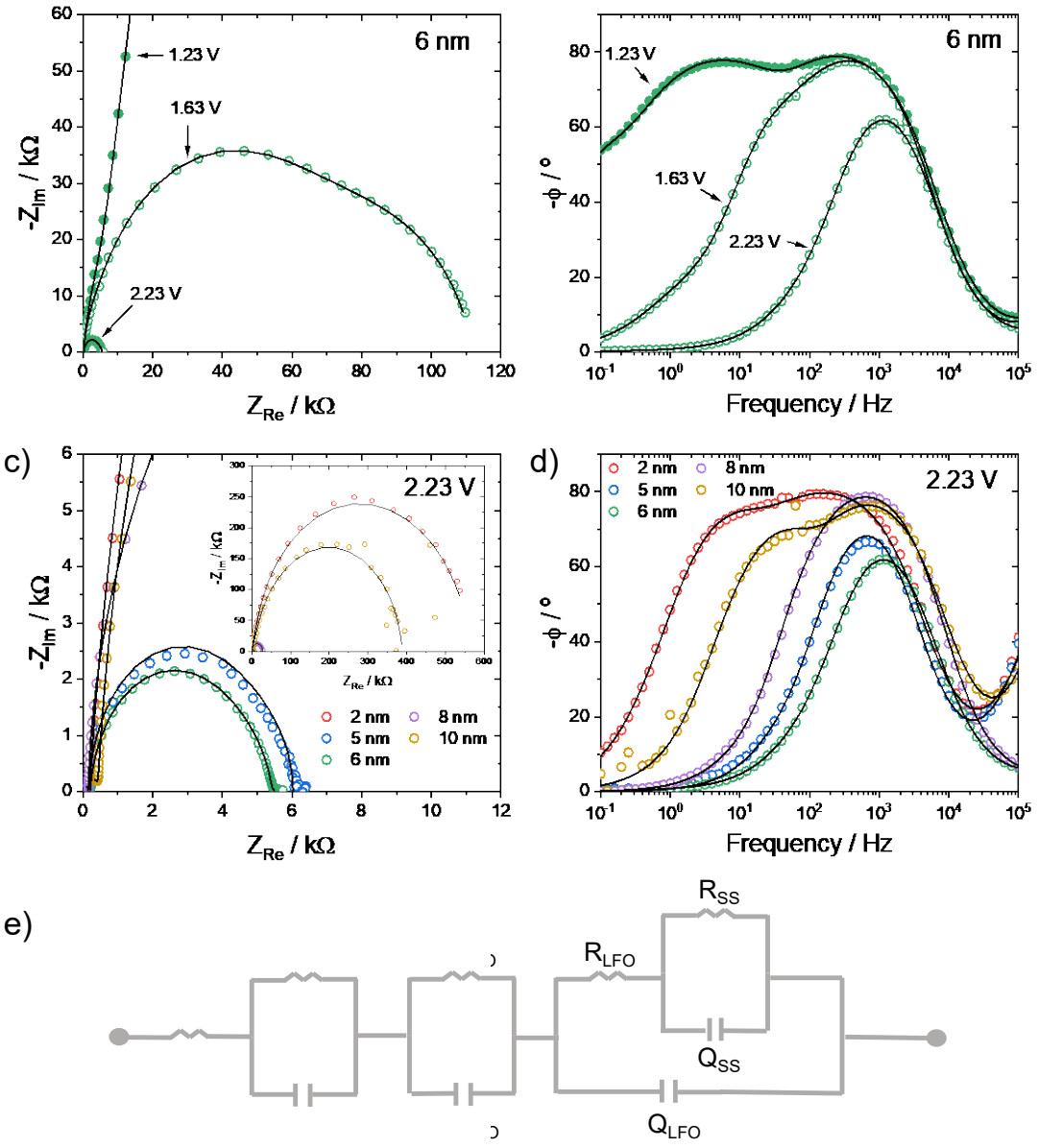

Figure 5.8: a) Nyquist and b) Bode-phase plots for 6 nm LFO measured at 1.23, 1.63, and 2.23 V vs RHE in 0.1 M KOH aqueous electrolyte (satd. O2). c) Nyquist and d) Bode-phase plots for 2,

5, 6, 8, and 10 nm LFO films measured at 2.23 V vs RHE. e) Equivalent circuit used to fit experimental data and generate overlaid lines.

Accurate modeling of the data was obtained with the equivalent circuit model shown in Figure 5.8 (e). In the circuit model to fit the EIS data liquid/liquid interface of the reference electrode/electrolyte is represented by (R_{ref}, Q_{ref}) and the solid/solid interface of *n*-STO/LFO by (R_{STO}, Q_{STO}) respectively. Similarly (R_{LFO}, Q_{LFO}) represents LFO/electrolyte interface and (R_{SS}, Q_{SS}) represents the surface states.

EIS experiments were also used to produce Mott-Schottky plots for determination of the flat band potential (E_{fb}) at the LFO/electrolyte interface. For thicknesses of 5-10 nm, these plots revealed negative slopes indicative of *p*-type behavior with an average E_{fb} = 1.38 ± 0.12 V vs RHE. Interestingly, E_{fb} was found to be -0.19 V vs RHE for 2 nm LFO and indicated *n*-type behavior based on the positive slope.

Given the large VBO at the *n*-STO/LFO interface and implication of surface state driven catalysis, questions arise regarding the structural and electronic variations throughout the depth of the LFO films. To examine these properties, STEM imaging and STEM-EELS measurements were performed on 6 nm samples with and without electrocatalysis experiments. Figure 5.9 shows STEM high-angle annular dark-field (HAADF) imaging performed on these films for the pre-electrocatalytic and post-electrocatalytic conditions to investigate atomic changes at the surface induced by electrocatalysis. In this imaging mode, image intensity is proportional to atomic number ($Z^{\sim 1.7}$), so the heaviest La atom columns are brightest, and contrast can be directly interpreted to visualize film defects and potential mass loss at the sample surface. The as-grown film quality for the pre-electrocatalysis sample is excellent, with a smooth surface and no extended

defects. Intermixing over several unit cells is present between the strontium and lanthanum atoms at the n-STO/LFO interface. Following electrocatalysis, we observed no substantial change in the n-STO/LFO interface and very little change at the LFO surface with only 1-2 u.c. steps present over large regions after treatment. Such small changes following exposure of the film surface to alkaline conditions and subjecting them to applied potentials reflects the stability of the MBE films during electrocatalysis. In addition, there is no evidence for a new phase in the treated sample, which would manifest in an interruption in the uniform crystalline structure if it formed during electrocatalysis.

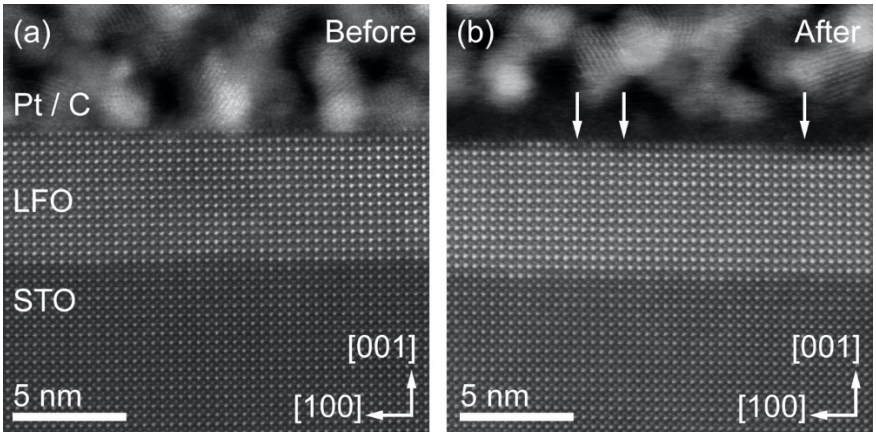

Figure 5.9: (a-b) Comparison of cross-sectional, high-magnification STEM-HAADF images of sample surface before and after treatment, respectively. Arrows indicate potential mass loss at the surface.

We also performed STEM-EELS measurements to explore chemical changes after electrocatalytic experiments described above. A comparison of composition maps of the before and after samples is shown in Figure 45.10 (a) and Figure 5.10 (d), respectively. Both maps are similar, with mixing on both the *A*- and *B*-site sublattices over ~1 u.c. at the interface. High-resolution O *K* and Fe $L_{2,3}$ edge spectra were collected from regions 1-3, corresponding to the interface, bulk, and surface of

the samples, respectively. The O *K* edge shown in Figure 5.10(b) contains the expected three features: a pre-peak (labeled **a**), main peak (labeled **b**), and secondary peak (labeled **c**), which result from the hybridization of O 2*p* states with *B*-site 3*d*, La 5*d*, and *B*-site 4*sp* bands, respectively. [164] The overall line shape is comparable to prior work in the literature, [165] with a redistribution of the weight of peak **c** to slightly higher energy loss moving from the surface (region 3) to the interface (region 1). A similar line shape is observed in the sample after cycling, as shown in Figure 5.10 (e); however, in this case, there is a more pronounced pre-peak feature **a**nd shift of main peak **b** to lower energy loss near the interface. Importantly, while the line shape varies only slightly throughout the untreated sample, it changes significantly near the surface of the treated sample, with a merging of pre-peak and main peak features. This finding points to possible electrocatalytically induced changes in the oxygen environment and agrees with the microstructural changes observed in Figure 5.9. Furthermore, these changes may even be responsible for OER catalysis based on the surface state model discussed for EIS data above.

Inspection of the Fe $L_{2,3}$ edge (Figure 5.10 (c) and Figure 5.10 (f)) reveals the expected white-line doublet, whose edge onset is a known indicator of a change in valence state. [166] Moving from the surface to the interface, we observe a pronounced 1 eV shift of the L_3 edge to lower energy loss in both samples. This trend indicates clear reduction to a Fe^{2+}-like valence, in agreement the n-type Mott-Schottky behavior observed here for 2 nm LFO in addition to previous theoretical and experimental results that indicate the LFO conduction band is nearly degenerate with that of n-STO such that electrons will accumulate at the interface to reduce the Fe ions. [160,165,167]

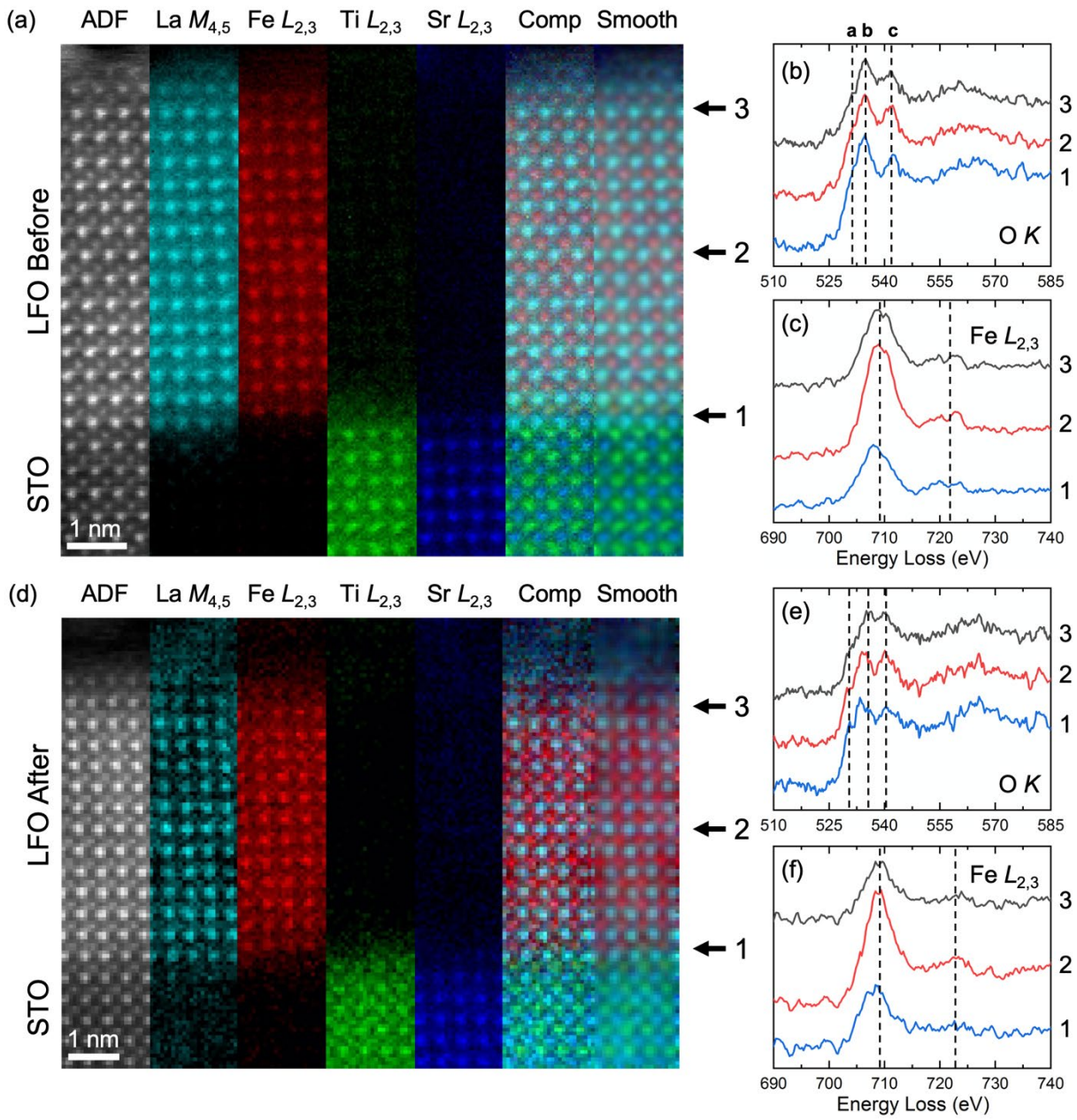

Figure 5.10: Cross-sectional STEM-ADF image, STEM-EELS composition maps, and extracted spectra for the O K and Fe L2,3 edges from the numbered regions for the before (a-c) and after (d-f) conditions. The extracted spectra were acquired from near the marked regions.

Considering all electrochemical and structural characterization presented here, we present an approximate band diagram shown in Figure 5.11 to explain the thickness dependent OER electrocatalysis. Comes and Chambers reported that LFO exhibits almost intrinsic character at the

LFO/n-STO interface [168]. Here, we have used the same procedure for LFO growth as the Comes and Chambers report and thus use their band alignment determination as a basis for our model.

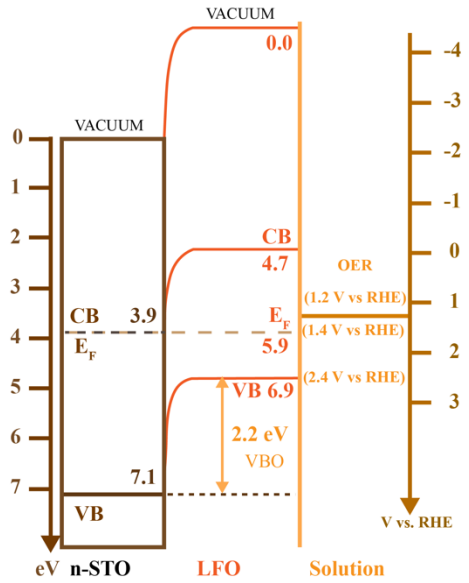

Figure 5.11: Band diagram for n-STO/LFO films immersed in aqueous electrolyte. Bandgaps of 3.2 and 2.2 eV were used for n-STO and LFO, respectively. Conversion from V vs RHE to eV was obtained using the conversion factor 0 V vs RHE = 4.5 eV.

Based on Figure 5.11, the thickness dependence for OER electrocatalysis with LFO can be explained based on the large VBO at the n-STO/LFO interface and the intrinsic nature of LFO. From previous literature, the VBO at the n-STO/LFO interface increases to a steady value of 2.0-2.2 eV within the first ~2.5 nm of deposited LFO. This means that the LFO/electrolyte interface for a 2 nm thick film displays more n-type character and results in poor catalysis. For LFO films >2.5 nm, the surface states which drive catalysis, most likely oxygen defects based on STEM-EELS results, are proximal to the n-STO/LFO interface and thus electrons have a higher probability of being extracted during OER electrocatalysis. Given the intrinsic nature of the LFO material and thus low concentration of free carriers in the valence band, this extraction likely relies on activation of electrons from the valence band to a low density of mid-gap electronic states, often called traps. This model represents a trap-state limited diffusion of charge through the LFO film and has been used to explain charge transport in nanocrystalline wide band gap oxides such as TiO_2 [169–171]. As surface states are moved further from the *n*-STO/LFO interface, the

probability of extraction decreases, resulting in lower observed current. Within our proposed circuit model, the R_{LFO} term represents the activation of electrons from the valence band to mid-gap states. Notably, this term was found to be the limiting factor in determining the overall resistance at the LFO/electrolyte interface. This overall resistance can be taken as $R_{LFO} + R_{SS}$ where at the 2.23 V condition, $R_{LFO} >> R_{SS}$ for all LFO thicknesses. This indicates that overall current is more likely limited by activation and transport of carriers than by catalysis at the oxide surface. Consideration of bulk conductivity is thus a significant factor in the design of effective electrocatalysts, regardless of surface chemical reactivity. Furthermore, these results show that band engineering is critical for multilayer film catalysts. Future designs could be targeted to produce greater bulk conductivities with a surface layer that is band engineered for optimal catalytic performance.

5.1.5.5 Conclusions

In summary, we have examined the role that interfacial band alignment plays on OER electrocatalysis in $LaFeO_3$ using a series of thin films grown on *n*-$SrTiO_3$ by molecular beam epitaxy. We find that ultrathin films (~2 nm) are *n*-type due to the degeneracy of the STO and LFO conduction bands at the interface. As the thickness increases, band bending yields intrinsic or slightly *p*-type LFO with the Fermi level near mid-gap. For reasonably thin films this band alignment produces favorable electrocatalytic performance, but catalysis rapidly degrades with increasing thickness. Electrochemical impedance spectroscopy results indicate that catalysis is mediated through surface defect states with a potential centered at 1.63 V vs RHE (~0.7 V above the valence band edge). Furthermore, catalysis at the surface is found to not be the rate limiting factor toward production of current, but rather current is limited by a Schottky barrier at the n-STO/LFO interface coupled with slow electron transport in the bulk of the LFO film.

5.2 Lanthanum Nickelate ($LaNiO_3$)

5.2.1 Structural and Magnetic Properties

Lanthanum nickelate has a rhombohedral perovskite structure with space group $R\bar{3}c$ at room temperature. Experimental lattice parameters of LNO are a=b=5.4573Å and c=13.1462Å [172]. The LNO unit cell is shown in Figure 5.12. A-site is occupied by La^{3+} and B-site Ni^{3+} are octahedrally coordinated with oxygen. The NiO_6 octahedra is tilted with respect to its corresponding pesudocubic structure and distortion due to octahedra tilting leads to rhombohedral structure in ambient condition.

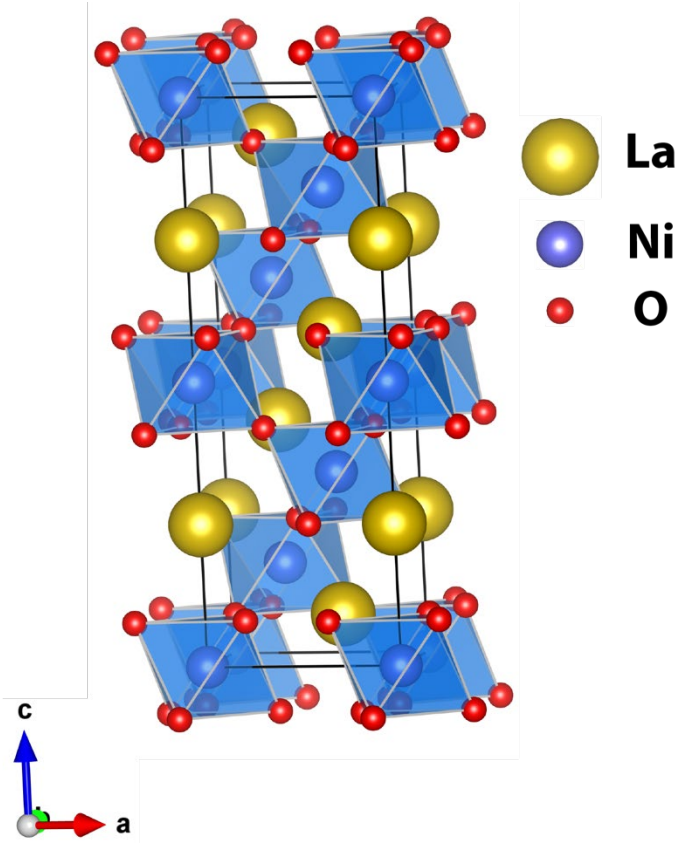

Figure 5.12 : Rhombohedral perovskite $LaNiO_3$ unit cell.

The Ni-O-Ni bond angle in pseudocubic structure is 180°, due to octahedra tilting, out-of-plane Ni-O-Ni bond angle is approximately 165° in rhombohedral structure [173]. The glazer notation for NiO_6 octahedra tilting is $a^- a^- a^-$. LNO is only member of nickelates with rhombohedral structure. Given the La-O and Ni-O bond lengths the tolerance factor of LNO (0.985) is close to unity. Therefore, it is stable in rhombohedral structure, rest of the nickelates are orthorhombic [173].

Ni ion is in 3+ valence state has an electron configuration $3d^7(t_{2g}^6 e_g^1)$ in low spin state and doesn't show Jahn-Teller distortion in ground state. This low spin configuration causes strong Ni-O-Ni overlapping resulting in paramagnetic behavior [172]. Our DFT calculation also reveals that the structure with paramagnetic phase is the most stable one. LNO thin films have been reported to have antiferromagnetic order [174] but the bulk LNO is paramagnetic at all temperature.

5.2.2 Bulk and Surface Electronic Properties

LaNiO3 is metallic at room temperature. There are reports of metal-to-insulator transitions in LaNiO3 thin films but the bulk LaNiO3 is metallic down to 1.5k and is the only member of nickelate family that doesn't undergo metal-to-insulator phase transition [172]. Ni 3d bands due to the crystal field of octahedrally coordinated oxygen splits in 3-fold degenerate t_{2g} and 2-fold degenerate e_g states.

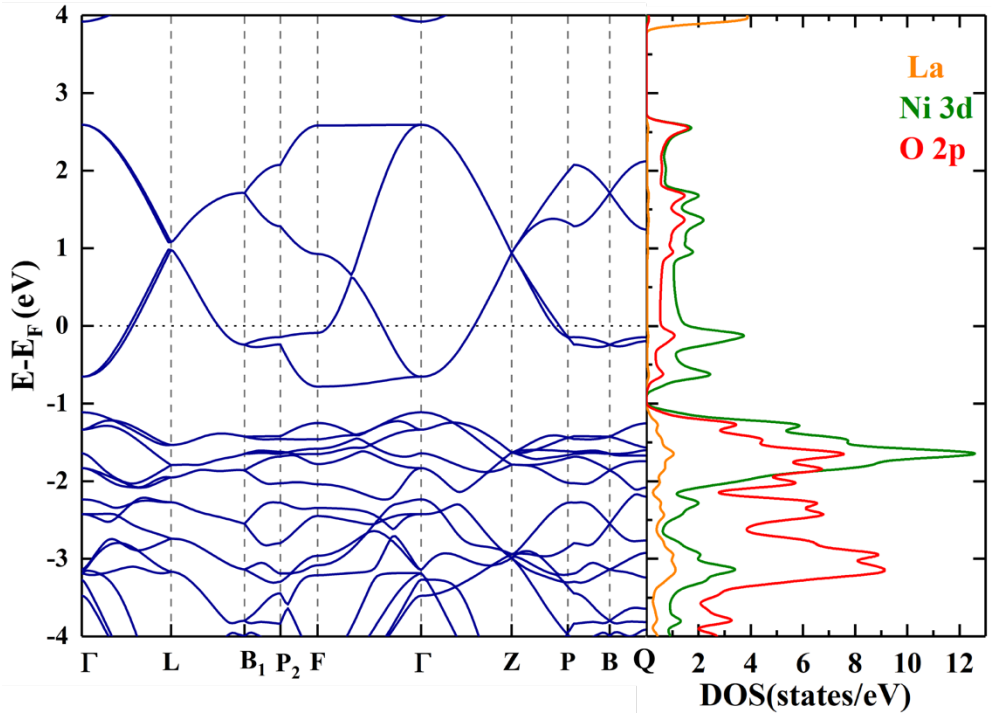

Figure 5.13 : Electronic band structure and projected density of states of rhombohedral $LaNiO_3$ structure.

Our DFT calculations shows that $LaNiO_3$ metallic as observed in the Figure 5.13. The conduction band near the Fermi energy are formed of hybridized Ni 3d and O 2p orbitals. Strong correlation of Ni 3d electrons and hybridization of Ni 3d-O 2p orbital impacts it's electronic properties significantly [175]. And unoccupied O 2p and Ni 3d e_g state form the valence band near the Fermi energy, which is consistent with available literature [176,177]. In the epitaxial thin films, strain lifts the degeneracy of e_g orbitals. The way available one electron fills the e_g states leads to exotic properties in $LaNiO_3$ thin films [11,146,152].

5.2.3 Thin Film Synthesis

$LaNiO_3$ thin films are synthesized using MBE. We used two different substrates $LaAlO_3$ (100) and Nb:$SrTiO_3$ (001). LNO (a_{pc}=3.838Å) have better lattice match with LAO (a_{pc}=3.795Å) than

STO(a_{pc}=3.905Å) so defect free peseudomorphic growth is more favored on LAO. But experimental design for cyclic voltammetry and electrochemical impedance spectroscopy in our lab requires conductive substrate, therefore all the characterization presented here are for LNO thin films grown on 0.7% Nb doped STO substrates. La (ESPI, 99.9%) and Ni flux were supplied through individual high temperature effusion cells. The cell temperatures for La and Fe were approximately 1550 °C and 1350 °C respectively. The oxygen flow was set to 2.5 sccm (Airgas, 99.999%) during the entire growth and an RF plasma source operated at 300 W was used to supply atomic oxygen. Pressure in the chamber during growth was $5x10^{-5}$ Torr. The *n*-STO substrate was heated to 600 °C in oxygen plasma before growth to remove hydrocarbons and recover a well-defined surface as observed by RHEED.

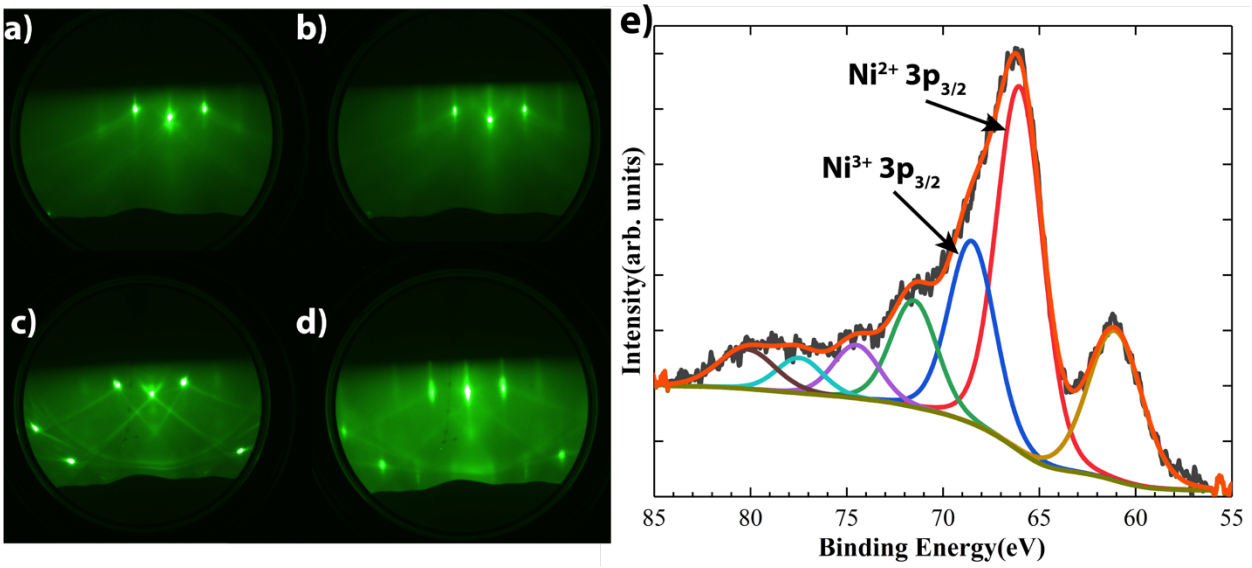

Figure 5.14 : RHEED images taken along (110) for a) Nb:STO (001) substrate, b) 3 nm thick LNO thin film on Nb:STO (001), c) LAO (100) substrate d)6nm thick LNO thin film on LAO(100) substrate e) Ni 3p XPS region for 3 nm LNO-NbSTO sample.

A shuttered growth process was employed to synthesize the samples at the same temperature (600 °C). The RHEED image of LNO thin film on STO and LAO is shown in Figure 5.14. LNO thin

films on STO and LAO substrate are coherently strained and crystalizes in pseudocubic structure. Due to the rhombohedral structure of LNO $(01\bar{1})$ plane is parallel to the (001) plane of STO, which allows LNO to grow in pseudocubic structure. Sharp RHEED image indicates the high crystallinity single crystal film. Ni is more stable in Ni^{2+} state than Ni^{3+}. Therefore, it is very sensitive to growth temperature and oxygen pressure, which makes it more challenging to grow stoichiometric LNO.

XPS analysis of the LNO thin films shows the Ni^{2+} and Ni^{3+} mixed valence state. Despite the mixed valence state LNO thin film shows high crystallinity and smooth surface as characterized by sharp RHEED pattern as shown in Figure 5.14.

5.2.4 LNO as an OER Catalyst

OER activity of the catalyst depends on several factors. In the case of 3d TMOs most significant is d-orbital filling, more specifically e_g filling. It has been reported that e_g close to unity (~1.1) maximizes the OER performance [8]. Number of e_g electrons in LNO (e_g=1) puts it in a spot with highest catalytic activity among 3d TMOs. LNO shows strong hybridization of Ni 3d and O 2p orbitals which is another characteristic required for higher catalytic activity. Thin films are often strained due to lattice mismatch with the substrate. Strain in LNO lifts the degeneracy in e_g states. Available one electron either fills d_{z^2} or $d_{x^2-y^2}$ orbital. It has been found that compressive strain favors filling of out of plane d_{z^2} orbital which lowers d-band center thereby lowering the charge transfer gap between 3d and 2p orbitals [11,34]. Also, LNO can be doped, or electrons can be transferred to 3d orbital by creating heterostructures to achieve optimal OER performance [13,84]. Therefore, the room for tuning catalytic performance of LNO, which already is the best OER catalyst in its intrinsic form, makes it the best candidate for OER catalyst.

CV measurement was performed on $LaNiO_3$ thin film and is shown in Figure 5.15. Catalytic current density of 13μA/cm^2 (η_{OER} = 0.37 V) was measured for 3nm LNO film. Which is better than the LFO thin films of comparable thicknesses. Further investigation is needed to explore if there exist thickness dependance of OER catalysis as we discovered in the LFO thin films in our previous work [51].

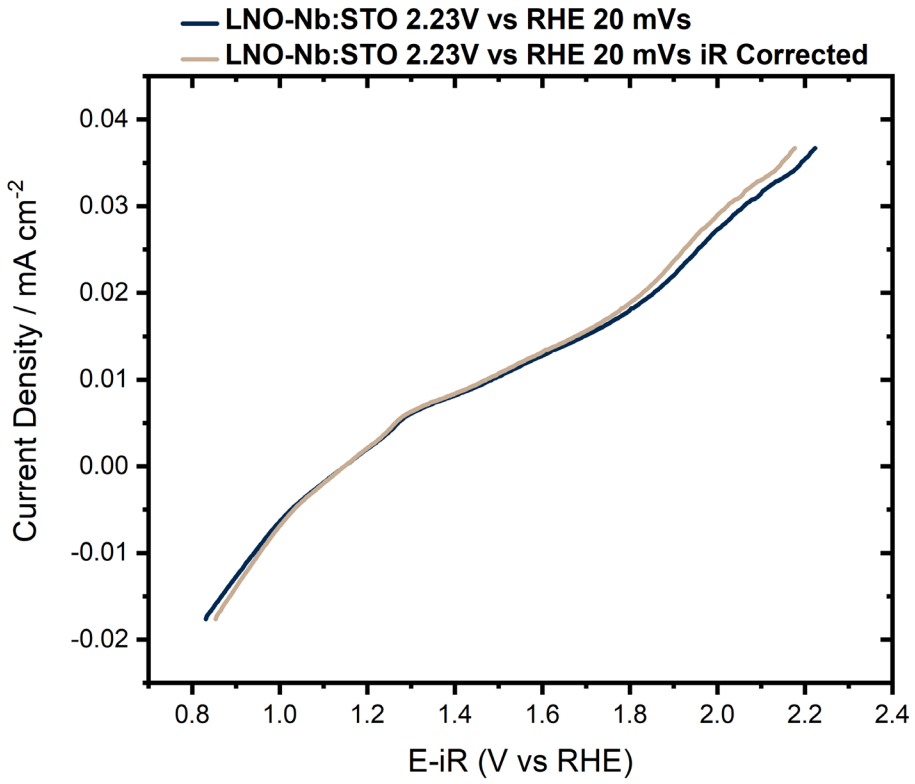

Figure 5.15: CV measurement of 2nm LNO-NbSTO thin film.

Chapter 6

Enhanced OER Activity in Strontium Doped LaFeO3 Thin films

6.1 First Principles Calculation

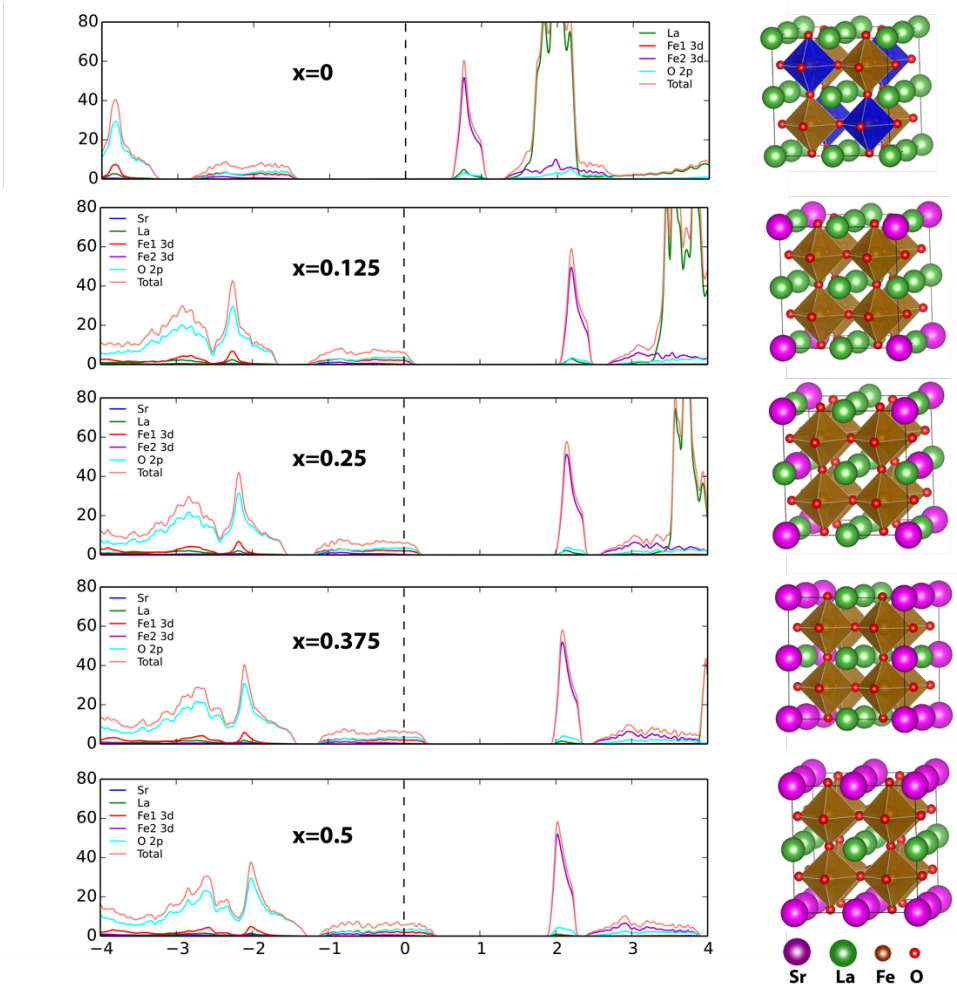

Figure 6.1: Density of states for different level of Sr doping in LFO due to majority spin. Corresponding crystal structures on the right, used for DFT simulations. Structures are exported from VESTA [36].

First principles calculations were performed on LFO for different level of doping. 2×2×2 superlattice of pseudocubic structure was used for the electronic structure calculations. The in-plane lattice parameter was constrained to match that of cubic STO and only out-of-plane lattice parameter was allowed to relax for structure optimization calculation. Atomic positions and lattice

parameter from structure optimization was then used for electronic structure calculation. Different level of Sr doped structure used for calculation is shown in Figure 6.1. Sr atom can occupy any La lattice site. And there are La lattice site with different symmetry (face, corner and center). Therefore, to check the effect of Sr atoms in a lattice site different symmetry, we performed the electronic structure calculation using different symmetry of Sr atoms. Our calculations reveal that different symmetry does not change the valence band conduction band in a region of ~1eV around the Fermi level as shown in Figure S5.

Addition of Sr^{2+} in A-site introduces holes into the lattice. From DOS of the bulk LFO, valence band maximum consists of strongly hybridized Fe 3d majority spin states and O 2p states and the composition doesn't change significantly over a range of Sr doping level (x=0.125, 0.25, 0.375 and 0.5). PBE+U calculations indicate that Sr^{2+} introduced holes have mixed Fe 3d-O 2p character. As reported by Ritzmann *et.al* these holes lie just above the Fermi energy and oxygen vacancy formation is more favored in presence of Sr^{2+}. Therefore holes have mostly O 2p character and are delocalized over oxygen sublattice [178].

Table 6.1: Out of lattice parameter for different concentration of Sr2+ in 2×2×2 Sr doped LFO superlattice.

X	**a=b(Å)**	**c(Å)**
0	7.809	7.877
0.125	7.809	7.855
0.25	7.809	7.809
0.375	7.809	7.774
0.5	7.809	7.732

Another interesting trend was observed for lattice parameter. The cell volume (out-of-plane lattice parameter) decreases with increased Sr^{2+} concentration even though the Sr^{2+} have higher ionic radii than La^{3+}. The out of plane lattice parameter are shown in table 6.1.

As reported in several studies the decreased unit cell volume is indicative of increased Fe^{4+} concentration and structure of the unit cell is dominated by smaller ionic radii of Fe^{4+} rather than Sr^{2+} [179–183]. However, Ritzmann *et al.* found that the introduction of a hole in the oxygen lattice results in a decrease in the magnetic moment of Fe, which shortens the Fe-O bond length and lowers the unit cell volume [178]. Our DFT+U modelling agrees more with this model to explain the decrease in unit cell volume with increased Sr^{2+} concentration.

6.2 Thin Film Synthesis

Sr-doped LFO (LSFO) thin films were synthesized using MBE. Commercially available 0.7% Nb doped STO was used as a substrate. The atomic fluxes were obtained by heating source material in the effusion cell. The effusion cell temperature for La, Fe and Sr were approximately 1550°C, 1350°C and 460°C respectively. Prior to growth, the substrate was heated in oxygen plasma to 700°C to remove any hydrocarbons or water molecules and to achieve a clean surface. Thin film samples were synthesized with substrate at 700°C. Thin films were deposited in layer-by-layer fashion and each atomic layer was doped to achieve uniform doping throughout the thin film sample. The shuttered growth technique was used to deposit La, Sr and Fe sequentially. The atomic flux and shuttering time were calibrated in such a way, that one shuttering cycle deposits one unit cell, which allows precise control over thickness of the film. Sr flux was calibrated to produce the same thickness as La in the same amount of time. This allows us to control the level of doping by simply adjusting the shuttering time between La and Sr.

The growth process was monitored using RHEED. RHEED images of the 15% and 20% Sr doped sample is shown in Figure 6.2. Clear oscillations were observed in RHEED intensity, which was used to control the thickness. Thicknesses were later confirmed by XRR measurements. XRR data used to determine the thickness of the 15% LSFO is shown in Figure 6.6. The sharp RHHED pattern and oscillation in the intensity confirms layer-by-layer growth and high crystallinity of the thin film sample.

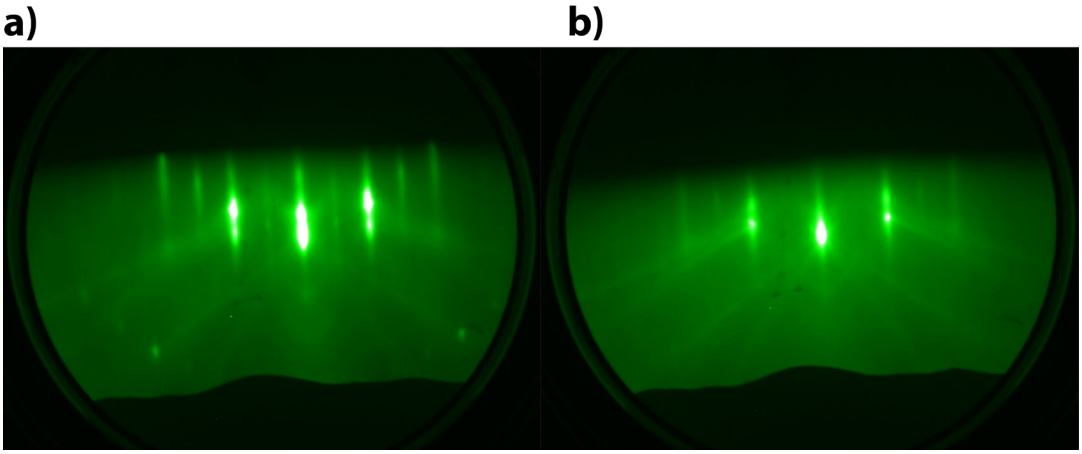

Figure 6.2: RHEED images of LSFO thin films with a) 15% doping in A-site b) 20% doping in B-site.

6.3 XPS and XRD Analysis

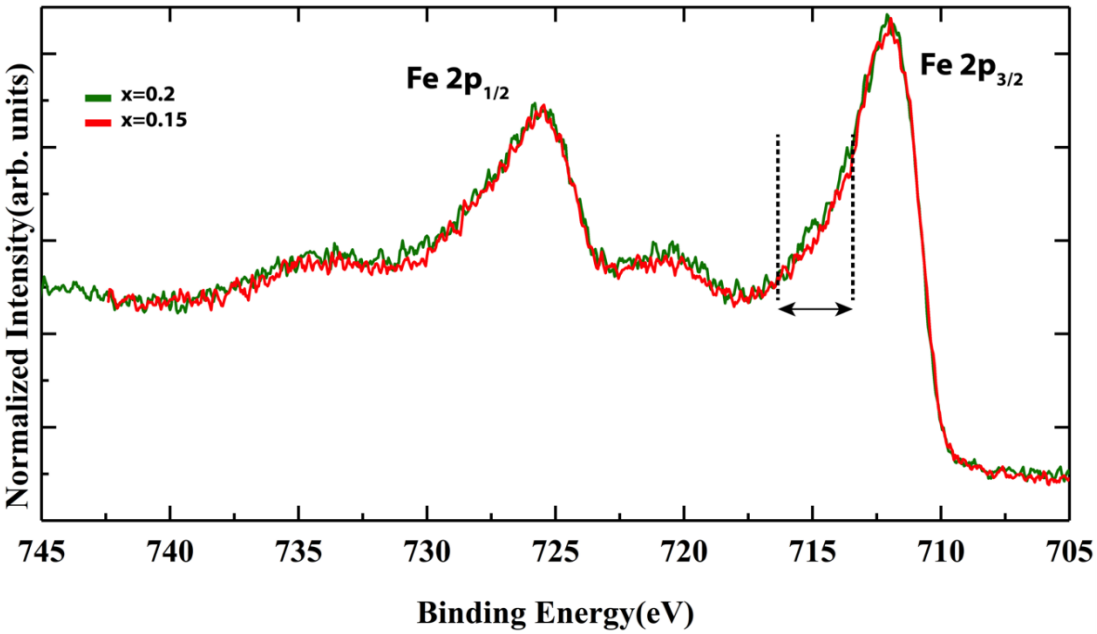

Figure 6.3: Fe 2p XPS region for LSFO thin films. The peak line shape doesn't change significantly to infer change in Fe^{4+} concentration in two different level of Sr^{2+} substitution.

XPS measurements were performed in-situ using Al Kα line. Analysis of XPS data was performed taking O1s peak as a reference BE and was set to 530eV.XPS region for Fe 2p shows two distinct peaks due to spin orbit splitting. Both $2p_{1/2}$ and $2p_{3/2}$ have a satellite peak and are approximately 8 eV apart from the main peak. These satellites are the confirmation of Fe^{3+} stoichiometry [139,184]. Strontium doping in A-site introduces holes into the lattice. Hole introduced due to substitution of Sr^{2+} on A-site can transfer electron either from Fe or O lattice site, which will either oxidize Fe^{3+} to Fe^{4+} or create a ligand hole on oxygen as in an O^{1-} . Fe 2p peak is complicated and requires very careful analysis as it contains contribution from spin multiplets, satellites and different Fe valences, if they are present. The region marked with dotted line and arrow in the Figure 6.3 is the BE range for Fe^{4+}. We did not observe any significant change

in peak shape between 15% and 20% doped LSFO compared to undoped LFO. Even though results from first principles calculation point towards the possibility of formation of Fe^{4+}, it is not evident from XPS data. Therefore, XPS and PBE+U results collectively suggest that Sr doping mostly results in formation of oxygen holes and not an Fe^{4+} formal charge. This is consistent with the reports of Abbate *et al.,* where they found that for lower concentration of Sr2+ (x≤0.5) holes have mostly O 2p character and for higher concentration of Sr^{2+} (x>0.5) holes have Fe3d-O2p mixed character [185].

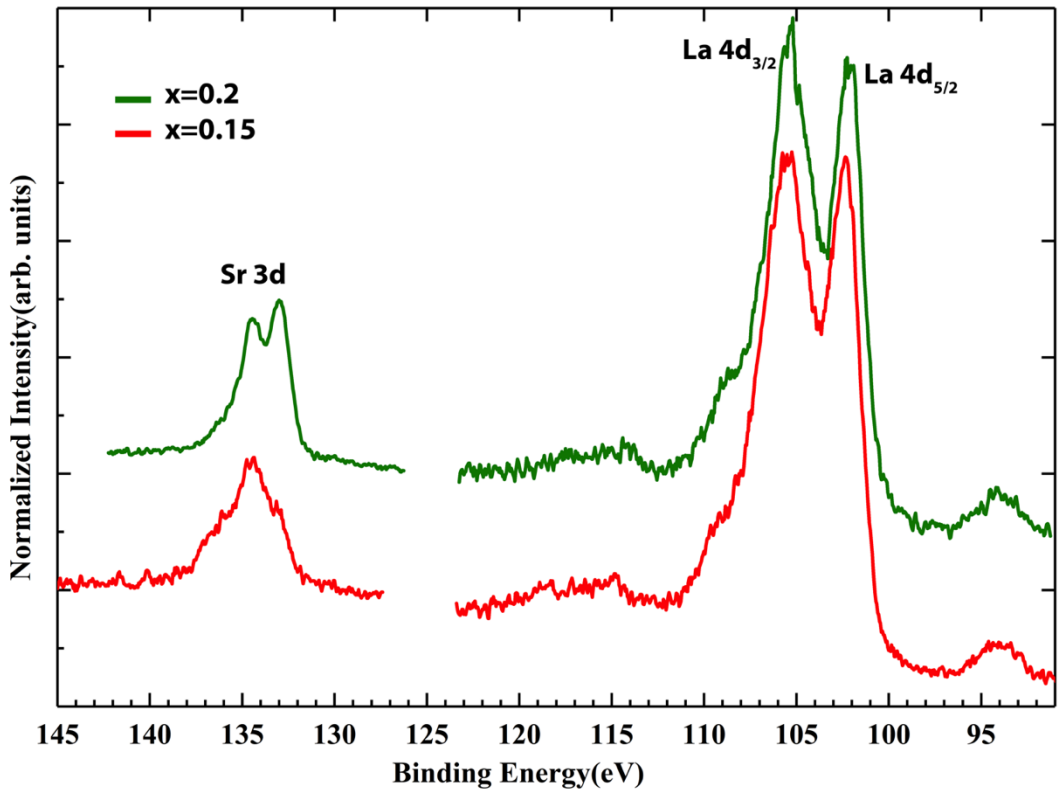

Figure 6.4: La 4d and Sr 3d XPS regions of LSFO thin films.

The Sr 3d and La 4d XPS region are shown in Figure 6.4. La 4d peak shows spin-orbit splitting with two peaks approximately 5eV apart. Sr 3d peak also exhibits spin-orbit splitting and it is well

resolved for x=0.2, which confirms the higher concentration of Sr in the sample, which results in higher peak intensity.

High resolution XRD measurements were performed on these samples and are shown in Figure 6.5. The out of plane HRXRD data shows the two intense reflection peaks from STO (001) and (002) crystal planes. The LFO peaks are on the left shoulder of main reflection peak from substrate shows that the thin film is coherently strained to lattice match with the substrate.

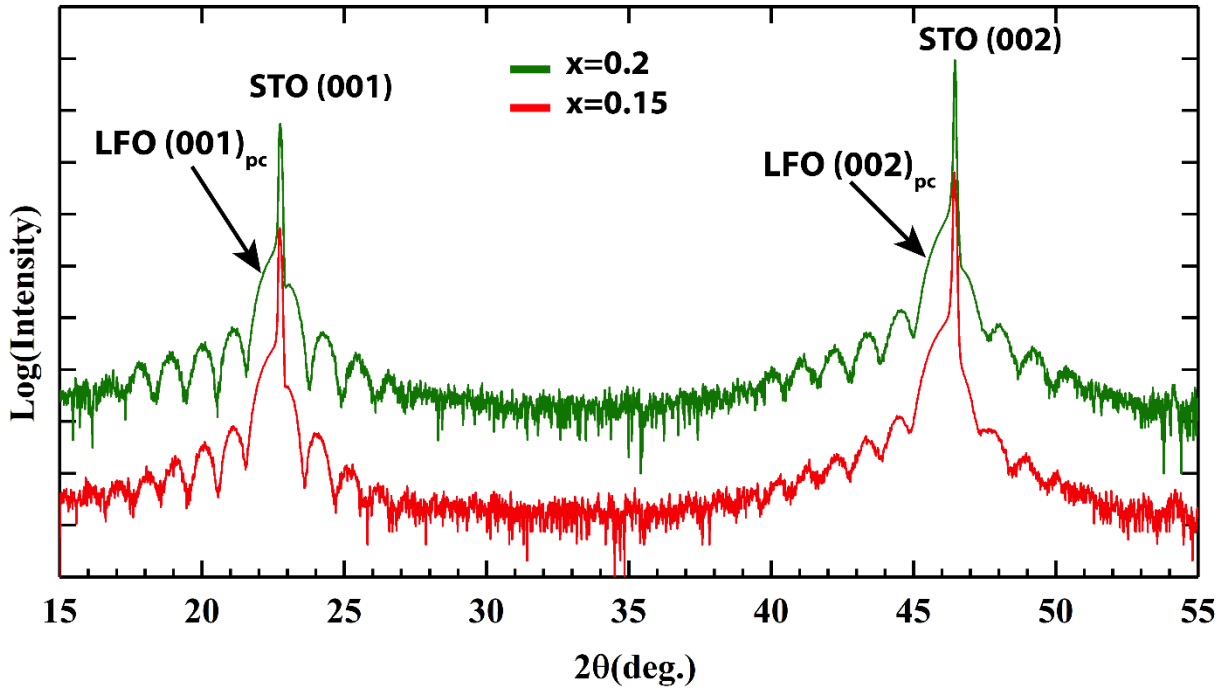

Figure 6.5: HRXRD out-of-plane 2θ-ω scans for (001) and 002) peaks of LSFO/Nb:STO thin films

The Kiessig fringes originated from the specular reflection from the LSFO film and Nb:STO interface indicates high crystallinity of the film and well defined interface with the substrate. If examined carefully, the reflection peaks for LSFO film are slightly shifted to the right for higher Sr^{2+} concentration. This indicates the smaller lattice parameter for higher Sr^{2+} concentration, which agrees with our DFT+U results.

The surface roughness and thickness of the LSFO thin films were determined by fitting X-ray reflectivity data as shown in Figure 6.6. The thickness of both the films estimated to be ~9 nm and the surface roughness under a unit cell.

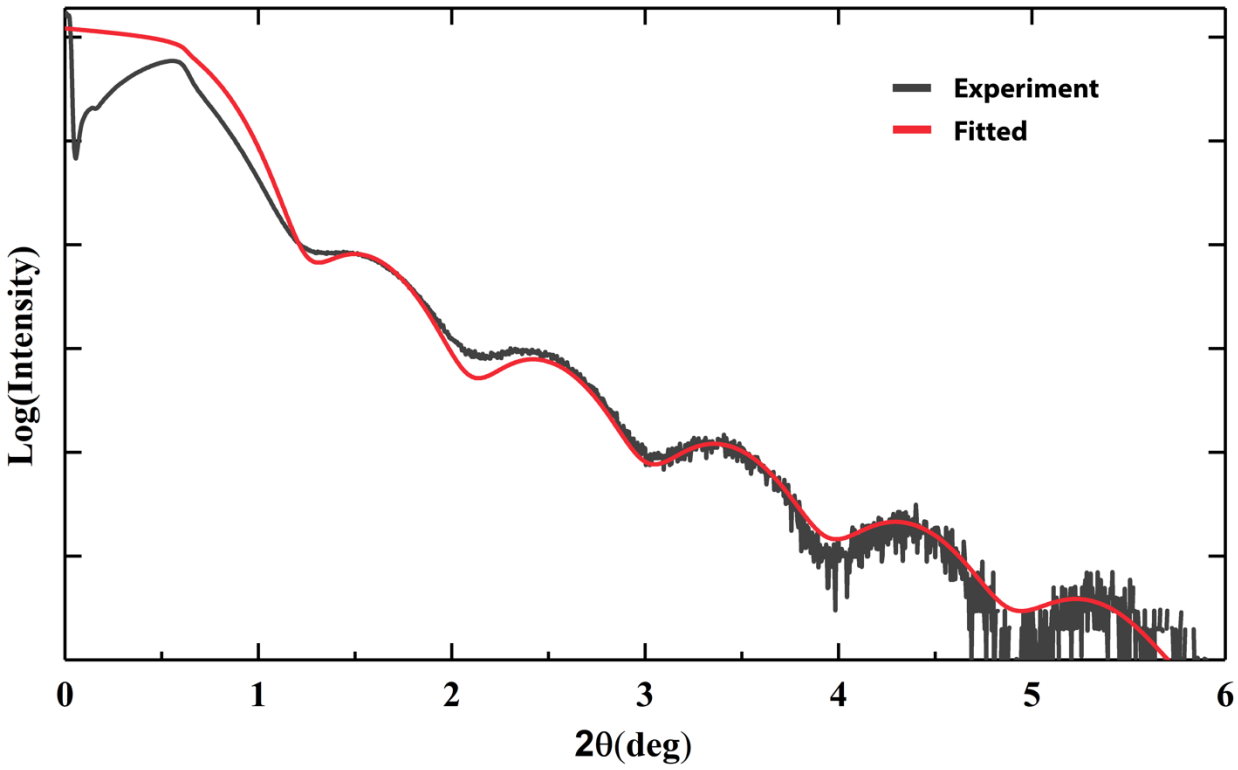

Figure 6.6: XRR data and its fitting to obtain the thickness.

6.4 OER Catalysis

LSFO thin films samples were prepared as an electrode with the procedure mentioned in section 3.5. And anodic current was measured for applied potential. A CV plot is shown in the Figure 6.7 and the OER performance of LFO thin films of varying thicknesses is shown for reference. Both LSFO thin films exhibit higher OER current compared to LFO thin film with similar thickness. Increase in the Sr^{2+} concentration decreases the overpotential and significantly improves the OER

current. For x=0.15, 23μAcm^{-2} was measured for 1.6 V vs. RHE (η=0.37). Similarly, 193μAcm^{-2} was measured for 1.6 V vs. RHE (η=0.37) for x=0.2. Compared to LFO thin films this is significant improvement in catalytic current.

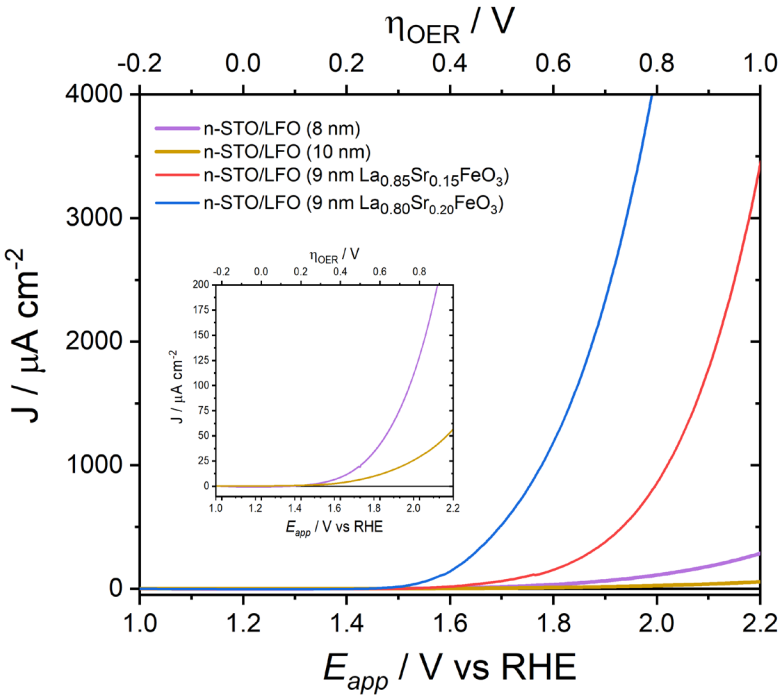

Figure 6.7: CV measurement on LSFO and 6nm LFO thin film samples.

6.5 Discussion and Conclusion

OER performance has been widely observed to improve due to hole doping, but the mechanisms enhancing electrochemical activity are not unique. The DFT+U modelling of LSFO samples and analysis of XPS and XRD data suggests that holes are delocalized in the oxygen lattice rather than formation of Fe^{4+} states. This is consistent with the reports that delocalization of holes in the oxygen lattice dominates for small concentration of Sr^{2+} (x< 0.5) and increasing occupation of Fe lattice site for higher concentration of Sr^{2+} [185,186]. More data with higher Sr^{2+} concentration is

necessary to get a broader picture of the evolution of OER activity. Delocalization of holes at oxygen lattice results in increased Fe-O covalency and easier hole transport [178]. Migration of these holes through oxygen sublattice causes electron migration through Fe sublattice. Furthermore, formation of O 2p holes decreases the charge transfer energy by shifting the Fermi level closer to the valence band, making it easier for carrier to transfer between Fe 3d and O2p bands and the electrolyte for catalysis [73]. Both the oxygen holes and formation of Fe^{4+} contribute to the enhancement of electrocatalysis of LSFO thin films.

Chapter 7

Band-Engineered LaFeO3-LaNiO3 Thin Film Interfaces for Electrocatalysis of Water

Chapter taken from Paudel et al. Submitted for publication, available online via https://arxiv.org/abs/2207.07264

7.1 Introduction

Interfaces in complex oxide thin film heterostructures are particularly interesting because of their non-equilibrium electronic properties, which usually do not exist in the bulk or even in uniform films. These unique properties emerge as a result of interfacial interactions, such as an offset in the band alignment for occupied states accompanied by charge transfer across the interface [57,58,154,187–195]. The band gap of the materials [196], separation between O 2p and metal 3d states [85], and film thickness [197] all play a significant role in charge transfer at the interfaces and band alignment at the surface. Careful epitaxial growth by molecular beam epitaxy or pulsed laser deposition enables control of these parameters individually and offers a route to the rational development of new functional materials for applications in renewable energy systems.

Transition metal (TM) oxide thin films, heterostructures, and interfaces have emerged as ideal model systems for understanding catalysis in energy conversion devices (electrochemical cells) by splitting of water for oxygen evolution reaction (OER) and oxygen reduction reaction (ORR) [6,198,199]. The available descriptors for high OER activity are based on the number of TM 3d (e_g) electrons [8], extent of O 2p-TM 3d hybridization and covalency of TM-O bond, valence state of TM [12]. and oxygen binding energy at the surface [200,201]. These parameters can be precisely tuned by doping on the perovskite A and B sites and creating interfaces and

heterostructures [13,182,199,202–204]. Collectively, these effects control the alignment of TM 3d electronic states relative to both the Fermi level and the OER reaction potential energy, which can reduce overpotentials for electrocatalysis.

Among these oxides, $LaNiO_3$ (LNO) and other perovskite nickelates have been reported to exhibit excellent catalytic performance for OER [199,205]. Bak et al. have shown that perturbing NiO_6 octahedra by electrochemical exchange of Fe on the LNO surface facilitates charge transfer and improves OER activity [206]. Similar results have been demonstrated by doping Fe on the B-site to generate partial electron transfer from Fe to Ni, leading to an $Fe^{3+\delta}$ and $Ni^{3-\delta}$ formal charge [13]. These alloy $La(Fe,Ni)O_3$ materials exhibited greater electrocatalytic performance than either pure $LaFeO_3$ (LFO) or LNO [13]. Partial oxidation of Fe^{3+} results in stronger hybridization between O 2p and Fe 3d orbitals, which increases OER activity of the perovskites owing to Fe higher covalency [8,12]. By forming an interface of LNO with a suitable material that induces charge transfer it may be possible to produce the same effect as extrinsic doping without any disorder introduced by impurity atoms, which might further improve the OER activity of LNO. Collectively, these results point to the importance of band engineering in heterostructures to boost OER activity. $LaFeO_3$ (LFO) is itself a good candidate for OER catalysis, particularly when hole doped [197,207], and given its electronic structure, LFO/LNO heterostructures might push boundaries in OER performance through interfacial hole doping of LFO. However, the LFO/LNO interface is noticeably lacking in exploration, both experimentally and theoretically.

In this work we characterize the enhanced catalytic performance of heterostructures formed with LNO/LFO grown using molecular beam epitaxy (MBE). The band alignment at LFO/LNO interface from first principles calculations using density functional theory (DFT). Taking the

Zhong and Hansmann model for band alignment via continuity of the O 2p bands across an interface as a basis [85], we discuss the alignment of oxygen center of mass for 2p states and possible charge transfer. We also present experimental band alignment of epitaxial LFO/LNO heterostructures using X-ray photoelectron spectroscopy (XPS). Using these band-engineered heterostructures, we demonstrate how band alignment can be used to dramatically enhance the catalytic performance of the LFO thin films by shifting the material from an intrinsic semiconductor with the Fermi level mid-gap to a *p*-type material with the Fermi level near the valence band band maximum. These LFO/LNO heterostructures show an increase in OER catalytic reaction rate by two orders of magnitude via cyclic voltammetry measurements compared to LFO films grown directly on *n*-doped $SrTiO_3$ [197].

7.2 Methods

7.2.1 DFT Calculations

Computational descriptions of these heterostructures were carried out on a $LaFeO_3/LaNiO_3$ superlattice comprised of 4 layers of each material with a $\sqrt{2}\times\sqrt{2}$ in-plane configuration assuming periodic boundary conditions in all directions. G-type antiferromagnetic polarization for LFO [208] and no spin polarization in LNO were used to replicate the magnetic behavior of each material at room temperature [172]. In-plane lattice constants were constrained to match the lattice parameter of LFO, and equilibrium lattice parameters along out-of-plane directions and atomic coordinates were obtained by relaxation of the superlattice. Projector augmented wave (PAW) [209] pseudopotentials were used for the description of the atomic cores along with the generalized gradient approximation (GGA) of Perdew-Burke-Ernzerhorf (PBE) [89] for the exchange-correlation functional. Calculations also included corrections based on the Hubbard model [44] to improve the ground state description and correct the band gap of these highly

correlated electron systems [88]. The Hubbard U parameters for Fe (U_{Fe} = 2.84 eV), Ni (U_{Ni} = 3.05 eV), and O (U_O = 6.34 eV) reproduced the experimental band gap in the bulk LFO and LNO as previously reported in the literature [88] and were employed for heterostructure calculations. Energy cut-offs were set to 80 and 600 Ry for wave functions and charge density, respectively. The energy convergence threshold was set to 10^{-6} eV and integration over the superlattice Brillouin zone was performed using an 8×8×1 Monkhorst-Pack *k*-grid [210]. Our first principles calculations were performed using Quantum Espresso (QE) [90].

7.2.2 Synthesis and Characterization

We synthesized epitaxial thin film heterostructures using oxide molecular beam epitaxy (MBE, Mantis Deposition). All samples were grown on 10 mm square 0.7% Nb-doped $SrTiO_3$ (STO) substrates (MTI Crystal) that served as a conductive bottom electrode for XPS and catalysis experiments. STO has a cubic lattice parameter of 3.905 Å while pseudocubic lattice parameters of LFO and LNO, obtained from experimental data are 3.93 Å [211] and 3.83 Å [172], respectively. This small lattice mismatch enables coherent growth of strained thin films. Before loading the substrate into the growth chamber, substrates were cleaned by sonication in acetone and iso-propyl alcohol and then dried with molecular nitrogen.

For LNO growth, the Nb:STO substrates were heated to 600 °C in oxygen plasma generated by a 300 W-RF plasma source (Mantis Deposition) and kept at the same temperature until completion of the LNO layer. Immediately after completion of the LNO layer, the substrate was heated to 750 °C for the LFO growth. Metallic fluxes were obtained by heating elemental sources in effusion cells to the evaporation or sublimation point. Elemental fluxes were calibrated using a quartz

crystal microbalance (QCM). By controlling the individual shutters, LaO and NiO_2/FeO_2 layers were deposited alternately, as described previously [197,212]. The real-time growth was monitored using reflection high energy electron diffraction (RHEED) from the film surface. RHEED exhibited well-defined oscillations in the intensity during the entire growth, confirming the layer-by-layer growth. The oxygen pressure in the chamber during LNO growth was $\sim 5\times10^{-5}$ Torr with the plasma activated to maximize oxidation of the LNO film. LFO was grown at $\sim 6\times10^{-6}$ Torr in plasma as well. After growth, the samples were cooled in oxygen plasma to room temperature.

Chemical composition and electronic valence state of synthesized samples were established using an appended XPS system (PHI 5400, refurbished by RBD Instruments) furnished with a monochromatic Al Kα X-ray source. The absolute core level positions cannot be referenced to the Fermi level of the system owing to a electron flood gun used to mitigate charging. Thus, XPS analysis was performed by aligning O 1s peak to 530eV to provide a consistent reference for all spectra. Band alignment measurements were performed via the Kraut method using the Fe 3p and Ni 3p core level spectra, as described previously [141,154,213,214]. This analysis is not affected by the electron flood gun as it depends on the relative energy separation of the two core level spectra rather than the absolute binding energy as referenced to the Fermi level [214].

7.2.3 OER Electrocatalysis

To fabricate electrodes for catalytic studies, the samples were diced using a standard dicing saw to 5mm×5mm pieces. These *n*-STO/LNO/LFO MBE films were used as electrodes and connected to a glassy carbon electrode (GC, Pine Instruments) as described in our previous work [197]. Gallium indium eutectic (InGa, Ted Pella #**495425**) forged electrical contact between the n-STO

substrate and the GC working electrode. [215] Silver was used to bind the n-STO substrate to the surface of the GC electrode. Chemically inert epoxy (Loctite, EA E-60HP) was then used to cover any exposed silver paint and seal the edges of the n-STO substrate.

Cyclic voltammetry (CV) experiments were performed with a Pine WaveDriver 20 bipotentiostat using a three-electrode setup. The working, reference, and counter electrodes for the electrochemical setup were *n*-STO/LNO/LFO, Hg/HgO (0.1 M KOH, Pine Instruments), and platinum coil respectively. All measurements were carried out under saturated O_2 conditions in water (18 MΩ, Millipore) with 0.1 M KOH electrolyte (pH 12.7) while rotating the working electrode at 2000 rpm to remove bubbles from the electrode surface. All potentials were converted from Hg/HgO to RHE. CV experiments were performed by sweeping the potential at 20 mV s^{-1} from 0.83 to 2.23 V vs RHE for 25 cycles to equilibrate the electrode surface. The anodic trace of the 25th cycle was used for analysis of electrocatalytic performance for OER.

7.3 Results

7.3.1 DFT Analysis

We first employ first principles calculation to establish the band alignment and charge transfer across the LFO/LNO interface and better understand how the heterostructures will function as OER catalysts. Strain and bonding environment may alter the electronic properties significantly between a bulk material and heterostructure, necessitating care to decouple interfacial effects from the structural changes imposed by the superlattice [216]. The interface was modeled employing LFO/LNO superlattice with 4 unit cell thickness for each material, as depicted in Figure 7.1(a). The electronic structure of the interface is rationalized by projecting Bloch states onto localized atomic orbitals in different layers of the superlattice. This decomposition shown in Figure 7.1(b)

only contains contributions from Fe, Ni and O orbitals as Bloch states formed with La ones only give small contributions in the vicinity of from Fermi level. The LFO bandgap in the heterostructure is estimated to be ~ 2.2 eV, which is in close agreement with the 2.3 eV experimental band gap reported previously [153,154]. Overall, features of the electronic structure are also similar to those obtained in calculations of bulk LFO and LNO presented in Figure S1 and S2 of the supplemental material. For instance, the bands crossing the Fermi level within the LNO layers are strongly hybridized Ni e_g and O 2p orbital bringing metallic character to the heterostructure. Occupied Fe e_g states form the top of the valence band within the LFO layers and unoccupied t_{2g} states are ~2.2 eV above the LFO valence band maximum, which is consistent with the bulk properties. The LFO valence band maximum is formed of hybridized O 2p and occupied Fe^{3+} e_g states and lies ~0.2 eV below the Fermi level (**Figure S3**).

In general, quantitative prediction of band offsets at complex oxide interfaces using computational methods is challenging due to exhibit electron correlations, various magnetic states and symmetry considerations [217]. Nonetheless, results could be anticipated from the bulk calculations following the approach by Zhong and Hansmann [85] based on the equilibration of oxygen states yielding the energy continuity of O 2p band center across the interface.

In these heterostructures, p-doping of the semiconductor is expected to be emerge as in bulk the O 2p-band center of LNO and LFO reside at approximately 2.20 eV and 2.82 eV below the Fermi level, respectively. Once the interface is formed, O 2p-band centers obtained from orbital projections on different layers tend to align, as shown in Figure 7.1(b) and listed in Table 7.1. For each material we observe small differences in the calculated O 2p band centers likely attributable to local octahedral tilting and spin configuration variations across the interface that break the

symmetry of the structure. The O 2p center difference for the NiO_2 planes in LNO reside nearly 0.15 eV above those of FeO_2 in LFO. Moreover, results from DFT calculations show that the valence band offset (VBO) of ~ 0.2 eV across the LNO layers, resulting in the nondegenerate p-doping of the LNO. From this offset, we estimated a hole density in the LNO to be 6.02×10^{16} cm^{-3} induced from the charge transfer Further analysis for the electronic band structure, we calculated the effective mass of LNO holes of approximately $0.61m_e$ (**Figure S4**). Details can be found in supporting information and hole densities are presented in table S1.

However, a change in the VBO of ±0.1 eV—roughly the experimental uncertainty for XPS measurements—produces a change in hole density of more than one order of magnitude in either direction. Clearly, the hole concentrations on the Fe ions are highly sensitive to the VBO between LFO and LNO.

Thus we conclude that no charge transfer is to be expected in the system but that the valence band maximum of an LFO film grown on top of LNO should be close to the Fermi level and lead to charge transfer of holes in the material, which may enhance catalytic performance compared to intrinsic and *n*-type LFO films when they are grown directly on Nb:STO in our previous work [197].

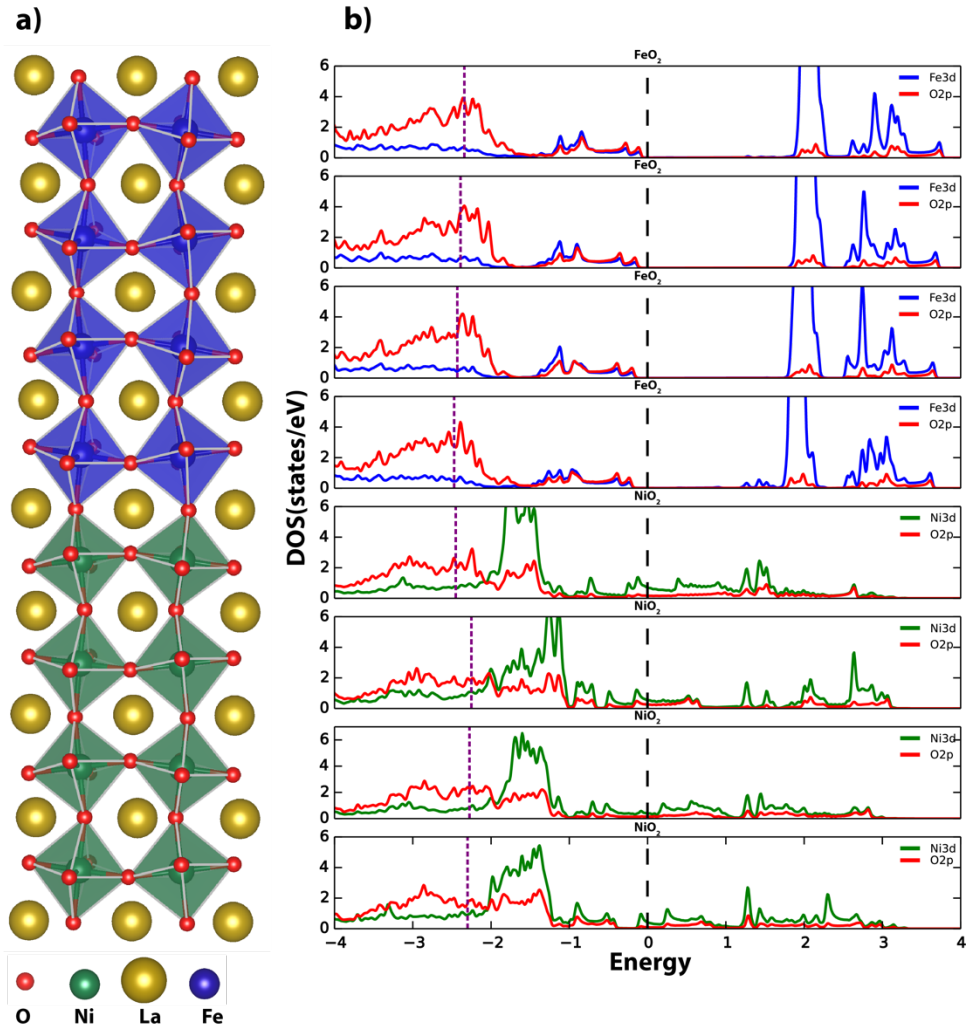

Figure 7.1: a) LFO/LNO superlattice model used for DFT band alignment predictions; b) Orbital projected density of states projected onto different FeO2 and NiO2 layers. Black dashed line is fermi energy and green dashed line represents O 2p center of mass

Table 7.1: Oxygen 2p center in different LaO, FeO2 and NiO2 layers. Layer-1 being closest to the interface. Energy values are in eV.

	$E_p(FeO_2)$	$E_p(LaO)_{LFO}$	$E_p(LaO)_{LNO}$	$E_p(NiO_2)$
Interface 1	-2.47	-2.40	-2.48	-2.45

Internal 1	-2.43	-2.31	-2.27	-2.25
Internal 2	-2.39	-2.29	-2.22	-2.27
Interface 2	-2.34	-2.22	-2.22	-2.30

7.3.2 Experimental Band Alignment Studies

To test the theoretical results determined from DFT, a series of films grown via MBE were measured using *in situ* XPS [141,213]. This method is based on constant binding energy difference between a chosen core level and the valence band maximum (VBM) of a material. Kraut et. al. originally used gaussian broadened theoretical valence band density of states (VBDOS) to fit the experimental valence band data to determine the VBM [140]. In ternary complex oxides, accurate theoretical calculation of VBDOS is complicated and computationally expensive [85]. Chambers et. al used the extrapolation of the linear part of leading valence band edge to zero level background estimate the VBM, offering a rather simple but yet sufficiently accurate estimate [142].

Initial LFO and LNO films were grown separately and used as references for determination of the energy difference between core levels and the valence band maximum in each material. These results are shown in Figure 7.2. The LFO and LNO valence bands extracted from XPS are shown in Figure 7.2(a-b) and determination of VBM by extrapolating the linear region of leading valence band edge is shown in the inset. Linear extrapolation method yields VBM of LFO at -0.2 eV and the VBM value for LNO is -1.1eV. Note that due to the use of the electron flood gun and alignment of the O 1s peak to 530 eV, binding energies are not measured relative to the Fermi level.

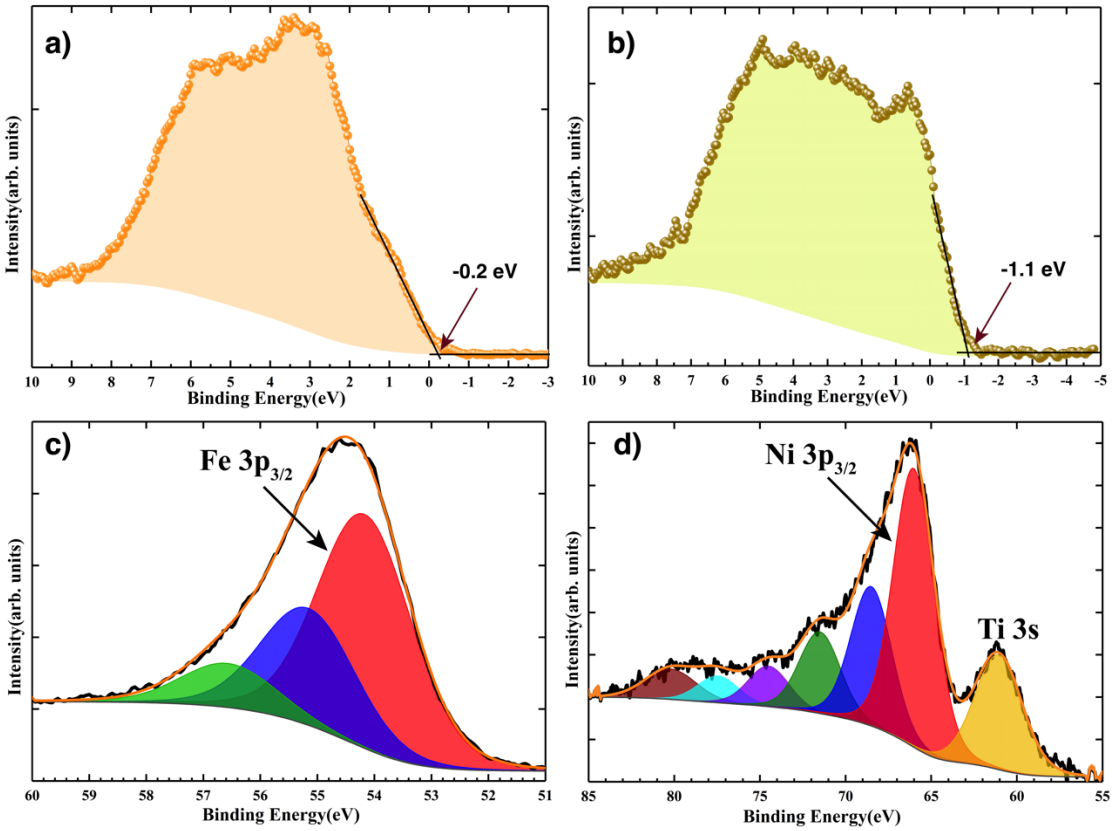

Figure 7.2: Valence band XPS spectra of a) 6nm thick LFO sample b) 3nm LNO sample and fitting of valence band leading edge using linear extrapolation method c) Fe 3p XPS region of LFO sample d) Ni 3p XPS region for LNO sample.

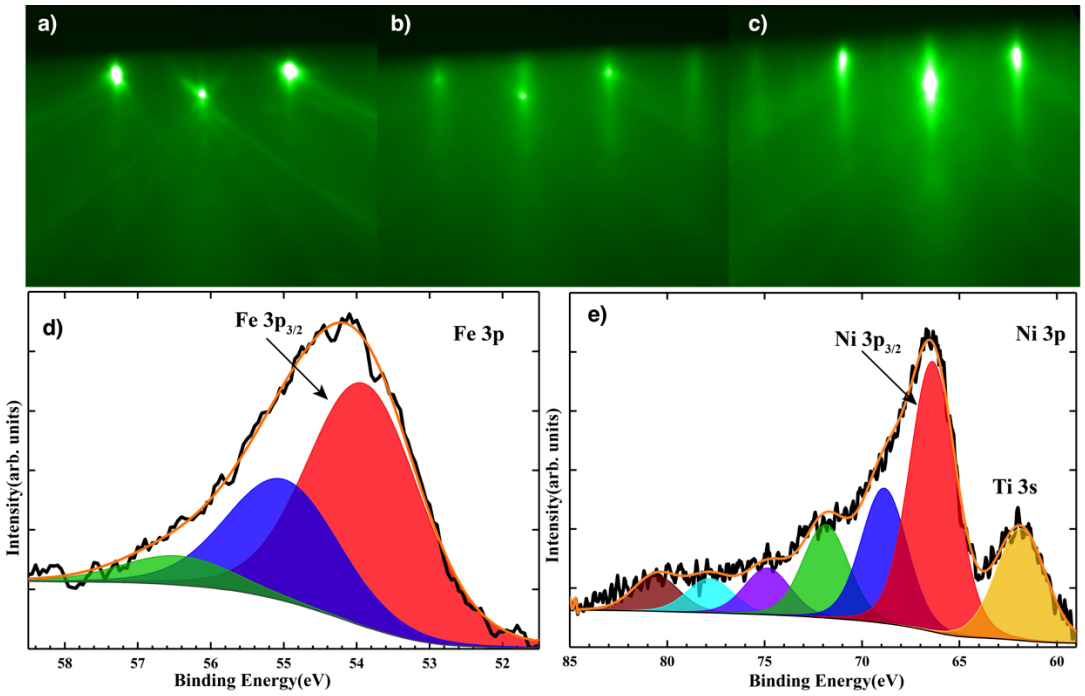

Figure 7.3: RHEED images of a) Nb:STO substrate b) 4 unit cell LNO-NbSTO c) LFO-LNO-NbSTO with 2 unit cell LFO d)Fe 3p XPS region of LFO-LNO sample-1 e) Ni 3p XPS region of LFO-LNO sample-1

The valence band offset is calculated as $\Delta E_V = (E_{CL} - E_V)_{LNO} - (E_{CL} - E_V)_{LFO} - \left(E_{CL}^{Ni\ 3p} - E_{CL}^{Fe\ 3p}\right)_{LFO/LNO}$, where E_{CL} is the chosen core level energy and E_v is the position of valence band maximum. Core level and VBM BE difference is measured in LFO and LNO thin films, and the core levels energy difference is measured in the heterostructure. The individual LFO (~6nm) and LNO (~3nm) thin films used to determine the core level and VBM energy difference for band offset measurement. The Fe 3p and Ni 3p XPS regions are shown in Figures 7.3(c) and 7.3(d). Deconvolution of Fe 3p regions shows that there is an additional satellite peak along with $3p_{1/2}$ and $3p_{3/2}$. Fe $3p_{3/2}$ was chosen as a core level in LFO. Similarly, deconvolution of Ni 3p reveals multiple peaks that must be deconvoluted under a consistent standard for analysis across

samples [218]. The lowest Ni $3p_{3/2}$ feature (shaded region in red) was chosen as the LNO core level for E_{CL}^{LNO}. In order to maintain consistency in the analysis, full width at half maximum, area ratio, energy difference between various valence and spin multiplet peaks were constrained to be the same for all measurements. The core level binding energies, VBM and VBO are presented in the Table 6.2. The VBO for all three heterostructure samples are consistent with value of ~0.3eV, in close agreement with the VBO estimates from first principles calculation considering the experimental error bars.

Table 7.2: Core level, VBM and band offset of LFO, LNO and LFO/LNO samples. The thickness of heterostructure samples: LFO/LNO-1 is 2uc/3uc, LFO/LNO-2 is 4uc/3uc and LFO/LNO-3 is 4uc/4uc. The energy values presented in the table are in eV.

sample	Ni3p3/2	Fe 3p3/2	VBM	ΔE_v
LFO	-	54.17	-0.2	
LNO	66.02	-	-1.1	
LFO/LNO-1	66.37	53.90	-0.65	0.28(0.1)
LFO/LNO-2	66.33	53.91	-0.70	0.32(0.1)
LFO/LNO-3	66.48	54.07	-0.70	0.33(0.1)

7.3.3 Electrocatalysis

Interfacial band engineering with epitaxial films can have a significant impact on emergent optoelectronic properties. To exhibit this impact, we studied the electrocatalysis of the oxygen evolution reaction (OER) using the same epitaxial LFO/LNO thin films described above. Films were converted into electrodes through back contact with a commercial glassy carbon disk and

assembled into a rotating-disk shaft electrode. Figure 7.4 shows the anodic scan for cyclic voltammetry data collected for each film at a scan rate of 20 mV s^{-1} while spinning the disk electrode at 2000 rpm to prevent bubble formation. Each voltammogram was collected following 25 continuous scans over the potential range 0.83 - 2.23 V vs RHE at 20 mV s^{-1}. The catalytic current densities observed at 1.73 V vs RHE (η_{OER} = 500 mV) were found to be 26 µA cm^{-2} for

LFO/LNO-1 and 52 µA cm^{-2} for LFO/LNO-3. The slightly larger current observed for LFO/LNO-3 may be due to the difference in thickness of the LFO layer. By comparison, the much smaller current density 0.2 µA cm^{-2} in a 5 u.c. LFO film (~2 nm) directly deposited on an n-STO substrate (i.e. without an intermediate LNO layer) was recently reported by our groups [197]. This data is reprinted in Figure 7.4 for direct comparison with the present LFO/LNO films.

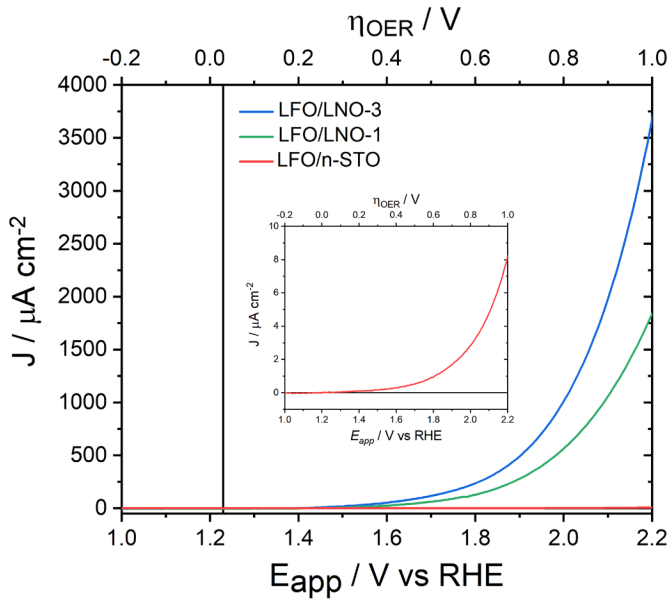

Figure 7.4: Anodic scans obtained from CV for LFO/LNO/n-STO films of different LFO and LNO thickness. Data collected in O_2 saturated 0.1 M pH 12.7 KOH aqueous electrolyte at 20 mV s^{-1}

scan rate and 2000 rpm rotation. (Inset) Current density measured for 2 nm thick LFO film. The 2 nm LFO/n-STO data was taken from Burton *et al.*

7.4 Discussion

The ~130-fold increase in catalysis observed for the LFO/LNO films compared to LFO alone is remarkable. We attribute this result to the interfacial hole doping due to the smaller VBO observed for the LFO/LNO interface (0.28-0.33 eV) than the LFO/STO interface reported previously (2.2 eV). The approximate band alignment diagram based on our experimental and theoretical determination of VBO based on our previous work [197] is summarized in Figure 7.5. Electrons transferred from LFO leave behind holes which move towards the surface (electrolyte-LFO interface) and contribute to water oxidation in the same fashion as holes produced by dopants in, for example, $(La,Sr)FeO_3$ [207]. The hole effective mass is $0.61m_e$, which makes the transportation of these holes in external electric field easier. Thus, creation of holes at the LFO/LNO interface will increase the surface oxidation kinetics, resulting in higher OER activity.

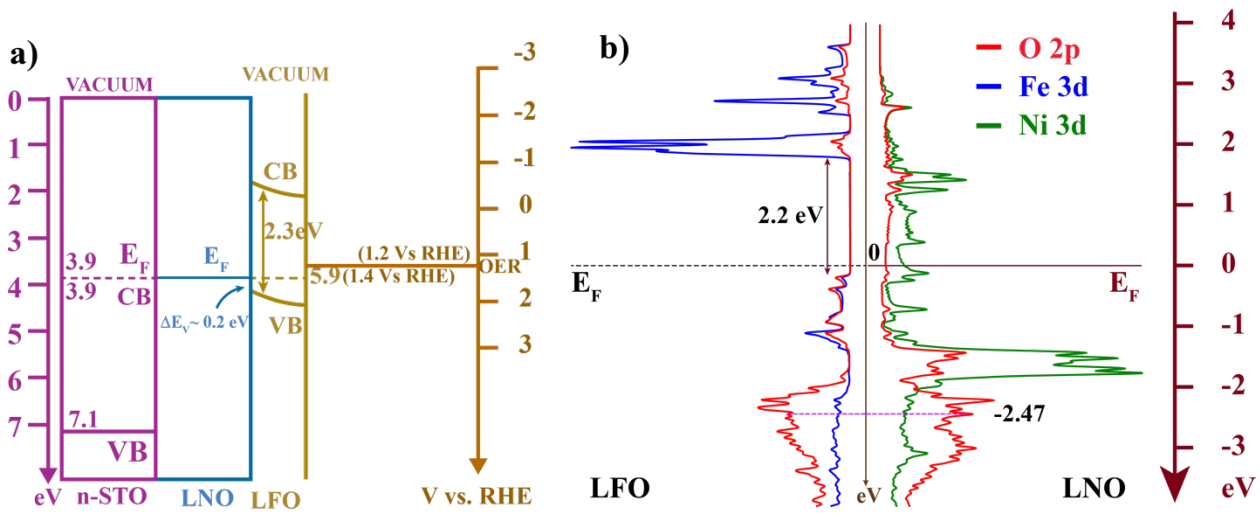

Figure 7.5: Experimental band alignment at STO/LNO/LFO interface b) Theoretical band alignment at LNO/LFO interface. Dashed line(magenta) at -2.47eV represents the O 2p band center at interfacial FeO2 and NiO2 layers.

We see that the VBM in LFO/LNO moves much closer to the OER activation energy (1.23V vs RHE) compared to the LFO/*n*-STO interface, reducing the overpotential significantly [197]. Moreover, during OER catalysis, electrons must travel from solution, through the valence band of LFO, and into the valence (conduction) band of LNO (*n*-STO). The band offset at the LFO/LNO(n-STO) interface thus represents an uphill barrier for charge transfer. The insertion of LNO between STO and LFO thus decreases this barrier significantly and results in greater electrocatalysis.

It is also noteworthy that we do not see evidence of significant formation of Fe^{4+} formal charge states in our heterostructures based on either the DFT predictions or the XPS analysis of the interfaces. Previous analysis by Wang et al. of alloy La(Fe,Ni)O_3 thin films had showed evidence of Fe^{4+} and Ni^{2+} formal charges in some samples with strongly enhanced electrocatalytic performance [13]. DFT models of these alloys also predicted formation of $Fe^{4-\delta}$ formal charge

states at low Fe concentrations (12.5%) but did not use Hubbard U parameters to reproduce the experimental band gap of pure LFO [13]. While we do predict favorable hole transfer into LFO due to the small valence band offset between LNO and LFO, our estimates allude that these hole densities would be insufficient to yield Fe^{4+} formal charge found in those alloys. Further studies of LFO/LNO heterostructures using electron microscopy and X-ray absorption spectroscopy could help to address these open questions.

7.5 Conclusions

We have investigated the electronic structure of the epitaxial LFO/LNO interface theoretically and experimentally and related these insights to the strong OER activity of these heterostructures. Theoretical predictions indicate that the LFO VBM should lie ~0.2 eV below the Fermi level when pinned by an interface with LNO in good agreement with experimental measurements on MBE-grown thin films. We find that the OER activity of the heterostructure is much higher (~130 times) when compared with the LFO and LNO thin films of same thicknesses. The small VBO offers low energy barriers for charge carriers and promotes charge transfer from LFO valence band to LNO. This minimal charge transfer results in partial oxidation of Fe^{3+} and partial reduction of Ni^{3+}, which enhances OER activity with respect to LFO/*n*-STO interface. Thus, our study highlights the importance of band engineering in developing a highly efficient OER catalyst.

Chapter 8

Conclusions and Future work

8.1 Conclusions

This dissertation is focused on two different topics. First, synthesis of perovskite TMO thin films using plasma assisted molecular beam epitaxy and tuning their electronic properties via thickness variation, cation substitution, and creating thin film heterostructures. Second, electrochemical characterization of these structures to understand the effect of these changes in the electronic structure on their OER catalytic performance. Electrochemical measurements in this dissertation are the result of our collaborative work with the Auburn Department of Chemistry.

Synthesizing high quality single crystal perovskite TMO thin films is a challenging task. By optimizing the interplay between oxygen pressure and substrate temperature, ideal crystallinity and stoichiometry in thin films can be achieved. We show how the shuttered growth technique is ideal for synthesis of layered perovskite oxides. Employing a shuttered growth technique offers additional controllable parameter to thin film synthesis. By calibrating atomic flux and shuttering time, layer-by-layer growth can be achieved, which allows us to precisely control thickness of the thin films. Post-growth annealing in oxygen plasma during cooldown was particularly useful to adequately oxidize TMO thin films to produce defect free samples. *In situ* RHEED, *in vacuo* XPS along with XRD serve as a valuable tool to study the surface, interface, and bulk of the thin films and heterostructures.

Film thickness offers an additional controllable parameter to tune the electronic properties in thin films. Just by varying thickness metal-to-insulator phase transition, ferromagnetic to

antiferromagnetic phases have been discovered in TMO thin films [47,48,50]. The change in thickness of the LFO thin films affects the electronic behavior. We observed *n*-type behavior in thin films with thicknesses below 2.5nm, whereas thicker films exhibited intrinsic behavior as in the bulk. The effect of thickness variation was significant in the OER activity. The volcano like trend was observed in OER activity with different film thicknesses. The thinner films being n-type exhibited poor OER catalytic performance due to large valence band offset at LFO/STO interface. OER property in thin films thicker than 2.5 is influenced by the intrinsic nature of LFO and surface states. Therefore, 6nm thickness being the most active OER catalyst.

Heterostructure interfaces are critical in designing new material properties. Octahedral coupling increases the hybridization between O 2p and TM 3d orbitals leading to new properties [219]. Novel properties emerge as a result of interfacial charge transfer due to band alignment at the interface [84,85,191]. It is possible to devise a new electronic state by suitable band engineering in oxide heterostructures. The LFO/LNO heterostructure was a novel work that resulted from our efforts to create an efficient OER catalyst. Due to band alignment at the LFO/LNO interface, there is a small valence band offset (~0.2-0.3 eV) at the interface. First principles DFT+U calculations were performed to determine the valence band offset at the LFO/LNO interface and determined to be ~0.2 eV. The valence band offset was determined experimentally from XPS data, which was ~0.3 eV. Considering the error bar of 0.1 eV in experimental results, theoretical and experimental valence band offset agrees well. This is a very encouraging result. Furthermore, we found a significant increase in OER activity and a decrease in overpotential in the heterostructure. We estimated the thermally created hole density to be of the order of 10^{16} cm^{-2} assuming a band offset of 0.2 eV. Even though the density of holes is not significant as a charge carrier, surface holes act as active sites for oxidation resulting in higher oxidation kinetics. We conclude that the increased

OER performance is the consequence of small valence band offset and thermally generated surface holes.

Cation substitution is a way to increase the carrier concentration in thin films. The substitution of Sr^{2+} in the A-site increases the hole concentration in LFO. The added holes have significant impact on catalytic property of LFO thin films. Our result shows that the added holes mostly reside in oxygen lattice creating an oxygen hole. Some of the holes spill over to the surface which are the active site for oxidation of water molecules. Therefore, the surface oxygen holes enhance the oxidation kinetics leading to a higher oxidation current. The effect of Sr^{2+} substitution was more dramatic than other methods explained previously. More investigation is necessary to establish a correlation between OER activity and the Sr^{2+} substitution level.

8.2 Future Work

This work provides an insight in exploiting the electronic structure to optimize the OER performance. Also, it leaves us with clear future directions to explore to optimize the OER performance of LFO thin films. Even though Sr^{2+} substitution in A-site has been investigated quite a lot, it would be worthwhile to study LFO thin films with wide range of Sr^{2+} concentration to fully understand the OER performance for different level of Sr^{2+} substitution. The combination of optimal LFO thickness and optimal level of Sr^{2+} substitution is another interesting area to explore.

The small valence band offset at LFO/LNO heterostructure highlights the importance of heterostructure and opens the door for further research. XAS measurement could be performed to measure the TM 3d - O2p hybridization in heterostructure samples. One immediate area of study could be the thickness variation of LFO and LNO in the heterostructure. One step further, investigation of LFO capped LSFO samples could yield interesting results. We know LFO

provides stability and band alignment at LFO/LSFO is yet to be explored. These are some of the research areas that could be explored to design an efficient OER catalyst.

References:

[1] N. S. Lewis and D. G. Nocera, *Powering the Planet: Chemical Challenges in Solar Energy Utilization*, Proceedings of the National Academy of Sciences **103**, 15729 (2006).

[2] C. Song, *Global Challenges and Strategies for Control, Conversion and Utilization of CO2 for Sustainable Development Involving Energy, Catalysis, Adsorption and Chemical Processing*, Catal. Today **115**, 2 (2006).

[3] A. Fujishima and K. Honda, *Electrochemical Photolysis of Water at a Semiconductor Electrode*, Nature **238**, 5358 (1972).

[4] J. Suntivich, H. A. Gasteiger, N. Yabuuchi, H. Nakanishi, J. B. Goodenough, and Y. Shao-Horn, *Design Principles for Oxygen Reduction Activity on Perovskite Oxide Catalysts for Fuel Cells and Metal-Air Batteries*, Nat. Chem. **3**, 546 (2011).

[5] Z.-L. Wang, D. Xu, J.-J. Xu, and X.-B. Zhang, *Oxygen Electrocatalysts in Metal–Air Batteries: From Aqueous to Nonaqueous Electrolytes*, Chem. Soc. Rev. **43**, 7746 (2014).

[6] J. Xu, C. Chen, Z. Han, Y. Yang, J. Li, and Q. Deng, *Recent Advances in Oxygen Electrocatalysts Based on Perovskite Oxides*, Nanomaterials **9**, 8 (2019).

[7] L. Han, S. Dong, and E. Wang, *Transition-Metal (Co, Ni, and Fe)-Based Electrocatalysts for the Water Oxidation Reaction*, Advanced Materials **28**, 9266 (2016).

[8] J. Suntivich, K. J. May, H. A. Gasteiger, J. B. Goodenough, and Y. Shao-Horn, *A Perovskite Oxide Optimized for Oxygen Evolution Catalysis from Molecular Orbital Principles*, Science **334**, 1383 (2011).

[9] A. Li, Y. Sun, T. Yao, and H. Han, *Earth-Abundant Transition-Metal-Based Electrocatalysts for Water Electrolysis to Produce Renewable Hydrogen*, Chemistry – A European Journal **24**, 18334 (2018).

[10] J. O. Bockris and T. Otagawa, *The Electrocatalysis of Oxygen Evolution on Perovskites*, J. Electrochem. Soc. **131**, 290 (1984).

[11] J. R. Petrie, V. R. Cooper, J. W. Freeland, T. L. Meyer, Z. Zhang, D. A. Lutterman, and H. N. Lee, *Enhanced Bifunctional Oxygen Catalysis in Strained LaNiO3 Perovskites*, J. Am. Chem. Soc. **138**, 2488 (2016).

[12] J. Suntivich, W. T. Hong, Y.-L. Lee, J. M. Rondinelli, W. Yang, J. B. Goodenough, B. Dabrowski, J. W. Freeland, and Y. Shao-Horn, *Estimating Hybridization of Transition Metal and Oxygen States in Perovskites from O K-Edge X-Ray Absorption Spectroscopy*, J. Phys. Chem. C **118**, 1856 (2014).

[13] L. Wang et al., *Understanding the Electronic Structure Evolution of Epitaxial LaNi1–XFexO3 Thin Films for Water Oxidation*, Nano Lett. **21**, 8324 (2021).

[14] B. Raveau, *Strongly Correlated Electron Systems: From Chemistry to Physics*, Comptes Rendus Chimie **14**, 856 (2011).

[15] A. T. Bollinger, G. Dubuis, J. Yoon, D. Pavuna, J. Misewich, and I. Božović, *Superconductor–Insulator Transition in La2 − XSr x CuO4 at the Pair Quantum Resistance*, Nature **472**, 7344 (2011).

[16] L. S. Bilbro, R. V. Aguilar, G. Logvenov, O. Pelleg, I. Božović, and N. P. Armitage, *Temporal Correlations of Superconductivity above the Transition Temperature in La2−xSrxCuO4 Probed by Terahertz Spectroscopy*, Nature Phys **7**, 4 (2011).

[17] Y. Maeno, H. Hashimoto, K. Yoshida, S. Nishizaki, T. Fujita, J. G. Bednorz, and F. Lichtenberg, *Superconductivity in a Layered Perovskite without Copper*, Nature **372**, 6506 (1994).

[18] Y. Nomura and R. Arita, *Superconductivity in Infinite-Layer Nickelates*, Rep. Prog. Phys. **85**, 052501 (2022).

[19] Y. Ji, J. Liu, L. Li, and Z. Liao, *Superconductivity in Infinite Layer Nickelates*, Journal of Applied Physics **130**, 060901 (2021).

[20] M. Imada, A. Fujimori, and Y. Tokura, *Metal-Insulator Transitions*, Rev. Mod. Phys. **70**, 1039 (1998).

[21] D. Meyers et al., *Pure Electronic Metal-Insulator Transition at the Interface of Complex Oxides*, Sci Rep **6**, 1 (2016).

[22] A. J. Hauser, E. Mikheev, N. E. Moreno, J. Hwang, J. Y. Zhang, and S. Stemmer, *Correlation between Stoichiometry, Strain, and Metal-Insulator Transitions of NdNiO3 Films*, Appl. Phys. Lett. **106**, 092104 (2015).

[23] S. Banik, K. Das, T. Paramanik, N. P. Lalla, B. Satpati, K. Pradhan, and I. Das, *Huge Magnetoresistance and Ultrasharp Metamagnetic Transition in Polycrystalline Sm0.5Ca0.25Sr0.25MnO3*, NPG Asia Mater **10**, 9 (2018).

[24] Y. Moritomo, A. Asamitsu, H. Kuwahara, and Y. Tokura, *Giant Magnetoresistance of Manganese Oxides with a Layered Perovskite Structure*, Nature **380**, 6570 (1996).

[25] M. Uehara, S. Mori, C. H. Chen, and S.-W. Cheong, *Percolative Phase Separation Underlies Colossal Magnetoresistance in Mixed-Valent Manganites*, Nature **399**, 6736 (1999).

[26] M. Čebela, D. Zagorac, K. Batalović, J. Radaković, B. Stojadinović, V. Spasojević, and R. Hercigonja, *BiFeO3 Perovskites: A Multidisciplinary Approach to Multiferroics*, Ceramics International **43**, 1256 (2017).

[27] W. Eerenstein, N. D. Mathur, and J. F. Scott, *Multiferroic and Magnetoelectric Materials*, Nature **442**, 7104 (2006).

[28] J. Wang et al., *Epitaxial BiFeO3 Multiferroic Thin Film Heterostructures*, Science **299**, 1719 (2003).

[29] T. Goto, T. Kimura, G. Lawes, A. P. Ramirez, and Y. Tokura, *Ferroelectricity and Giant Magnetocapacitance in Perovskite Rare-Earth Manganites*, Phys. Rev. Lett. **92**, 257201 (2004).

[30] W. Prellier, M. P. Singh, and P. Murugavel, *The Single-Phase Multiferroic Oxides: From Bulk to Thin Film*, J. Phys.: Condens. Matter **17**, R803 (2005).

[31] Y. Sun, G. Chen, S. Xi, and Z. J. Xu, *Catalytically Influential Features in Transition Metal Oxides*, ACS Catal. **11**, 13947 (2021).

[32] L. Pan and G. Zhu, *Perovskite Materials: Synthesis, Characterisation, Properties, and Applications* (BoD – Books on Demand, 2016).

[33] X. Wang et al., *Eg Occupancy as an Effective Descriptor for the Catalytic Activity of Perovskite Oxide-Based Peroxidase Mimics*, Nat Commun **10**, 1 (2019).

[34] F. H. B. Lima, J. Zhang, M. H. Shao, K. Sasaki, M. B. Vukmirovic, E. A. Ticianelli, and R. R. Adzic, *Catalytic Activity−d-Band Center Correlation for the O2 Reduction Reaction on Platinum in Alkaline Solutions*, J. Phys. Chem. C **111**, 404 (2007).

[35] K. J. May, D. P. Fenning, T. Ming, W. T. Hong, D. Lee, K. A. Stoerzinger, M. D. Biegalski, A. M. Kolpak, and Y. Shao-Horn, *Thickness-Dependent Photoelectrochemical Water Splitting on Ultrathin LaFeO3 Films Grown on Nb:SrTiO3*, J. Phys. Chem. Lett. **6**, 977 (2015).

[36] K. Momma and F. Izumi, *VESTA 3 for Three-Dimensional Visualization of Crystal, Volumetric and Morphology Data*, J Appl Cryst **44**, 6 (2011).

[37] C. Li, X. Lu, W. Ding, L. Feng, Y. Gao, and Z. Guo, *Formability of ABX3 (X = F, Cl, Br, I) Halide Perovskites*, Acta Cryst B **64**, 6 (2008).

[38] M. A. Peña and J. L. G. Fierro, *Chemical Structures and Performance of Perovskite Oxides*, Chem. Rev. **101**, 1981 (2001).

[39] H. Tanaka and M. Misono, *Advances in Designing Perovskite Catalysts*, Current Opinion in Solid State and Materials Science **5**, 381 (2001).

[40] P. Hohenberg and W. Kohn, *Inhomogeneous Electron Gas*, Phys. Rev. **136**, B864 (1964).

[41] W. Kohn and L. J. Sham, *Self-Consistent Equations Including Exchange and Correlation Effects*, Phys. Rev. **140**, A1133 (1965).

[42] L. A. Agapito, S. Curtarolo, and M. Buongiorno Nardelli, *Reformulation of $\mathrm{DFT}+U$ as a Pseudohybrid Hubbard Density Functional for Accelerated Materials Discovery*, Phys. Rev. X **5**, 011006 (2015).

[43] B. Himmetoglu, A. Floris, S. de Gironcoli, and M. Cococcioni, *Hubbard-Corrected DFT Energy Functionals: The LDA+U Description of Correlated Systems*, International Journal of Quantum Chemistry **114**, 14 (2014).

[44] J. Hubbard, *Electron Correlations in Narrow Energy Bands*, Proceedings of the Royal Society of London. Series A, Mathematical and Physical Sciences **276**, 238 (1963).

[45] *Planewaves, Pseudopotentials, and the LAPW Method* (n.d.).

[46] J. K. Nørskov, T. Bligaard, J. Rossmeisl, and C. H. Christensen, *Towards the Computational Design of Solid Catalysts*, Nature Chemistry **1**, (2009).

[47] A. V. Boris et al., *Dimensionality Control of Electronic Phase Transitions in Nickel-Oxide Superlattices*, Science **332**, 937 (2011).

[48] K. Yoshimatsu, T. Okabe, H. Kumigashira, S. Okamoto, S. Aizaki, A. Fujimori, and M. Oshima, *Dimensional-Crossover-Driven Metal-Insulator Transition in ${\mathrm{SrVO}}_{3}$ Ultrathin Films*, Phys. Rev. Lett. **104**, 147601 (2010).

[49] M. Huijben, L. W. Martin, Y.-H. Chu, M. B. Holcomb, P. Yu, G. Rijnders, D. H. A. Blank, and R. Ramesh, *Critical Thickness and Orbital Ordering in Ultrathin ${\text{La}}_{0.7}{\text{Sr}}_{0.3}{\text{MnO}}_{3}$ Films*, Phys. Rev. B **78**, 094413 (2008).

[50] J. Junquera and P. Ghosez, *Critical Thickness for Ferroelectricity in Perovskite Ultrathin Films*, Nature **422**, 6931 (2003).

[51] A. R. Burton, R. Paudel, B. Matthews, M. Sassi, S. R. Spurgeon, B. H. Farnum, and R. B. Comes, *Thickness Dependent OER Electrocatalysis of Epitaxial LaFeO$_{3}$ Thin Films*, ArXiv:2108.09360 [Cond-Mat] (2021).

[52] A. R. C. Bredar, M. D. Blanchet, A. R. Burton, B. E. Matthews, S. R. Spurgeon, R. B. Comes, and B. H. Farnum, *Oxygen Reduction Electrocatalysis with Epitaxially Grown Spinel MnFe2O4 and Fe3O4*, ACS Catal. **12**, 3577 (2022).

[53] M. Ohring, *Chapter 8 - Epitaxy*, in *Materials Science of Thin Films (Second Edition)*, edited by M. Ohring (Academic Press, San Diego, 2002), pp. 417–494.

[54] H. Kroemer, *Nobel Lecture: Quasielectric Fields and Band Offsets: Teaching Electrons New Tricks*, Rev. Mod. Phys. **73**, 783 (2001).

[55] J. Mannhart and D. G. Schlom, *Oxide Interfaces: An Opportunity for Electronics*, Science **327**, 1607 (2010).

[56] J. M. D. Coey, Ariando, and W. E. Pickett, *Magnetism at the Edge: New Phenomena at Oxide Interfaces*, MRS Bulletin **38**, 1040 (2013).

[57] A. Ohtomo and H. Y. Hwang, *A High-Mobility Electron Gas at the LaAlO3/SrTiO3 Heterointerface*, Nature **427**, 423 (2004).

[58] J. E. Kleibeuker et al., *Electronic Reconstruction at the Isopolar ${\mathrm{LaTiO}}_{3}/{\mathrm{LaFeO}}_{3}$ Interface: An X-Ray Photoemission and Density-Functional Theory Study*, Phys. Rev. Lett. **113**, 237402 (2014).

[59] R. U. Chandrasena et al., *Depth-Resolved Charge Reconstruction at the $\mathrm{LaNi}{\mathrm{O}}_{3}/\mathrm{CaMn}{\mathrm{O}}_{3}$ Interface*, Phys. Rev. B **98**, 155103 (2018).

[60] H. Y. Hwang, Y. Iwasa, M. Kawasaki, B. Keimer, N. Nagaosa, and Y. Tokura, *Emergent Phenomena at Oxide Interfaces*, Nature Mater **11**, 2 (2012).

[61] H. Zaid et al., *Atomic-Resolved Depth Profile of Strain and Cation Intermixing around LaAlO3/SrTiO3 Interfaces*, Sci Rep **6**, 1 (2016).

[62] J. Mannhart, D. H. A. Blank, H. Y. Hwang, A. J. Millis, and J. M. Triscone, *Two-Dimensional Electron Gases at Oxide Interfaces*, MRS Bulletin **33**, 1027 (2008).

[63] A. Ohtomo, D. A. Muller, J. L. Grazul, and H. Y. Hwang, *Artificial Charge-Modulationin Atomic-Scale Perovskite Titanate Superlattices*, Nature **419**, 6905 (2002).

[64] R. Ohtsuka, M. Matvejeff, K. Nishio, R. Takahashi, and M. Lippmaa, *Transport Properties of LaTiO3/SrTiO3 Heterostructures*, Appl. Phys. Lett. **96**, 192111 (2010).

[65] N. Reyren et al., *Superconducting Interfaces Between Insulating Oxides*, Science **317**, 1196 (2007).

[66] P. Delugas, A. Filippetti, V. Fiorentini, D. I. Bilc, D. Fontaine, and P. Ghosez, *Spontaneous 2-Dimensional Carrier Confinement at the n-Type ${\mathrm{SrTiO}}_{3}/{\mathrm{LaAlO}}_{3}$ Interface*, Phys. Rev. Lett. **106**, 166807 (2011).

[67] M. Salluzzo et al., *Orbital Reconstruction and the Two-Dimensional Electron Gas at the ${\mathrm{LaAlO}}_{3}/{\mathrm{SrTiO}}_{3}$ Interface*, Phys. Rev. Lett. **102**, 166804 (2009).

[68] Z. Liao et al., *Controlled Lateral Anisotropy in Correlated Manganite Heterostructures by Interface-Engineered Oxygen Octahedral Coupling*, Nature Mater **15**, 4 (2016).

[69] K. S. Takahashi, M. Kawasaki, and Y. Tokura, *Interface Ferromagnetism in Oxide Superlattices of CaMnO3/CaRuO3*, Appl. Phys. Lett. **79**, 1324 (2001).

[70] K. G. Rana, V. Khikhlovskyi, and T. Banerjee, *Electrical Transport across Au/Nb:SrTiO3 Schottky Interface with Different Nb Doping*, Appl. Phys. Lett. **100**, 213502 (2012).

[71] M. Choi et al., *Structural, Optical, and Electrical Properties of Strained La-Doped SrTiO3 Films*, Journal of Applied Physics **116**, 043705 (2014).

[72] F. Calle-Vallejo, N. G. Inoglu, H.-Y. Su, J. I. Martínez, I. C. Man, M. T. M. Koper, J. R. Kitchin, and J. Rossmeisl, *Number of Outer Electrons as Descriptor for Adsorption Processes on Transition Metals and Their Oxides*, Chem. Sci. **4**, 1245 (2013).

[73] W. T. Hong, K. A. Stoerzinger, Y.-L. Lee, L. Giordano, A. Grimaud, A. M. Johnson, J. Hwang, E. J. Crumlin, W. Yang, and Y. Shao-Horn, *Charge-Transfer-Energy-Dependent Oxygen Evolution Reaction Mechanisms for Perovskite Oxides*, Energy Environ. Sci. **10**, 2190 (2017).

[74] L. Wang et al., *Understanding the Electronic Structure Evolution of Epitaxial LaNi1–XFexO3 Thin Films for Water Oxidation*, Nano Lett. **21**, 8324 (2021).

[75] J. Liu et al., *Tuning the Electronic Structure of LaNiO3 through Alloying with Strontium to Enhance Oxygen Evolution Activity*, Advanced Science **6**, 1901073 (2019).

[76] A. Grimaud, K. J. May, C. E. Carlton, Y.-L. Lee, M. Risch, W. T. Hong, J. Zhou, and Y. Shao-Horn, *Double Perovskites as a Family of Highly Active Catalysts for Oxygen Evolution in Alkaline Solution*, Nat Commun **4**, 1 (2013).

[77] Y. Cao, X. Liu, M. Kareev, D. Choudhury, S. Middey, D. Meyers, J.-W. Kim, P. J. Ryan, J. W. Freeland, and J. Chakhalian, *Engineered Mott Ground State in a LaTiO3+δ/LaNiO3 Heterostructure*, Nat Commun **7**, 1 (2016).

[78] J. Liu et al., *Heterointerface Engineered Electronic and Magnetic Phases of NdNiO3 Thin Films*, Nat Commun **4**, 1 (2013).

[79] J. Hwang, J. Y. Zhang, J. Son, and S. Stemmer, *Nanoscale Quantification of Octahedral Tilts in Perovskite Films*, Appl. Phys. Lett. **100**, 191909 (2012).

[80] D. Pesquera, G. Herranz, A. Barla, E. Pellegrin, F. Bondino, E. Magnano, F. Sánchez, and J. Fontcuberta, *Surface Symmetry-Breaking and Strain Effects on Orbital Occupancy in Transition Metal Perovskite Epitaxial Films*, Nat Commun **3**, 1 (2012).

[81] K. A. Stoerzinger, W. S. Choi, H. Jeen, H. N. Lee, and Y. Shao-Horn, *Role of Strain and Conductivity in Oxygen Electrocatalysis on LaCoO3 Thin Films*, J. Phys. Chem. Lett. **6**, 487 (2015).

[82] T. Hirakawa and P. V. Kamat, *Charge Separation and Catalytic Activity of Ag@TiO2 Core-Shell Composite Clusters under UV-Irradiation*, J Am Chem Soc **127**, 3928 (2005).

[83] I. González, S. Okamoto, S. Yunoki, A. Moreo, and E. Dagotto, *Charge Transfer in Heterostructures of Strongly Correlated Materials*, J. Phys.: Condens. Matter **20**, 264002 (2008).

[84] J. Hoffman, I. C. Tung, B. B. Nelson-Cheeseman, M. Liu, J. W. Freeland, and A. Bhattacharya, *Charge Transfer and Interfacial Magnetism in (LaNiO${}_{3}$)${}_{n}$/(LaMnO${}_{3}$)${}_{2}$ Superlattices*, Phys. Rev. B **88**, 144411 (2013).

[85] Z. Zhong and P. Hansmann, *Band Alignment and Charge Transfer in Complex Oxide Interfaces*, Phys. Rev. X **7**, 011023 (2017).

[86] H. Park, A. J. Millis, and C. A. Marianetti, *Total Energy Calculations Using DFT+DMFT: Computing the Pressure Phase Diagram of the Rare Earth Nickelates*, Phys. Rev. B **89**, 245133 (2014).

[87] Y.-L. Lee and D. Morgan, *Ab Initio Defect Energetics of Perovskite (001) Surfaces for Solid Oxide Fuel Cells: A Comparative Study of $\mathrm{LaMn}{\mathrm{O}}_{3}$ versus $\mathrm{SrTi}{\mathrm{O}}_{3}$ and $\mathrm{LaAl}{\mathrm{O}}_{3}$*, Phys. Rev. B **91**, 195430 (2015).

[88] K. J. May and A. M. Kolpak, *Improved Description of Perovskite Oxide Crystal Structure and Electronic Properties Using Self-Consistent Hubbard U Corrections from ACBN0*, Phys. Rev. B **101**, 165117 (2020).

[89] J. P. Perdew, K. Burke, and M. Ernzerhof, *Generalized Gradient Approximation Made Simple*, Phys. Rev. Lett. **77**, 3865 (1996).

[90] P. Giannozzi et al., *QUANTUM ESPRESSO: A Modular and Open-Source Software Project for Quantum Simulations of Materials*, Journal of Physics: Condensed Matter **21**, 395502 (2009).

[91] P. Giannozzi et al., *Advanced Capabilities for Materials Modelling with Quantum ESPRESSO*, J. Phys.: Condens. Matter **29**, 465901 (2017).

[92] D. Vanderbilt, *Soft Self-Consistent Pseudopotentials in a Generalized Eigenvalue Formalism*, Phys. Rev. B **41**, 7892 (1990).

[93] P. E. Blöchl, *Projector Augmented-Wave Method*, Phys. Rev. B **50**, 17953 (1994).

[94] P. a. M. Dirac, *Note on Exchange Phenomena in the Thomas Atom*, Mathematical Proceedings of the Cambridge Philosophical Society **26**, 376 (1930).

[95] J. P. Perdew and Y. Wang, *Accurate and Simple Analytic Representation of the Electron-Gas Correlation Energy*, Phys. Rev. B **45**, 13244 (1992).

[96] J. P. Perdew, *Density Functional Theory and the Band Gap Problem*, International Journal of Quantum Chemistry **28**, 497 (1985).

[97] L. J. Sham and M. Schlüter, *Density-Functional Theory of the Band Gap*, Phys. Rev. B **32**, 3883 (1985).

[98] S. L. Dudarev, G. A. Botton, S. Y. Savrasov, C. J. Humphreys, and A. P. Sutton, *Electron-Energy-Loss Spectra and the Structural Stability of Nickel Oxide: An LSDA+U Study*, Phys. Rev. B **57**, 1505 (1998).

[99] A. I. Liechtenstein, V. I. Anisimov, and J. Zaanen, *Density-Functional Theory and Strong Interactions: Orbital Ordering in Mott-Hubbard Insulators*, Phys. Rev. B **52**, R5467 (1995).

[100] A. G. Petukhov, I. I. Mazin, L. Chioncel, and A. I. Lichtenstein, *Correlated Metals and the $\mathrm{LDA}+U$ Method*, Phys. Rev. B **67**, 153106 (2003).

[101] B. A. Joyce, *Molecular Beam Epitaxy*, Rep. Prog. Phys. **48**, 1637 (1985).

[102] K. Ploog, A. Fischer, R. Trommer, and M. Hirose, *MBE-grown Insulating Oxide Films on GaAs*, Journal of Vacuum Science and Technology **16**, 290 (1979).

[103] J. G. Bednorz and K. A. Müller, *Possible HighTc Superconductivity in the Ba−La−Cu−O System*, Z. Physik B - Condensed Matter **64**, 189 (1986).

[104] D. D. Berkley et al., *In Situ Formation of Superconducting YBa2Cu3O7−x Thin Films Using Pure Ozone Vapor Oxidation*, Appl. Phys. Lett. **53**, 1973 (1988).

[105] Y. Nakayama, I. Tsukada, A. Maeda, and K. Uchinokura, *Epitaxial Growth of Bi-Sr-Ca-Cu-O Thin Films by Molecular Beam Epitaxy Technique with Shutter Control*, Jpn. J. Appl. Phys. **28**, L1809 (1989).

[106] B. Jalan, R. Engel-Herbert, N. J. Wright, and S. Stemmer, *Growth of High-Quality SrTiO3 Films Using a Hybrid Molecular Beam Epitaxy Approach*, Journal of Vacuum Science & Technology A **27**, 461 (2009).

[107] *Frontiers in the Growth of Complex Oxide Thin Films: Past, Present, and Future of Hybrid MBE - Brahlek - 2018 - Advanced Functional Materials - Wiley Online Library*, https://onlinelibrary.wiley.com/doi/full/10.1002/adfm.201702772.

[108] E. S. Hellman and E. H. Hartford, *Effects of Oxygen on the Sublimation of Alkaline Earths from Effusion Cells*, Journal of Vacuum Science & Technology B: Microelectronics and Nanometer Structures Processing, Measurement, and Phenomena **12**, 1178 (1994).

[109] Y.-S. Kim, N. Bansal, and S. Oh, *Simple Self-Gettering Differential-Pump for Minimizing Source Oxidation in Oxide-MBE Environment*, Journal of Vacuum Science & Technology A **29**, 041505 (2011).

[110] M. Brahlek, L. Zhang, C. Eaton, H.-T. Zhang, and R. Engel-Herbert, *Accessing a Growth Window for SrVO3 Thin Films*, Appl. Phys. Lett. **107**, 143108 (2015).

[111] B. Jalan, J. Cagnon, T. E. Mates, and S. Stemmer, *Analysis of Carbon in SrTiO3 Grown by Hybrid Molecular Beam Epitaxy*, Journal of Vacuum Science & Technology A **27**, 1365 (2009).

[112] S. Thapa, S. R. Provence, D. Jessup, J. Lapano, M. Brahlek, J. T. Sadowski, P. Reinke, W. Jin, and R. B. Comes, *Correlating Surface Stoichiometry and Termination in SrTiO3 Films Grown by Hybrid Molecular Beam Epitaxy*, Journal of Vacuum Science & Technology A **39**, 053203 (2021).

[113] *Molecular Beam Epitaxy - 1st Edition*, https://www.elsevier.com/books/molecular-beam-epitaxy/farrow/978-0-8155-1371-1.

[114] J. H. Haeni, C. D. Theis, and D. G. Schlom, *RHEED Intensity Oscillations for the Stoichiometric Growth of SrTiO3 Thin Films by Reactive Molecular Beam Epitaxy*, Journal of Electroceramics **4**, 385 (2000).

[115] M. Ohring, *Chapter 7 - Substrate Surfaces and Thin-Film Nucleation*, in *Materials Science of Thin Films (Second Edition)*, edited by M. Ohring (Academic Press, San Diego, 2002), pp. 357–415.

[116] F. C. Frank and J. H. van der Merwe, *One-Dimensional Dislocations. I. Static Theory*, Proceedings of the Royal Society of London. Series A, Mathematical and Physical Sciences **198**, 205 (1949).

[117] R. L. Schwoebel and E. J. Shipsey, *Step Motion on Crystal Surfaces*, Journal of Applied Physics **37**, 3682 (1966).

[118] R. L. Schwoebel, *Step Motion on Crystal Surfaces. II*, Journal of Applied Physics **40**, 614 (1969).

[119] M. C. Sullivan, M. J. Ward, A. Gutiérrez-Llorente, E. R. Adler, H. Joress, A. Woll, and J. D. Brock, *Complex Oxide Growth Using Simultaneous in Situ Reflection High-Energy Electron Diffraction and x-Ray Reflectivity: When Is One Layer Complete?*, Appl. Phys. Lett. **106**, 031604 (2015).

[120] W. Hong, H. N. Lee, M. Yoon, H. M. Christen, D. H. Lowndes, Z. Suo, and Z. Zhang, *Persistent Step-Flow Growth of Strained Films on Vicinal Substrates*, Phys. Rev. Lett. **95**, 095501 (2005).

[121] M. D. Rossell, R. Erni, M. P. Prange, J.-C. Idrobo, W. Luo, R. J. Zeches, S. T. Pantelides, and R. Ramesh, *Atomic Structure of Highly Strained ${\mathrm{BiFeO}}_{3}$ Thin Films*, Phys. Rev. Lett. **108**, 047601 (2012).

[122] *Phys. Rev. Lett. 105, 057601 (2010) - Bridging Multiferroic Phase Transitions by Epitaxial Strain in ${\mathrm{BiFeO}}_{3}$*, https://journals.aps.org/prl/abstract/10.1103/PhysRevLett.105.057601.

[123] *Critical Thickness and Strain Relaxation in Molecular Beam Epitaxy-Grown SrTiO3 Films: Applied Physics Letters: Vol 103, No 21*, https://aip.scitation.org/doi/full/10.1063/1.4833248.

[124] C. Adamo et al., *Effect of Biaxial Strain on the Electrical and Magnetic Properties of (001) La0.7Sr0.3MnO3 Thin Films*, Appl. Phys. Lett. **95**, 112504 (2009).

[125] C. Ederer and N. A. Spaldin, *Effect of Epitaxial Strain on the Spontaneous Polarization of Thin Film Ferroelectrics*, Phys. Rev. Lett. **95**, 257601 (2005).

[126] Z. Wang, F. Li, S. Meng, J. Zhang, E. W. Plummer, U. Diebold, and J. Guo, *Strain-Induced Defect Superstructure on the ${\mathrm{SrTiO}}_{3}(110)$ Surface*, Phys. Rev. Lett. **111**, 056101 (2013).

[127] S. Kuprenaite, V. Astié, S. Margueron, C. Millon, J.-M. Decams, Z. Saltyte, P. Boulet, V. Plausinaitiene, A. Abrutis, and A. Bartasyte, *Relationship Processing–Composition–Structure–Resistivity of LaNiO3 Thin Films Grown by Chemical Vapor Deposition Methods*, Coatings **9**, 1 (2019).

[128] H. I. Seo, S. Woo, J. Kim, S. G. Jeong, T. Park, and W. S. Choi, *Crystalline Symmetry-Dependent Magnon Formation in the Itinerant Ferromagnet $\mathrm{SrRu}{\mathrm{O}}_{3}$*, Phys. Rev. B **103**, 045104 (2021).

[129] Z. Q. Liu, Z. Huang, W. M. Lü, K. Gopinadhan, X. Wang, A. Annadi, T. Venkatesan, and Ariando, *Atomically Flat Interface between a Single-Terminated LaAlO3 Substrate and SrTiO3 Thin Film Is Insulating*, AIP Advances **2**, 012147 (2012).

[130] G. Koster, B. L. Kropman, G. J. H. M. Rijnders, D. H. A. Blank, and H. Rogalla, *Quasi-Ideal Strontium Titanate Crystal Surfaces through Formation of Strontium Hydroxide*, Appl. Phys. Lett. **73**, 2920 (1998).

[131] M. G. Blamire, J. L. MacManus-Driscoll, N. D. Mathur, and Z. H. Barber, *The Materials Science of Functional Oxide Thin Films*, Advanced Materials **21**, 3827 (2009).

[132] J. H. Song, T. Susaki, and H. Y. Hwang, *Enhanced Thermodynamic Stability of Epitaxial Oxide Thin Films*, Advanced Materials **20**, 2528 (2008).

[133] J. Dho, X. Qi, H. Kim, J. L. MacManus-Driscoll, and M. G. Blamire, *Large Electric Polarization and Exchange Bias in Multiferroic BiFeO3*, Advanced Materials **18**, 1445 (2006).

[134] J. E. Mahan, K. M. Geib, G. Y. Robinson, and R. G. Long, *A Review of the Geometrical Fundamentals of Reflection High-energy Electron Diffraction with Application to Silicon Surfaces*, Journal of Vacuum Science & Technology A **8**, 3692 (1990).

[135] F. Tang, T. Parker, G.-C. Wang, and T.-M. Lu, *Surface Texture Evolution of Polycrystalline and Nanostructured Films: RHEED Surface Pole Figure Analysis*, J. Phys. D: Appl. Phys. **40**, R427 (2007).

[136] S. Thapa, R. Paudel, M. D. Blanchet, P. T. Gemperline, and R. B. Comes, *Probing Surfaces and Interfaces in Complex Oxide Films via in Situ X-Ray Photoelectron Spectroscopy*, Journal of Materials Research **36**, 26 (2021).

[137] S. J. Roosendaal, B. van Asselen, J. W. Elsenaar, A. M. Vredenberg, and F. H. P. M. Habraken, *The Oxidation State of Fe(100) after Initial Oxidation in O2*, Surface Science **442**, 329 (1999).

[138] P. C. J. Graat and M. A. J. Somers, *Simultaneous Determination of Composition and Thickness of Thin Iron-Oxide Films from XPS Fe 2p Spectra*, Applied Surface Science **100–101**, 36 (1996).

[139] T. Yamashita and P. Hayes, *Analysis of XPS Spectra of Fe2+ and Fe3+ Ions in Oxide Materials*, Applied Surface Science **254**, 2441 (2008).

[140] E. A. Kraut, R. W. Grant, J. R. Waldrop, and S. P. Kowalczyk, *Semiconductor Core-Level to Valence-Band Maximum Binding-Energy Differences: Precise Determination by x-Ray Photoelectron Spectroscopy*, Phys. Rev. B **28**, 1965 (1983).

[141] E. A. Kraut, R. W. Grant, J. R. Waldrop, and S. P. Kowalczyk, *Precise Determination of the Valence-Band Edge in X-Ray Photoemission Spectra: Application to Measurement of Semiconductor Interface Potentials*, Phys. Rev. Lett. **44**, 1620 (1980).

[142] S. A. Chambers, T. Droubay, T. C. Kaspar, and M. Gutowski, *Experimental Determination of Valence Band Maxima for SrTiO3, TiO2, and SrO and the Associated Valence Band Offsets with Si(001)*, Journal of Vacuum Science & Technology B: Microelectronics and Nanometer Structures Processing, Measurement, and Phenomena **22**, 2205 (2004).

[143] G. E. M. Jauncey, *The Scattering of X-Rays and Bragg's Law*, Proceedings of the National Academy of Sciences **10**, 57 (1924).

[144] H. Kiessig, *Untersuchungen Zur Totalreflexion von Röntgenstrahlen*, Annalen Der Physik **402**, 715 (1931).

[145] V. Climent, N. M. Marković, and P. N. Ross, *Kinetics of Oxygen Reduction on an Epitaxial Film of Palladium on Pt(111)*, J. Phys. Chem. B **104**, 3116 (2000).

[146] J. Lüning, F. Nolting, A. Scholl, H. Ohldag, J. W. Seo, J. Fompeyrine, J.-P. Locquet, and J. Stöhr, *Determination of the Antiferromagnetic Spin Axis in Epitaxial ${\mathrm{LaFeO}}_{3}$ Films by X-Ray Magnetic Linear Dichroism Spectroscopy*, Phys. Rev. B **67**, 214433 (2003).

[147] S. E. Dann, D. B. Currie, M. T. Weller, M. F. Thomas, and A. D. Al-Rawwas, *The Effect of Oxygen Stoichiometry on Phase Relations and Structure in the System La1-XSrxFeO3-δ (0 ≤ x ≤ 1, 0 ≤ δ ≤ 0.5)*, Journal of Solid State Chemistry **109**, 134 (1994).

[148] C. A. L. Dixon, C. M. Kavanagh, K. S. Knight, W. Kockelmann, F. D. Morrison, and P. Lightfoot, *Thermal Evolution of the Crystal Structure of the Orthorhombic Perovskite LaFeO3*, Journal of Solid State Chemistry **230**, 337 (2015).

[149] A. M. Glazer, *The Classification of Tilted Octahedra in Perovskites*, Acta Cryst B **28**, 11 (1972).

[150] S. M. Selbach, J. R. Tolchard, A. Fossdal, and T. Grande, *Non-Linear Thermal Evolution of the Crystal Structure and Phase Transitions of LaFeO3 Investigated by High Temperature X-Ray Diffraction*, Journal of Solid State Chemistry **196**, 249 (2012).

[151] M. Capone, C. J. Ridley, N. P. Funnell, M. Guthrie, and C. L. Bull, *Subtle Structural Changes in LaFeO3 at High Pressure*, Physica Status Solidi (b) **258**, 2000413 (2021).

[152] J. W. Seo, E. E. Fullerton, F. Nolting, A. Scholl, J. Fompeyrine, and J.-P. Locquet, *Antiferromagnetic LaFeO$\less$sub$\greater$3$\less$/Sub$\greater$thin Films and Their Effect on Exchange Bias*, J. Phys.: Condens. Matter **20**, 264014 (2008).

[153] M. D. Scafetta, A. M. Cordi, J. M. Rondinelli, and S. J. May, *Band Structure and Optical Transitions in LaFeO3: Theory and Experiment*, J. Phys.: Condens. Matter **26**, 505502 (2014).

[154] R. Comes and S. Chambers, *Interface Structure, Band Alignment, and Built-In Potentials at ${\mathrm{LaFeO}}_{3}/N\text{\ensuremath{-}}{\mathrm{SrTiO}}_{3}$ Heterojunctions*, Phys. Rev. Lett. **117**, 226802 (2016).

[155] S. Y. Yang et al., *Above-Bandgap Voltages from Ferroelectric Photovoltaic Devices*, Nature Nanotech **5**, 2 (2010).

[156] W. S. Choi, M. F. Chisholm, D. J. Singh, T. Choi, G. E. Jellison, and H. N. Lee, *Wide Bandgap Tunability in Complex Transition Metal Oxides by Site-Specific Substitution*, Nat Commun **3**, 1 (2012).

[157] T. Choi, S. Lee, Y. J. Choi, V. Kiryukhin, and S.-W. Cheong, *Switchable Ferroelectric Diode and Photovoltaic Effect in BiFeO3*, Science **324**, 63 (2009).

[158] F. Andrei et al., *Thickness-Dependent Photoelectrochemical Water Splitting Properties of Self-Assembled Nanostructured LaFeO3 Perovskite Thin Films*, Nanomaterials **11**, 6 (2021).

[159] K. M. Parida, K. H. Reddy, S. Martha, D. P. Das, and N. Biswal, *Fabrication of Nanocrystalline LaFeO3: An Efficient Sol–Gel Auto-Combustion Assisted Visible Light Responsive Photocatalyst for Water Decomposition*, International Journal of Hydrogen Energy **35**, 12161 (2010).

[160] R. Comes and S. Chambers, *Interface Structure, Band Alignment, and Built-In Potentials at LaFeO 3 / n − SrTiO 3 Heterojunctions*, Phys. Rev. Lett. **117**, 226802 (2016).

[161] J. H. Haeni, C. D. Theis, D. G. Schlom, W. Tian, X. Q. Pan, H. Chang, I. Takeuchi, and X.-D. Xiang, *Epitaxial Growth of the First Five Members of the Srn+1TinO3n+1 Ruddlesden–Popper Homologous Series*, Appl. Phys. Lett. **78**, 3292 (2001).

[162] L. Qiao et al., *The Impacts of Cation Stoichiometry and Substrate Surface Quality on Nucleation, Structure, Defect Formation, and Intermixing in Complex Oxide Heteroepitaxy–LaCrO3 on SrTiO3(001)*, Advanced Functional Materials **23**, 2953 (2013).

[163] S. A. Chambers, Y. J. Kim, and Y. Gao, *Fe 2* p *Core-Level Spectra for Pure, Epitaxial α-Fe 2 O 3 (0001), γ-Fe 2 O 3 (001), and Fe 3 O 4 (001)*, Surface Science Spectra **5**, 219 (1998).

[164] M. Varela, M. P. Oxley, W. Luo, J. Tao, M. Watanabe, A. R. Lupini, S. T. Pantelides, and S. J. Pennycook, *Atomic-Resolution Imaging of Oxidation States in Manganites*, Phys. Rev. B **79**, 085117 (2009).

[165] S. R. Spurgeon, P. V. Sushko, S. A. Chambers, and R. B. Comes, *Dynamic Interface Rearrangement in LaFeO 3 / n − SrTiO 3 Heterojunctions*, Phys. Rev. Materials **1**, 063401 (2017).

[166] H. Tan, J. Verbeeck, A. Abakumov, and G. Van Tendeloo, *Oxidation State and Chemical Shift Investigation in Transition Metal Oxides by EELS*, Ultramicroscopy **116**, 24 (2012).

[167] P. Xu et al., *Reversible Formation of 2D Electron Gas at the LaFeO 3 /SrTiO 3 Interface via Control of Oxygen Vacancies*, Adv. Mater. **29**, 1604447 (2017).

[168] R. Comes and S. Chambers, *Interface Structure, Band Alignment, and Built-In Potentials at ${\mathrm{LaFeO}}_{3}/N\text{\ensuremath{-}}{\mathrm{SrTiO}}_{3}$ Heterojunctions*, Phys. Rev. Lett. **117**, 226802 (2016).

[169] A. Hagfeldt and M. Graetzel, *Light-Induced Redox Reactions in Nanocrystalline Systems*, Chem. Rev. **95**, 49 (1995).

[170] J. Bisquert, *Beyond the Quasistatic Approximation: Impedance and Capacitance of an Exponential Distribution of Traps*, Phys. Rev. B **77**, 235203 (2008).

[171] F. Fabregat-Santiago, I. Mora-Seró, G. Garcia-Belmonte, and J. Bisquert, *Cyclic Voltammetry Studies of Nanoporous Semiconductors. Capacitive and Reactive Properties of Nanocrystalline TiO2 Electrodes in Aqueous Electrolyte*, J. Phys. Chem. B **107**, 758 (2003).

[172] J. L. García-Muñoz, J. Rodríguez-Carvajal, P. Lacorre, and J. B. Torrance, *Neutron-Diffraction Study of R${\mathrm{NiO}}_{3}$ (R=La,Pr,Nd,Sm): Electronically Induced Structural Changes across the Metal-Insulator Transition*, Phys. Rev. B **46**, 4414 (1992).

[173] M. L. Medarde, *Structural, Magnetic and Electronic Properties of Perovskites (R = Rare Earth)*, J. Phys.: Condens. Matter **9**, 1679 (1997).

[174] H. Guo et al., *Antiferromagnetic Correlations in the Metallic Strongly Correlated Transition Metal Oxide LaNiO3*, Nat Commun **9**, 1 (2018).

[175] K. Sreedhar, J. M. Honig, M. Darwin, M. McElfresh, P. M. Shand, J. Xu, B. C. Crooker, and J. Spalek, *Electronic Properties of the Metallic Perovskite ${\mathrm{LaNiO}}_{3}$: Correlated Behavior of 3d Electrons*, Phys. Rev. B **46**, 6382 (1992).

[176] E. Alves, H. P. Martins, S. Domenech, and M. Abbate, *Band Structure and Cluster Model Calculations of LaNiO3 Compared to Photoemission, O 1s X-Ray Absorption, and Optical Absorption Spectra*, Physics Letters A **383**, 2952 (2019).

[177] A. Yu. Dobin, K. R. Nikolaev, I. N. Krivorotov, R. M. Wentzcovitch, E. D. Dahlberg, and A. M. Goldman, *Electronic and Crystal Structure of Fully Strained ${\mathrm{LaNiO}}_{3}$ Films*, Phys. Rev. B **68**, 113408 (2003).

[178] A. M. Ritzmann, A. B. Muñoz-García, M. Pavone, J. A. Keith, and E. A. Carter, *Ab Initio DFT+U Analysis of Oxygen Vacancy Formation and Migration in La1-XSrxFeO3-δ (x = 0, 0.25, 0.50)*, Chem. Mater. **25**, 3011 (2013).

[179] H. Wadati et al., *Hole-Doping-Induced Changes in the Electronic Structure of ${\mathrm{La}}_{1\ensuremath{-}x}{\mathrm{Sr}}_{x}{\mathrm{FeO}}_{3}$: Soft x-Ray Photoemission and Absorption Study of Epitaxial Thin Films*, Phys. Rev. B **71**, 035108 (2005).

[180] L.-W. Tai, M. M. Nasrallah, H. U. Anderson, D. M. Sparlin, and S. R. Sehlin, *Structure and Electrical Properties of La1 − XSrxCo1 − YFeyO3. Part 2. The System La1 − XSrxCo0.2Fe0.8O3*, Solid State Ionics **76**, 273 (1995).

[181] G. P. Wheeler, V. U. Baltazar, T. J. Smart, A. Radmilovic, Y. Ping, and K.-S. Choi, *Combined Theoretical and Experimental Investigations of Atomic Doping To Enhance Photon Absorption and Carrier Transport of LaFeO3 Photocathodes*, Chem. Mater. **31**, 5890 (2019).

[182] X. Sun, D. Tiwari, and D. J. Fermin, *Promoting Active Electronic States in LaFeO3 Thin-Films Photocathodes via Alkaline-Earth Metal Substitution*, ACS Appl. Mater. Interfaces **12**, 31486 (2020).

[183] Y. J. Xie, M. D. Scafetta, E. J. Moon, A. L. Krick, R. J. Sichel-Tissot, and S. J. May, *Electronic Phase Diagram of Epitaxial La1−xSrxFeO3 Films*, Appl. Phys. Lett. **105**, 062110 (2014).

[184] S. A. Chambers and S. A. Joyce, *Surface Termination, Composition and Reconstruction of Fe3O4(001) and γ-Fe2O3(001)*, Surf. Sci. **420**, 111 (1999).

[185] M. Abbate, F. M. F. Degroot, J. C. Fuggle, A. Fujimori, O. Strebel, F. Lopez, M. Domke, G. Kaindl, G. A. Sawatzky, and M. Takano, *Controlled-Valence Properties of La1–XSrxFeO3 and La1–XSrxMnO3 Studied by Soft-X-Ray Absorption-Spectroscopy*, Phys. Rev. B **46**, 4511 (1992).

[186] S. She, J. Yu, W. Tang, Y. Zhu, Y. Chen, J. Sunarso, W. Zhou, and Z. Shao, *Systematic Study of Oxygen Evolution Activity and Stability on La1–XSrxFeO3−δ Perovskite Electrocatalysts in Alkaline Media*, ACS Appl. Mater. Interfaces **10**, 11715 (2018).

[187] S. A. Chambers, L. Qiao, T. C. Droubay, T. C. Kaspar, B. W. Arey, and P. V. Sushko, *Band Alignment, Built-In Potential, and the Absence of Conductivity at the*

${\mathrm{LaCrO}}_{3}/{\mathrm{SrTiO}}_{3}(001)$ Heterojunction, Phys. Rev. Lett. **107**, 206802 (2011).

[188] S. A. Chambers et al., *Instability, Intermixing and Electronic Structure at the Epitaxial LaAlO3/SrTiO3(001) Heterojunction*, Surface Science Reports **65**, 317 (2010).

[189] M. A. Kuroda, J. Tersoff, R. A. Nistor, and G. J. Martyna, *Optimal Thickness for Charge Transfer in Multilayer Graphene Electrodes*, Phys. Rev. Applied **1**, 014005 (2014).

[190] A. Ohtomo, D. A. Muller, J. L. Grazul, and H. Y. Hwang, *Artificial Charge-Modulationin Atomic-Scale Perovskite Titanate Superlattices*, Nature **419**, 378 (2002).

[191] I. González, S. Okamoto, S. Yunoki, A. Moreo, and E. Dagotto, *Charge Transfer in Heterostructures of Strongly Correlated Materials*, J. Phys.: Condens. Matter **20**, 264002 (2008).

[192] H. Chen, A. J. Millis, and C. A. Marianetti, *Engineering Correlation Effects via Artificially Designed Oxide Superlattices*, Phys. Rev. Lett. **111**, 116403 (2013).

[193] J. Garcia-Barriocanal et al., *"Charge Leakage" at LaMnO3/SrTiO3 Interfaces*, Advanced Materials **22**, 627 (2010).

[194] M. N. Grisolia et al., *Hybridization-Controlled Charge Transfer and Induced Magnetism at Correlated Oxide Interfaces*, Nature Physics **12**, 484 (2016).

[195] A. S. Disa, D. P. Kumah, A. Malashevich, H. Chen, D. A. Arena, E. D. Specht, S. Ismail-Beigi, F. J. Walker, and C. H. Ahn, *Orbital Engineering in Symmetry-Breaking Polar Heterostructures*, Phys. Rev. Lett. **114**, 026801 (2015).

[196] A. Prakash et al., *Separating Electrons and Donors in BaSnO3 via Band Engineering*, Nano Lett. **19**, 8920 (2019).

[197] A. R. Burton, R. Paudel, B. Matthews, M. Sassi, S. R. Spurgeon, B. H. Farnum, and R. B. Comes, *Thickness Dependent OER Electrocatalysis of Epitaxial LaFeO 3 Thin Films*, Journal of Materials Chemistry A **10**, 1909 (2022).

[198] N.-T. Suen, S.-F. Hung, Q. Quan, N. Zhang, Y.-J. Xu, and H. M. Chen, *Electrocatalysis for the Oxygen Evolution Reaction: Recent Development and Future Perspectives*, Chem. Soc. Rev. **46**, 337 (2017).

[199] J. R. Petrie, V. R. Cooper, J. W. Freeland, T. L. Meyer, Z. Zhang, D. A. Lutterman, and H. N. Lee, *Enhanced Bifunctional Oxygen Catalysis in Strained LaNiO3 Perovskites*, J. Am. Chem. Soc. **138**, 2488 (2016).

[200] J. Rossmeisl, Z.-W. Qu, H. Zhu, G.-J. Kroes, and J. K. Nørskov, *Electrolysis of Water on Oxide Surfaces*, Journal of Electroanalytical Chemistry **607**, 83 (2007).

[201] I. C. Man, H.-Y. Su, F. Calle-Vallejo, H. A. Hansen, J. I. Martínez, N. G. Inoglu, J. Kitchin, T. F. Jaramillo, J. K. Nørskov, and J. Rossmeisl, *Universality in Oxygen Evolution Electrocatalysis on Oxide Surfaces*, ChemCatChem **3**, 1159 (2011).

[202] J. Bak, H. B. Bae, C. Oh, J. Son, and S.-Y. Chung, *Effect of Lattice Strain on the Formation of Ruddlesden–Popper Faults in Heteroepitaxial LaNiO3 for Oxygen Evolution Electrocatalysis*, J. Phys. Chem. Lett. **11**, 7253 (2020).

[203] J. Low, J. Yu, M. Jaroniec, S. Wageh, and A. A. Al-Ghamdi, *Heterojunction Photocatalysts*, Advanced Materials **29**, 1601694 (2017).

[204] J. Su, G.-D. Li, X.-H. Li, and J.-S. Chen, *2D/2D Heterojunctions for Catalysis*, Advanced Science **6**, 1801702 (2019).

[205] L. Wang et al., *Tuning Bifunctional Oxygen Electrocatalysts by Changing the A-Site Rare-Earth Element in Perovskite Nickelates*, Advanced Functional Materials **28**, 1803712 (2018).

[206] J. Bak, H. Bin Bae, and S.-Y. Chung, *Atomic-Scale Perturbation of Oxygen Octahedra via Surface Ion Exchange in Perovskite Nickelates Boosts Water Oxidation*, Nat Commun **10**, 2713 (2019).

[207] K. A. Stoerzinger, L. Wang, Y. Ye, M. Bowden, E. J. Crumlin, Y. Du, and S. A. Chambers, *Linking Surface Chemistry to Photovoltage in Sr-Substituted LaFeO 3 for Water Oxidation*, Journal of Materials Chemistry A **6**, 22170 (2018).

[208] T. Peterlin-Neumaier and E. Steichele, *Antiferromagnetic Structure of LaFeO3 from High Resolution Tof Neutron Diffraction*, Journal of Magnetism and Magnetic Materials **59**, 351 (1986).

[209] P. E. Blöchl, *Projector Augmented-Wave Method*, Phys. Rev. B **50**, 17953 (1994).

[210] H. J. Monkhorst and J. D. Pack, *Special Points for Brillouin-Zone Integrations*, Phys. Rev. B **13**, 5188 (1976).

[211] E. Iguchi and W. Hwan Jung, *Electrical Transports of* $LaFe_{1-x}Ti_xO_3$ ($x \leq 0.10$), J. Phys. Soc. Jpn. **63**, 3078 (1994).

[212] S. R. Provence, S. Thapa, R. Paudel, T. K. Truttmann, A. Prakash, B. Jalan, and R. B. Comes, *Machine Learning Analysis of Perovskite Oxides Grown by Molecular Beam Epitaxy*, Phys. Rev. Materials **4**, 083807 (2020).

[213] S. Thapa, R. Paudel, M. D. Blanchet, P. T. Gemperline, and R. B. Comes, *Probing Surfaces and Interfaces in Complex Oxide Films via in Situ X-Ray Photoelectron Spectroscopy*, Journal of Materials Research **36**, 26 (2021).

[214] R. B. Comes, P. Xu, B. Jalan, and S. A. Chambers, *Band Alignment of Epitaxial SrTiO3 Thin Films with (LaAlO3)0.3-(Sr2AlTaO6)0.7 (001)*, Applied Physics Letters **107**, 131601 (2015).

[215] K. J. May, D. P. Fenning, T. Ming, W. T. Hong, D. Lee, K. A. Stoerzinger, M. D. Biegalski, A. M. Kolpak, and Y. Shao-Horn, *Thickness-Dependent Photoelectrochemical Water Splitting on Ultrathin LaFeO 3 Films Grown on Nb:SrTiO 3*, J. Phys. Chem. Lett. **6**, 977 (2015).

[216] A. J. Mao, H. Tian, X. Y. Kuang, J. W. Jia, and J. S. Chai, *Structural Phase Transition and Spin Reorientation of LaFeO3 Films under Epitaxial Strain*, RSC Adv. **6**, 100526 (2016).

[217] J. Varignon, M. Bibes, and A. Zunger, *Origin of Band Gaps in 3d Perovskite Oxides*, Nat Commun **10**, 1658 (2019).

[218] L. Qiao and X. Bi, *Direct Observation of Ni3+ and Ni2+ in Correlated LaNiO3−δ Films*, (2011).

[219] Z. Liao et al., *Thickness Dependent Properties in Oxide Heterostructures Driven by Structurally Induced Metal–Oxygen Hybridization Variations*, Advanced Functional Materials **27**, 1606717 (2017).

[220] G. Gou, I. Grinberg, A. M. Rappe, and J. M. Rondinelli, *Lattice Normal Modes and Electronic Properties of the Correlated Metal LaNiO${}_{3}$*, Phys. Rev. B **84**, 144101 (2011).

Appendices

Appendix A

Supporting Information

Band-Engineered $LaFeO_3$-$LaNiO_3$ Thin Film Interfaces for Electrocatalysis of Water

Rajendra Paudel[1], Andricus R. Burton[2], Marcelo A. Kuroda[1], Byron H. Farnum[2], and Ryan B. Comes[1]

[1] Department of Physics, Auburn University, Auburn, AL, USA 36849

[2] Department of Chemistry, Auburn University, Auburn, AL, USA 36849

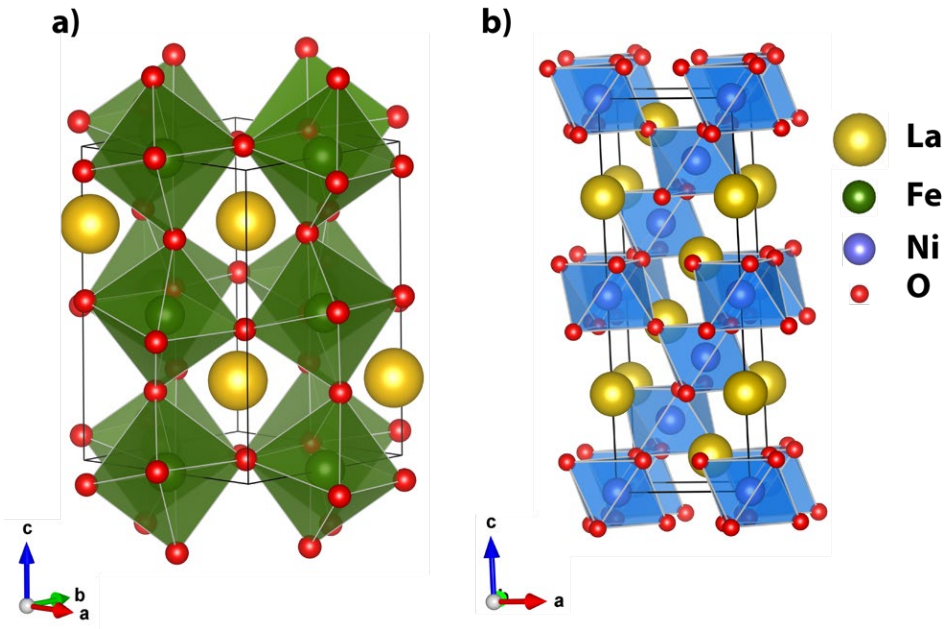

Figure S 1: Orthorhombic crystal structure of LFO b) Rhombohedral crystal structure of LNO.

$LaFeO_3$ has orthorhombic perovskite crystal structure at room temperature with antiferromagnetic phase. And LNO is a rhombohedral perovskite with no magnetic phase at room temperature. Both the structures are shown in **Figure S1.**

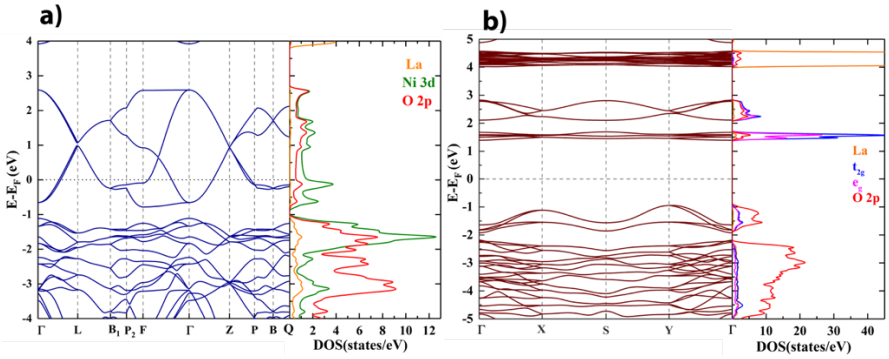

Figure S 2: Electronic band structure and density of states of LaNiO3, b) Electronic band structure and density of states of LaFeO3, contributions from both majority and minority spins, projected on various atoms and atomic orbitals.

To test the ability of our DFT model of these materials to replicate the available experimental results in the literature and further understand the electronic properties of LFO and LNO we performed first principles calculation on the bulk. Electronic bands and DOS are presented in the Figure S2. LFO at room temperature has G-type antiferromagnetic phase with orthorhombic crystal structure. Occupied eg states of Fe3+ lie in the valence band and unoccupied t2g forms the state close to the Fermi level in conduction band. Spin polarized DFT+U calculation estimates the bandgap ~2.2eV, which is in close agreement with experimental band gap of 2.3eV [153]

LNO, on the other hand is a rhombohedral paramagnetic metal at room temperature. The bands near the fermi level are strongly hybridized Ni 3d and O2p orbitals, which is responsible for metallicity of LNO. Ni3+ t2g states which are almost completely filled, forms the valence band

and partially occupied eg states cross the fermi level forming metallic band. This is consistent with experimentally observed electronic structure of LNO

In order to find out the electronic bands forming VBM in LFO/LNO superlattice we projected the contribution from various atoms and atomic orbitals onto electronic bands. **Figure S3** shows the projected bands. Our calculation confirms the band offset estimated from the density of states which is ~0.2 eV. Fe 3d and O 2p orbitals form the VBM in LFO/LNO superlattice. This is consistent with our argument that electrons are transferred to conduction band (mostly Ni 3d bands) from valence band in the LFO.

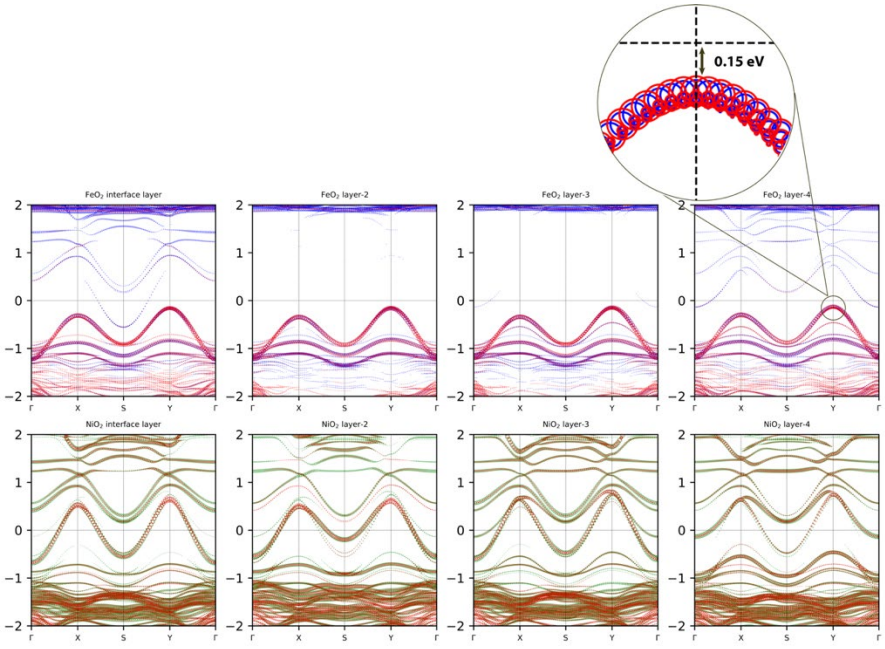

Figure S 3: Electronic band structure of LFO/LNO superlattice projected onto different atomic layers based on the contribution from different atomic orbitals. Size of the circles are proportional to the weight of orbital contribution.

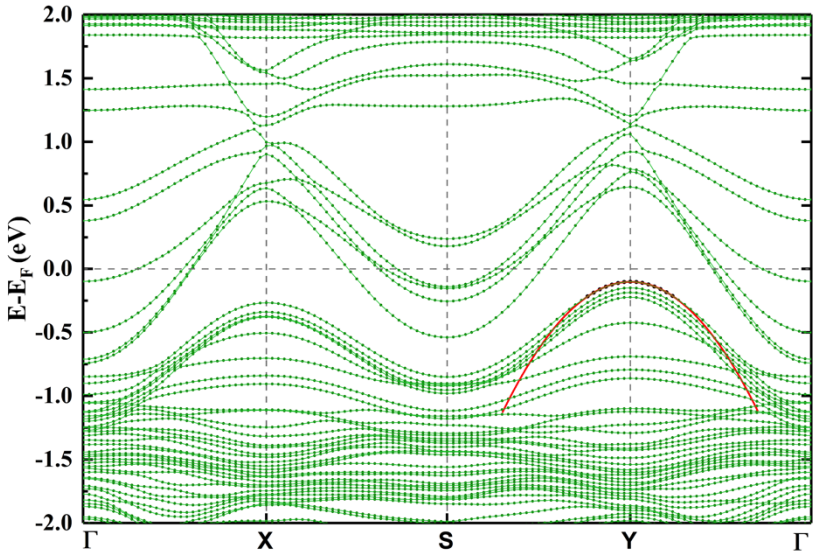

Figure S 4: Parabolic fit to the electronic bands of LFO/LNO superlattice forming VBM to calculate the hole effective mass at the along (100) and (010) directions.

The energy of the electron for given k value is

$$E(k) = E_0 + \frac{\hbar^2 \kappa^2}{2m}$$

And effective mass of electrons of holes in the energy band is calculated from second derivative of the E versus *k* curve as,

$$\frac{1}{m*} = \frac{1}{\hbar^2}\left(\frac{\partial^2 E(k)}{\partial k^2}\right)$$

Considering the symmetric nature of the electronic bands we calculated the effective mass of hole along **S-Y-Γ** k-path. We considered the energy range of $5K_BT$ to fit the quadratic function. The parabolic fit to the bands forming VBM is shown in **Figure S4**. We estimated the effective mass of holes to be $0.6m_e$.

From the information about density of states, position of Fermi energy and valence band maximum we can calculate the number of thermally generated holes at temperature T as,

$$P_o = \int_{-\infty}^{E_v} g_v(E)[1 - f_F(E)]dE$$

$$Where, \quad 1 - f_E(E) = \frac{1}{1 + exp(\frac{E_F - E}{kT})}$$

For (E_F-E_v)>>kT,

$$1 - f_E(E) \approx exp[\frac{-(E_F - E)}{kT}]$$

And density of holes is calculated as, $n = \frac{P_o}{unit\ cell\ Volume}$

We estimated the charge transfer from our DFT results for bulk LFO. We used the LFO DOS data from the bulk and used the position of VBM relative to Fermi energy from LFO/LNO superlattice. We estimated hole density for a range of VBM positions relative to Fermi energy and are presented in the table S1.

Table S0.1: Density of holes on valence band for different band offset values

Band Offset(eV)	Hole density(cm^{-3})
0.0	1.36×10^{20}
0.1	2.86×10^{18}
0.2	6.02×10^{16}

0.3	1.27×10^{15}

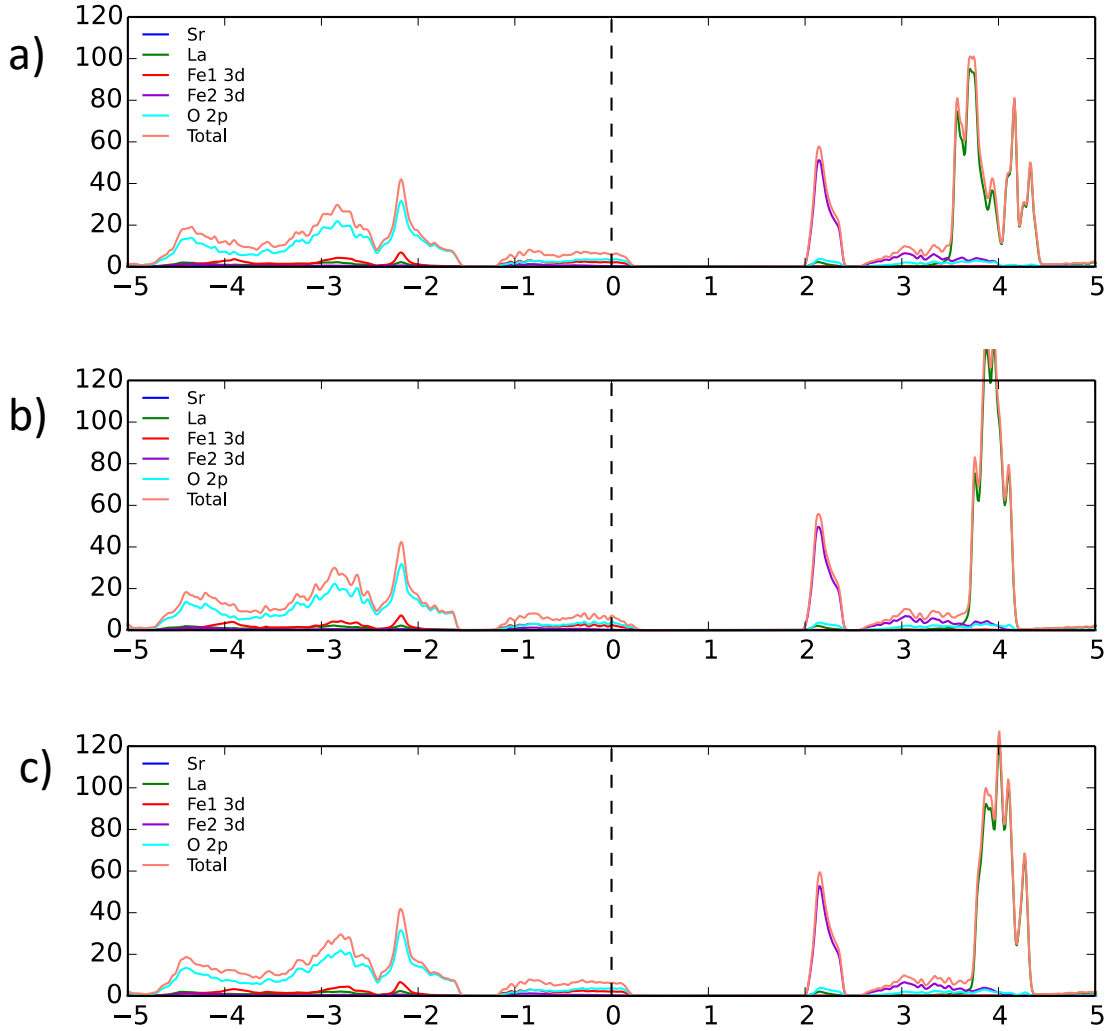

Figure S 5: Density of states for different symmetry of Sr^{2+} substitution for x=0.25. a) in corner and face of the cubic unit cell b) in corner and center of the cube c) in corner and edge of the cube